

## INFORMATION TO USERS

This material was produced from a microfilm copy of the original document. While the most advanced technological means to photograph and reproduce this document have been used, the quality is heavily dependent upon the quality of the original submitted.

The following explanation of techniques is provided to help you understand markings or patterns which may appear on this reproduction.

1. The sign or "target" for pages apparently lacking from the document photographed is "Missing Page(s)". If it was possible to obtain the missing page(s) or section, they are spliced into the film along with adjacent pages. This may have necessitated cutting thru an image and duplicating adjacent pages to insure you complete continuity.
2. When an image on the film is obliterated with a large round black mark, it is an indication that the photographer suspected that the copy may have moved during exposure and thus cause a blurred image. You will find a good image of the page in the adjacent frame.
3. When a map, drawing or chart, etc., was part of the material being photographed the photographer followed a definite method in "sectioning" the material. It is customary to begin photoing at the upper left hand corner of a large sheet and to continue photoing from left to right in equal sections with a small overlap. If necessary, sectioning is continued again — beginning below the first row and continuing on until complete.
4. The majority of users indicate that the textual content is of greatest value, however, a somewhat higher quality reproduction could be made from "photographs" if essential to the understanding of the dissertation. Silver prints of "photographs" may be ordered at additional charge by writing the Order Department, giving the catalog number, title, author and specific pages you wish reproduced.
5. PLEASE NOTE: Some pages may have indistinct print. Filmed as received.

**Xerox University Microfilms**

300 North Zeeb Road  
Ann Arbor, Michigan 48106

74-10,979

JOBE, Charles Edwin, 1939-  
THE NUMERICAL SOLUTION OF THE ASYMPTOTIC  
EQUATIONS OF TRAILING EDGE FLOW.

The Ohio State University, Ph.D., 1973  
Engineering, aeronautical

University Microfilms, A XEROX Company, Ann Arbor, Michigan

THE NUMERICAL SOLUTION OF THE ASYMPTOTIC  
EQUATIONS OF TRAILING EDGE FLOW

DISSERTATION

Presented in Partial Fulfillment of the Requirements for  
the Degree Doctor of Philosophy in the Graduate  
School of The Ohio State University

By

Charles Edwin Jobe, B.Aero.E., M.Sc.

\* \* \* \* \*

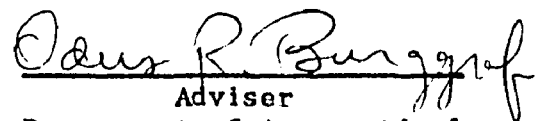
The Ohio State University

1973

Reading Committee:

Odus R. Burggraf  
Robert M. Nerem  
Stuart L. Petrie

Approved by

  
Adviser  
Department of Aeronautical  
and  
Astronautical Engineering

#### ACKNOWLEDGMENTS

The author wishes to gratefully acknowledge the patience, guidance and encouragement of Professor Odus Burggraf. The author is also indebted to Professor K. Stewartson for several enlightening discussions and considerable encouragement.

## VITA

June 19, 1939 . . . Born - Detroit, Michigan

1961 . . . . . B.Aero.E., University of Detroit,  
Detroit, Michigan

1961-Present . . . Aerospace Engineer, Air Force Flight  
Dynamics Laboratory, Wright-Patterson  
Air Force Base, Ohio

1966 . . . . . M.Sc., The Ohio State University,  
Columbus, Ohio

## FIELDS OF STUDY

**Major Field: Aeronautical and Astronautical Engineering**

**Fluid Mechanics.** Professors Odus R. Burggraf and K. Stewartson

**Applied Mathematics.** Professors Henry D. Colson, Odus R. Burggraf,  
and K. Stewartson

**Aerodynamics.** Professors Odus R. Burggraf, John D. Lee,  
Garvin L. Von Eschen, Ting Y. Li, and Robert M. Nerem

TABLE OF CONTENTS

	Page
ACKNOWLEDGMENTS . . . . .	ii
VITA . . . . .	iii
LIST OF TABLES . . . . .	v
LIST OF ILLUSTRATIONS . . . . .	vi
 Chapter	
I.    INTRODUCTION . . . . .	1
II.   THE TRIPLE-DECK ANALYSIS . . . . .	8
III.  THE NUMERICAL PROCEDURE . . . . .	26
Input Data	
The Main Program	
The Hilbert Transformation	
The Boundary-Layer Subroutine	
IV.   THE RESULTS . . . . .	45
V.    CONCLUSIONS . . . . .	80
 APPENDIX	
A. . . . .	84
B. . . . .	95
C. . . . .	108
REFERENCES . . . . .	113

## LIST OF TABLES

Table	Page
1. Drag Comparison with Numerical Data Flat Plate Drag . . .	49
2. Drag Comparison with Experimental Data . . . . .	51
3. The Numerical Results . . . . .	82
4. The Numerical Solution of $F_1''' - 18\eta^2 F_1'' - 36(\eta F_1' - F_1) = -1.8330$ . . . . .	86

## LIST OF ILLUSTRATIONS

Figure	Page
1. A Flow Chart of the Main Program . . . . .	27
2. Initial Velocity Profile at $X = -6$ . . . . .	30
3. Initial Estimate for the Displacement Thickness . . . . .	32
4. Skin Friction near the Trailing Edge . . . . .	46
5. Drag versus Reynolds Number - A Comparison of Theory and Experiment . . . . .	52
6. Induced Pressure Distribution . . . . .	54
7. A Comparison of the Induced Pressure Distribution with the Results of Schneider & Denny at $R = 10^5$ . . . . .	55
8. Lower Deck Displacement Function, $A(X)$ . . . . .	57
9. Slope of the Displacement Function, $A'(X)$ . . . . .	59
10. Pressure-Displacement Function Error Analysis . . . . .	61
11. The Centerline Velocity. . . . .	63
12. The Centerline Velocity near $X = 0$ . . . . .	65
13. The Pressure near $X = 0$ . . . . .	66
14. The Asymptotic Behavior: $b_1$ for $X \rightarrow 6$ , $\Delta X = .05$ . . . . .	68
15. The Asymptotic Behavior: $b_1$ for $X \rightarrow 6$ , $\Delta X = .025$ . . . . .	69
16. The Asymptotic Behavior: $b_1$ for $X \rightarrow 12$ , $\Delta X = .05$ . . . . .	70
17. A Comparison of the Lower Deck and the Goldstein Wake Velocity Profiles . . . . .	73
18. Velocity Perturbations on the Plate . . . . .	75
19. Velocity Perturbations at the Trailing Edge . . . . .	76
20. Velocity Perturbations in the Inner Wake . . . . .	77



Figure	Page
21. Velocity Profiles in the Inner Wake . . . . .	79
22. A Summary of the Numerical Results . . . . .	81
23. A Comparison of Initial Velocity Profiles . . . . .	85
24. A Comparison of the Skin Friction resulting from the Initial Velocity Profiles . . . . .	88
25. Cauchy Integral Error Analysis . . . . .	91
26. Hilbert Transformation Error Analysis . . . . .	93
27. Asymptotic Behavior: $Z_e = 6$ , Shallow Velocity Profile .	96
28. Asymptotic Behavior: $Z_e = 6$ , Revised Velocity Profile .	98
29. Asymptotic Behavior: $Z_e = 8$ , Revised Velocity Profile .	99
30. Asymptotic Behavior: $Z_e = 8$ , The Pressure Shift . . . .	101
31. Asymptotic Behavior: $Z_e = 9$ , Second-Order Terms . . . .	103
32. Asymptotic Behavior: $Z_e = 9$ , Second-Order Terms . . . .	104
33. Asymptotic Behavior: $Z_e = 9$ , Centerline Boundary Condition . . . . .	106
34. A Comparison of the Centerline Velocity for Goldstein's Inner Wake . . . . .	112

## CHAPTER I

### INTRODUCTION

The quest for the second and higher approximations to the laminar boundary layer over a finite flat plate immersed in an incompressible viscous fluid has been accompanied by considerable controversy. It has been and is the cause of extensive analytical and numerical efforts. The controversy arose anew about 1969 when Stewartson (1969), and separately Messiter (1970), derived a rational, consistent expansion procedure for the neighborhood of the trailing edge. Their analyses predict that the second order term in the Reynolds number expansion for the drag of the plate is  $O(R^{-7/8})$ . The Reynolds number is based on the plate length,  $L$ , freestream velocity,  $U_{\infty}$ , and kinematic viscosity,  $\nu$ . A numerical solution to the fundamental problem of the trailing edge is required to determine the multiplicative constant appearing in this term.

It is the purpose of this dissertation to present the results of numerical computations which clearly demonstrate that a physically acceptable numerical solution to the fundamental problem of the trailing edge exists and determines the constants which are required to complete Stewartson's (1969) analysis.

The controversy concerns the streamwise extent of the region influenced by the change in boundary conditions at the trailing edge.

As pointed out by all the current authors concerned with this problem, the assumptions on which the boundary-layer equations are based fail in a neighborhood of the trailing edge of  $O(R^{-3/4})$ . The Navier Stokes equations must be applied in this region and its relevance is not the cause for the controversy. If this  $O(R^{-3/4})$  region were the entire streamwise extent of the influence of the trailing edge, as contended by some authors, the second-order term in the drag equation is  $O(R^{-1})$ , as shown by Imai (1957). The  $O(R^{-3/4})$  region contributes a still higher-order term,  $O(R^{-5/4})$ . However, the basic hypothesis of the triple-deck analyses of Stewartson (1969) and Messiter (1970) that leads to a consistent description of the flow field is that the streamwise region influenced by the trailing edge is  $O(R^{-3/8})$ . This larger region produces a term of  $O(R^{-7/8})$  in the finite flat plate drag equation; thus it intervenes to become second-order in the expansion of Imai (1957). This larger region also produces a term  $O(R^{-1})$ , as well as higher fractional-order terms, that will modify the constant derived by Imai (1957) who considered the displacement effect of the boundary layer over the semi-infinite flat plate using a momentum balance applied on a large circle centered on the leading edge. A review of Imai's analysis and several additional analyses based on inverse half-power Reynolds number expansions, as well as the additional controversy concerning the multiplicative constant which appears in the  $R^{-1}$  term, are contained in Van Dyke's (1964) book. The various values of the constant are: 4.12 (Kuo (1953)), 2.326 (Imai (1957)), and 5.3 (Van Dyke (1964)). Van Dyke proposes that the trailing-edge region can contribute only a third-order term, proportional to  $R^{-3/2}$ , to the drag equation since it is

sheltered by a relatively thick boundary layer, whereas the leading edge is exposed to the free stream.

The controversy is resolved by the present numerical solution to the fundamental problem of the trailing edge, a boundary-layer equation coupled to a Cauchy integral through the boundary condition at the outer edge. The numerical integration of the skin friction completely determines, to second-order, the drag on the plate. Thus

$$C_d = \frac{D}{\frac{1}{2}\rho U_\infty^2 L} = \frac{1.328}{R^{1/2}} + \frac{d_2}{R^{1/8}} + \dots ; \quad (1)$$

the leading term coming from Blasius' solution to the boundary-layer equations, the numerical factor being determined by Goldstein (1930) who elucidated the double structure of the near wake in the same paper using the notion of matched asymptotic expansions. In the above equation,  $D$  is the drag due to one side of the plate and  $\rho$  is the constant viscosity of the flow. In the present study the constant  $d_2$  was found to be 2.694. The drag predicted by Equation (1) with this value of  $d_2$  has been compared with the drag from the numerical solutions to the Navier-Stokes equations of Dennis (1973), Dennis and Chang (1969), and Dennis and Dunwoody (1966). This comparison has confirmed the validity of Equation (1) for a wider range of Reynolds numbers than could be expected--eight and one-half per cent high at  $R = 1$ ! A comparison with the oil flow data of Janour (1951) has a mean error of 1.5 per cent, a maximum error of 7.5 per cent, and a root mean square error of 3.5 per cent for Reynolds numbers from 12 to 2335. This equation is the most accurate correlation of Janour's data known.

Detailed comparisons of the wake centerline velocity and overall pressure distribution are in reasonable agreement with the data of Schneider and Denny (1971) for their single Reynolds number of  $10^5$ . Their method of solution used a separate numerical method in each of three regions. The pressure-displacement thickness in an outer, potential region was obtained by employing a source distribution of appropriate strength on the displacement thickness such that the flow normal to the displacement surface is zero. An implicit Crank-Nicholson type difference analogue was used to solve the boundary-layer equations in a transformed coordinate system which magnified the trailing-edge region. The second-order boundary-layer solution was obtained by manually constructing succeeding iterates using the transformed boundary-layer equations to obtain the displacement thickness which was input to the potential flow program to obtain improved values of the pressure. The boundary-layer solution provided the boundary conditions for the third, innermost region in which the full Navier-Stokes equations were solved by an integral averaging method. Schneider and Denny (1971) conclude that their Navier-Stokes solution appears to match their second-order boundary-layer solution on a circle of radius about  $R^{-3/4}$  for  $R = 10^5$ .

Dennis (1973) has obtained numerical solutions to the Navier-Stokes equations in elliptic coordinates for the finite flat plate. By fitting his skin friction results at  $R = 40, 100, \text{ and } 200$  he finds a larger trailing-edge region of influence that scales with  $R^{-3/8}$ , in agreement with Stewartson (1969) and Messiter (1970).

Plotkin and Flugge-Lotz (1968), using a numerical technique to solve the Navier-Stokes equations in boundary-layer variables, also

have found the influence of the trailing edge to extend much further than  $R^{-3/4}$  in the streamwise direction. They attempt to find an improved first approximation to the solution in a region approximately centered on the trailing edge, thus the displacement thickness effect of the boundary layer is neglected. As pointed out by several authors, their grid size is larger than  $R^{-3/4}$ ; it is not, however, larger than  $R^{-3/8}$ . Since their problem is not the problem considered here due to their neglect of the displacement thickness effect, detailed comparisons would not be valid. Qualitatively their results for the pressure, wake centerline velocity, and skin friction are in agreement with the present results.

The relevance of the  $O(R^{-3/8})$  scaling is implicit in the coordinate straining of Goldberg and Cheng (1961) and is a consistent limit for the Navier-Stokes equations as shown by Messiter (1970). Goldberg and Cheng (1961), however, find the region of upstream influence of the trailing edge is of  $O(R^{-1/2})$  by the coordinate straining method and of  $O(R^{-1})$  by their parabolic coordinate solution. They conclude that neither approach is likely to be correct since the estimates differ by  $O(R^{-1/2})$ .

The results of Talke and Berger (1970) are, indeed, difficult to reconcile with the present results. Talke and Berger (1970) have employed the method of series truncation (Van Dyke (1964)) to ascertain that the trailing edge influences an elliptic region of  $O(Re^{-3/4})$ . The boundary conditions in the near wake suggest an expansion for the stream function which is substituted into the Navier-Stokes equations expressed in parabolic coordinates and truncated at

one or two terms. The Reynolds number for each integral curve of the resulting fourth-order ordinary differential equation must be determined by numerically matching, i.e., patching, to the Goldstein (1930) near wake centerline velocity, either approximately, or exactly. The upstream influence of the trailing edge is then determined, for the first truncation, by equating the resulting skin friction to the Blasius skin friction to determine the point at which the curves coincide. This procedure is not possible for the second truncation since the minimum skin friction is always larger than the Blasius value (or the value at the triple-deck trailing edge). Therefore, it is assumed that the point of minimum skin friction determines the upstream extent of the trailing edge region for the second truncation.

From their results it can be shown that the downstream extent of the region of influence varies from  $R^{-.43}$  for  $R = 276$ , to  $R^{-.62}$  for  $R = 65,600$ , as determined by the streamwise location at which the numerical solutions are numerically matched to the Goldstein wake; while the upstream influence is, to a remarkable precision,  $R^{-.75}$ . The first truncation predicts a skin friction which, apparently, becomes smaller than the Blasius value and the second truncation predicts a skin friction considerably higher than the Blasius value. As the authors suggest, a numerical solution of the third truncation might be useful in numerically matching the skin friction if their sequence of truncations is convergent. It may also be of value in reconciling the anomalous behavior since the larger value of the skin friction predicted by the triple-deck analysis is now available.

The present method of solution utilizes the triple-deck coordinate system of Stewartson (1969) to remove the influence of Reynolds number from the trailing-edge problem. The boundary-layer equations of the lower deck are solved by an implicit Crank-Nicholson type difference analogue and an iteration procedure for the pressure gradient which is related to the displacement function of the potential upper deck by a Cauchy integral. Thus the boundary-layer equations are used to determine the pressure from the displacement function and the Cauchy integral of linear airfoil theory determines a new displacement function from the pressure, a reverse of the boundary layer-potential flow iteration procedure of Schneider and Denny (1971). The present iteration method is entirely automated and convergence is attained when the displacement function differs from its previous iterate by less than  $10^{-4}$  at each streamwise location. This iteration method eliminates any need for numerical differentiation. Interpolation is not necessary due to the use of a single coordinate system for both the boundary layer and potential flow calculations.

The use of the linear ized boundary condition and Cauchy integral to compute the pressure-displacement function relationship in the outer layer is justified to first order since the normal velocity is  $O(R^{-1/4})$  and the streamline slopes remain small compared to unity. This point has been reiterated by Messiter and Stewartson (1972) and Denny (1972).



## CHAPTER II

### THE TRIPLE-DECK ANALYSIS

The triple-deck analysis, necessitated by the change in boundary condition at the trailing edge, was applied to the finite flat plate aligned with an incompressible freestream by Stewartson (1969) and Messiter (1970). To the reader who is familiar with Stewartson's paper, this section is a summary of his analysis with minor corrections included here for completeness. The triple-deck and other multi-structured boundary-layer analysis methods have subsequently been applied to many separating flows. A complete review of this subject is forthcoming, Stewartson (1974).

The triple-deck region intervenes between the region of validity of the Blasius (1908) solution and the region of validity of the Goldstein (1930) wake solution in order to remove the discontinuity in the vertical velocity of the wake solution as the trailing edge is approached from the downstream side. The lower deck corresponds to Goldstein's inner viscous wake which arises from the change in boundary conditions at the trailing edge. The boundary-layer equations apply in the lower deck and the upstream influence of the wake is not permitted due to their parabolic nature. The main deck corresponds to Goldstein's essentially inviscid outer wake which is the inviscid continuation of the Blasius solution. The upper deck

is additional to the Goldstein solution and is required to account for the displacement effect of the wake. The flow in the upper deck is potential and permits the upstream influence of the wake through the elliptic nature of the governing equations. Thus the upstream influence of the wake is felt in the parabolic lower deck through the elliptic nature of the upper deck.

The ensuing notation is that of Stewartson (1969) with the two exceptions that  $R$  is used for  $Re$  and  $L$  replaces its lower case script version. Define a physical, rectangular cartesian coordinate system,  $Ox^*y^*$ , centered at the trailing edge with velocity components  $u^*$  and  $v^*$ ;  $u^*$  and  $x^*$  are aligned with the freestream,  $U_\infty$ , and  $y^*$  and  $v^*$  are normal to the freestream and the plate which extends a distance  $L$  upstream in the negative  $x^*$ -direction. Additionally,  $p^*$  is the pressure and  $\epsilon$  is the inverse one-eighth power of the Reynolds number.

The streamwise extent of the triple-deck, or intermediate region between the region of the Blasius (1908) solution and the Goldstein (1930) wake region is  $x^* = O(L\epsilon^3)$ . Various length scales for this intermediate region may be envisioned and tried; however, the  $L\epsilon^3$  scale has been demonstrated to lead to a consistent description of the flow field in the trailing-edge region. The upper deck, of length  $O(L\epsilon^3)$  in the  $y^*$ -direction, protrudes above the conventional boundary layer and wake to account for the displacement thickness perturbation induced by the lower deck where  $y^* = O(L\epsilon^5)$ . The lower deck is required to reduce the slip velocity at the lower edge of the main deck to its value on the plate, zero. The main deck, which is essentially inviscid and relatively passive, is  $O(L\epsilon^4)$  in  $y^*$

and must match the upper and lower decks as well as the streamwise component of the Blasius solution upstream and the Goldstein outer wake downstream of the trailing edge.

We now define dependent and independent variables which emphasize the physics of the flow field in the various layers or decks and proceed to set up the boundary conditions to which the expansions must match. Define  $x$ ,  $u$ ,  $v$  and  $p$  by:

$$x^* = \epsilon^3 Lx, \quad u^* = U_\infty u, \quad v^* = U_\infty v, \quad p^* = P_\infty + \rho U_\infty^2 p \quad (2)$$

in all three decks and  $Y$ ,  $y$ , and  $z$  by

$$y^* = \epsilon^3 LY, \quad y^* = \epsilon^4 Ly, \quad y^* = \epsilon^5 Lz \quad (3)$$

in the upper, main, and lower decks, respectively.

Upstream of the trailing edge,  $x \rightarrow -\infty$  and the expansions in the various decks must match the streamwise component of the Blasius solution,  $U_0(y)$ , where  $U_0(y) = \Psi_0'(y)$  and  $\Psi_0$  satisfies the conventional Blasius equation

$$\Psi_0'''' + \Psi_0 \Psi_0'' = 0, \quad \Psi_0(0) = \Psi_0'(0) = 0, \quad \Psi_0'(\infty) = 1 \quad (4)$$

with  $y$  as the independent variable. The upstream boundary conditions for the main deck,  $y$  fixed, are

$$u \rightarrow U_0(y) + O(\epsilon^3), \quad v \rightarrow O(\epsilon^4) \quad \text{and} \quad p \rightarrow O(\epsilon^4), \quad (5)$$

the  $\epsilon^3$  term in  $u$  arising because the full Blasius solution depends on the square root of  $L + x^*$  as well as  $y^*$ . Above the entire triple-deck,  $Y \rightarrow \infty$ ,  $x$  fixed, the perturbations due to the overall displacement

thickness of the boundary layer are  $O(\epsilon^4)$  and

$$u \rightarrow 1 + O(\epsilon^4), \quad v \rightarrow O(\epsilon^4), \quad p \rightarrow O(\epsilon^4) \quad (6)$$

This boundary condition will necessitate the introduction of the upper deck.

Proceeding along the centerline  $y = 0$  the boundary conditions are

$$u = v = 0, \quad \text{if } x < 0, \quad \text{and } v = \partial u / \partial y = 0, \quad \text{if } x > 0 \quad (7)$$

which will necessitate the introduction of the lower deck when  $x < 0$ .

The three-layered structure is also evident in the boundary conditions downstream - the near wake. The double-structure of the near wake was first elucidated by Goldstein (1930) who assumed the pressure to be constant throughout the trailing edge region and a Taylor series expansion of  $U_0(y)$  remains valid to the trailing edge, i.e.,

$$U_0(y) = a_1 y + a_4 y^4 + a_7 y^7 + \dots \quad (8)$$

where

$$a_1 = 0.3321 = \lambda. \quad (9)$$

Assuming an expansion of the form

$$u = \frac{1}{3} \left( \frac{x^*}{4L} \right)^{1/3} f_0(\eta^*) + \frac{1}{3} \left( \frac{x^*}{4L} \right)^{4/3} f_1'(\eta^*) + \dots \quad (10)$$

for the inner wake, he found  $f_0$  must satisfy

$$f_0'''' + 2f_0 f_0'' - f_0'^2 = 0, \quad f_0(0) = f_0'' = 0, \quad f_0' \eta^{*-1} \rightarrow 18a_1 \text{ as } \eta^* \rightarrow \infty \quad (11)$$

where

$$\eta^* = y^*/3\epsilon^4 (2L^2 x^*)^{1/3} = y/3\epsilon (2x)^{1/3} = z/3(2x)^{1/3}. \quad (12)$$

Examining the structure of Equation (10) for large  $\eta^*$ , Goldstein found that in the outer wake  $u$  may be expanded in the series

$$u = U_0(y) + \left(\frac{x^*}{4L}\right)^{1/3} U_1(y) + \left(\frac{x^*}{4L}\right)^{2/3} U_2(y) + \dots \quad (13)$$

where each of  $U_n$  are related to  $U_0$ .

$$U_1(y) = \delta_1 \frac{dU_0}{dy}, \quad U_2(y) = \frac{1}{2} \delta_1^2 \frac{d^2 U_0}{dy^2} \quad (14)$$

etc., where  $\delta_1 = 2.0448$ .

The downstream boundary conditions ( $x \rightarrow \infty$ ) for the triple-deck are:  $v \rightarrow 0(\epsilon^4)$  and  $p \rightarrow 0(\epsilon^4)$  in all three decks while

$$u \rightarrow \frac{\epsilon}{3} \left(\frac{x}{4}\right)^{1/3} f_0'(\eta^*) + 0(\epsilon^4) \quad (15)$$

when  $\eta^*$  is finite,

$$u \rightarrow U_0(y) + \epsilon x^{1/3} \delta_1 \frac{dU_0}{dy} + 0(\epsilon^2) \quad (16)$$

when  $y$  is finite, and

$$u \rightarrow 1 + O(\epsilon^4) \quad (17)$$

when  $Y$  is finite.

On the plate, the main deck will require the introduction of the upper deck to satisfy the boundary condition, Equation (6), and similarly, the lower deck is required to satisfy Equation (7). To see this, we substitute the expansions

$$u(x,y) = U_0(y) + \epsilon u_1(x,y) + \epsilon^2 u_2(x,y) + \dots \quad (18)$$

$$v(x,y) = \epsilon^2 v_1(x,y) + \epsilon^3 v_2(x,y) + \dots \quad (19)$$

$$p(x,y) = \epsilon p_1(x,y) + \epsilon^2 p_2(x,y) + \dots \quad (20)$$

into the Navier-Stokes equations in  $x$  and  $y$ .

From the power  $\epsilon^{-3}$ :  $\partial p_1 / \partial y = 0$ ,

$$\epsilon^{-2}; \quad \frac{\partial u_1}{\partial x} + \frac{\partial v_1}{\partial y} = 0$$

$$U_0 \frac{\partial u_1}{\partial x} + v_1 \frac{dU_0}{dy} = - dp_1 / dx \quad (21)$$

$$0 = \partial p_2 / \partial y,$$

$$\epsilon^{-1}; \quad \frac{\partial u_2}{\partial x} + \frac{\partial v_2}{\partial y} = 0$$

$$U_0 \frac{\partial u_2}{\partial x} + v_2 \frac{dU_0}{dy} + u_1 \frac{\partial u_1}{\partial x} + v_1 \frac{\partial u_1}{\partial y} = - \frac{dp_2}{dx} \quad (22)$$

In order to enforce a consistent matching between the upper and main decks, it is necessary to set

$$p_1 \equiv 0. \quad (23)$$

The validity of this assumption will be demonstrated by the self-consistency of the expansion. Otherwise, a physically unacceptable cause external to the triple-deck would drive the first-order perturbations, Equation (21). Alternatively, Messiter (1970) obtains the same result by expanding the pressure and stream function in terms of arbitrary gauge functions and determines the largest terms in the Navier-Stokes equations when the streamwise coordinate is stretched by an amount greater than  $R^{1/2}$ .

The solution to Equations (21) is

$$u_1 = A_1(x) \, dU_0/dy, \quad v_1 = -A_1'(x) \, U_0(y) \quad (24)$$

where

$$A_1(x) \rightarrow 0 \text{ as } x \rightarrow -\infty \quad (25)$$

and

$$A_1(x) - \delta_1 \left( \frac{x}{4} \right)^{1/3} \rightarrow 0 \text{ as } x \rightarrow \infty$$

from the boundary conditions, Equations (5) and (16). As  $y \rightarrow \infty$ ,  $U_0(y) \rightarrow 1$  and  $v_1 = -A_1'(x)$  leading to the downward displacement effect on the upper deck.

Stewartson also obtains a solution for Equations (22); however, here it is only necessary to note that, since  $U_0'$  and  $U_0'' \rightarrow 0$  as  $y \rightarrow \infty$ ,  $u_2 \rightarrow p_2$ . Therefore, for  $y \rightarrow \infty$ , the main deck expansions

have the form

$$\begin{aligned}
 u &\rightarrow 1 - \epsilon^2 p_2(x) + O(\epsilon^3) \\
 v &\rightarrow -\epsilon^2 A_1'(x) + O(\epsilon^3) \\
 p &\rightarrow \epsilon^2 p_2(x) + O(\epsilon^3)
 \end{aligned}
 \tag{26}$$

and cannot satisfy the boundary conditions given by Equation (6) necessitating the introduction of the upper deck.

The flow in the upper deck is inviscid and irrotational and  $x$  and  $Y$  are  $O(1)$ . The appropriate expansions are:

$$\begin{aligned}
 u &= 1 + \epsilon^2 U_2(x, Y) + \epsilon^3 U_3(x, Y) + \dots \\
 v &= \epsilon^2 V_2(x, Y) + \epsilon^3 V_3(x, Y) + \dots \\
 p &= \epsilon^2 P_2(x, Y) + \epsilon^3 P_3(x, Y) + \dots
 \end{aligned}
 \tag{27}$$

where the  $U_n$  and  $V_n$  are complex conjugates since the flow is potential and satisfies Laplace's equation. Matching with the main deck as  $y \rightarrow \infty$  and  $Y \rightarrow 0$

$$U_2(x, 0) = -p_2(x), \quad V_2(x, 0) = -A_1'(x), \quad P_2(x, 0) = p_2(x). \tag{28}$$

The pressure-displacement function relationship in the upper deck may be obtained using the properties of harmonic functions (Stewartson) or, equivalently, from linear airfoil theory (Messiter) as the skew-reciprocal Hilbert transformation

$$P_2(x) = \frac{1}{\pi} \int_{-\infty}^{\infty} \frac{A_1'(x_1) dx_1}{x - x_1}. \tag{29}$$



This equation and the assumption  $p_1 = 0$  must be satisfied to accomplish the match between the potential upper deck and the essentially inviscid main deck.

The necessity for the lower deck becomes evident when the main deck expansions are examined for  $y \rightarrow 0$ . Substituting the Taylor series for  $U_0(y)$  Equation (8) and Equations (24) into Equations (18) and (19),

$$u = [\lambda y + O(y^4)] + \epsilon[\lambda A_1(x) + O(y^3)] + O(\epsilon^2) + \dots \quad (30)$$

$$v = -\epsilon^2[\lambda y A_1'(x) + O(y^4)] + \epsilon^3[-A_1 A_1' - \lambda^{-1} p_2'(x)] + \dots, \quad (31)$$

and  $u \rightarrow 0$  as  $y \rightarrow 0$  as required by the no slip boundary condition on the plate. To remedy this problem the lower deck, where

$$u = \epsilon \tilde{u}_1(x, z) + \epsilon^2 \tilde{u}_2(x, z) + \dots \quad (32)$$

$$v = \epsilon^3 \tilde{v}_1(x, z) + \epsilon^4 \tilde{v}_2(x, z) + \dots \quad (33)$$

$$p = \epsilon^2 \tilde{p}_1(x, z) + \epsilon^3 \tilde{p}_2(x, z) + \dots \quad (34)$$

must be inserted. The conventional boundary-layer equations result when these expansions are substituted into the Navier-Stokes equations in  $x$  and  $z$ .

$$\partial \tilde{u}_1 / \partial x + \partial \tilde{v}_1 / \partial z = 0$$

$$\tilde{u}_1 \partial \tilde{u}_1 / \partial x + \tilde{v}_1 \partial \tilde{u}_1 / \partial z = -\partial \tilde{p}_1 / \partial x + \partial^2 \tilde{u}_1 / \partial z^2 \quad (35)$$

$$0 = \partial \tilde{p}_1 / \partial z$$

Since  $\tilde{p}_1$  is independent of  $z$ ,

$$\tilde{p}_1(x, z) = P_2(x, 0) = p_2(x) . \quad (36)$$

The boundary conditions along  $z = 0$  follow from Equation (7),

$$\tilde{u}_1 = \tilde{v}_1 = 0 \text{ if } x < 0, \quad \tilde{v}_1 = \partial \tilde{u}_1 / \partial z = 0 \text{ if } x > 0. \quad (37)$$

Upstream,  $\tilde{u}_1 \rightarrow \lambda z$  to match with the Blasius solution for small  $y$  as  $x \rightarrow -\infty$ , while downstream  $x \rightarrow \infty$  and

$$\tilde{u}_1 \rightarrow \frac{1}{3} \left( \frac{x}{4} \right)^{1/3} f'_0(\eta^*) \quad (38)$$

to match with Equation (15) the Goldstein inner wake solution. As  $z \rightarrow \infty$ , the lower deck must match with the main deck as  $y \rightarrow 0$  so

$$\tilde{u}_1 - \lambda z \rightarrow \lambda A_1(x) \quad (39)$$

since  $f'_0(\eta^*) \rightarrow 18 \lambda \eta^*$  as  $\eta^* \rightarrow \infty$  from Goldstein's (1930) solution.

The problem can now be reduced to a more universal form by scaling the variables to remove the constant  $\lambda$ . The fundamental problem of the trailing edge results when the affine transformation

$$\begin{aligned} x &= \lambda^{-5/4} X, \quad z = \lambda^{-3/4} Z, \quad \tilde{u}_1 = \lambda^{1/4} U(X, Z) \\ \tilde{v}_1 &= \lambda^{3/4} V(X, Z), \quad \eta^* = \lambda^{-1/3} \eta, \quad f_0 = \lambda^{1/3} g_0(\eta) \\ p_2 &= \lambda^{1/2} P(X), \quad A_1(X) = \lambda^{-3/4} A(X) \end{aligned} \quad (40)$$

is applied to the previous equations.

The problem is the existence of a physically acceptable solution of the boundary-layer equations

$$\frac{\partial U}{\partial X} + \frac{\partial V}{\partial Z} = 0, \quad U \frac{\partial U}{\partial X} + V \frac{\partial U}{\partial Z} = -\frac{dP}{dX} + \frac{\partial^2 U}{\partial Z^2} \quad (41)$$

with boundary conditions

$$U = 0, \quad V = 0 \quad \text{on } Z = 0, \quad X < 0$$

$$V = 0, \quad \partial U / \partial Z = 0 \quad \text{on } Z = 0, \quad X > 0$$

$$U - Z \rightarrow 0, \quad P \rightarrow 0 \quad \text{as } X \rightarrow -\infty \quad (42)$$

$$U - Z - A(X) \rightarrow 0 \quad \text{as } Z \rightarrow \infty$$

$$P \rightarrow 0, \quad U - \frac{1}{3} \left( \frac{X}{4} \right)^{1/3} g'_0(\eta) \rightarrow 0 \quad \text{as } X \rightarrow \infty$$

where  $P(X)$  and  $A(X)$  are related by the Hilbert integral

$$P(X) = \frac{1}{\pi} \int_{-\infty}^{\infty} \frac{A'(X_1) dX_1}{X - X_1} \quad (43)$$

Furthermore from Equation (18) and the boundary conditions, Equations (5) and (16)

$$A(X) \rightarrow 0 \quad \text{as } X \rightarrow -\infty, \quad A(X) \rightarrow 0.8920X^{1/3} \quad \text{as } X \rightarrow \infty \quad (44)$$

and from Equations (15) and (40)  $g_0$  satisfies the first-order Goldstein wake equation

$$g_0'''' + 2g_0 g_0'' - g_0'^2 = 0, \quad g_0(0) = g_0''(0) = 0$$

$$g_0'(0) = 7.6715, \quad g_0(\eta) \rightarrow 9 (\eta + 0.2360)^2 \quad \text{as } \eta \rightarrow \infty. \quad (45)$$

To answer this query originally posed by Stewartson (1969) is the purpose of this dissertation. The numerical computations reported in the succeeding chapters will demonstrate that the answer to this question is affirmative.

From the coordinate transformations Equations (3) and (40) and the lower deck expansion Equation (32) the skin friction is

$$\rho \nu \left. \frac{\partial u^*}{\partial y^*} \right|_{y^*=0} = \frac{\rho U_\infty^2 \lambda}{R^{1/2}} + \frac{\rho U_\infty^2 \lambda}{R^{1/2}} \left[ \left. \frac{\partial U}{\partial Z} \right|_{Z=0} - 1 \right] + O(R^{-5/8}) \quad (46)$$

where the first and last terms on the right-hand side are the Blasius value to  $O(\epsilon^7)$ . An integration along the plate produces the drag coefficient for one side of the plate

$$C_d = \frac{4\lambda}{R^{1/2}} + \frac{2}{\lambda^{1/4} R^{7/8}} \int_{-\infty}^0 \left[ \left. \frac{\partial U}{\partial Z} \right|_{Z=0} - 1 \right] dX + O(R^{-1}). \quad (47)$$

The following numerical procedure has determined the value of the above integral, subsequently labeled  $\theta_1$  by Stewartson (1974), to be 1.021.

Prior to proceeding to the numerical analysis it is necessary to determine the asymptotic structure of the velocity, pressure and displacement thickness for  $|X| \rightarrow \infty$  for use in the Hilbert integral subprogram.

To determine the asymptotic structure of the pressure it is only necessary to note that  $P(X)$  and  $A'(X)$  are complex conjugates from the harmonic property of  $U_2$  and  $V_2$  in the upper deck. Thus

$$P(X) \sim - \frac{1.784}{3^{3/2} |X|^{2/3}} \quad \text{if } X < 0 \quad (48)$$

and

$$P(X) \sim \frac{0.892}{3^{3/2} X^{2/3}} \quad \text{if } X > 0 \quad (49)$$

since

$$A'(X) \sim \frac{0.892}{3 X^{2/3}} \quad \text{if } X > 0 \quad (50)$$

and

$$A'(X) \sim 0 \quad \text{if } X < 0 \quad (51)$$

from Equation (44). The leading term in  $A(X)$  when  $X$  is large and negative can be determined by substituting

$$U = Z + 1.784 |X|^{-1} F_1'(\eta) + \dots \quad (52)$$

$$V = -2.248 |X|^{-5/3} (2F_1 + \eta F_1') + \dots \quad (53)$$

into the boundary-layer equation with result:

$$F_1'''' - 18\eta^2 F_1'' - 36(\eta F_1' - F_1) = -1.833 \quad (54)$$

$$F_1(0) = F_1'(0) = 0, F_1'(\eta) \rightarrow 0 \text{ as } \eta \rightarrow \infty, X \text{ large.}$$

The solution to Equation (54) may be represented in terms of the confluent hypergeometric function or its integral representation as shown by Messiter (1970) and Stewartson (1969). Here the solution was obtained numerically in order to obtain the initial velocity profile required to integrate the boundary-layer equation. The results are the same:

$$F_1''(0) = 0.6580, F_1'(\infty) = 0.1830 \quad (55)$$

so that when  $X$  is large and negative

$$\frac{\partial U}{\partial Z} \Big|_{z=0} = 1 + \frac{0.3106}{|X|^{4/3}} + \dots ; A(X) = \frac{0.3265}{|X|} + \dots \quad (56)$$

Similarly, when  $X$  is large and positive the form of  $A(X)$  must be determined from the boundary-layer equations. On substituting the expansions

$$U = \frac{1}{3} \left( \frac{X}{4} \right)^{1/3} g_0'(\eta) + \frac{1}{3} \left( \frac{X}{4} \right)^{1-n/3} g_n'(\eta) + \dots \quad (57)$$

$$V = -\frac{1}{6} \left( \frac{X}{4} \right)^{-1/3} [2g_0 - \eta g_0' + \left( \frac{X}{4} \right)^{-n/3} ((2-n)g_n - \eta g_n')] + \dots \quad (58)$$

and  $P(X)$  from Equation (49) into the boundary layer equation we find  $g_n$  must satisfy

$$g_n'''' + 2g_0 g_n'' - (2-n)(g_0' g_n' - g_0'' g_n) = -1.2263$$

$$g_n(0) = g_n'(0) = 0 \quad \text{for } n = 4. \quad (59)$$

A third boundary condition is required to determine a unique solution to Equation (59). Stewartson has shown that as  $\eta \rightarrow \infty$  the requirement of exponential decay must be imposed to avoid a mismatch with the Goldstein wake. This requirement, however, leads to an infinity of terms associated with the eigenfunctions of the expansion for  $U$  given by Equation (57). The first eigenfunction is associated with  $V$  and corresponds to  $n = 3$  in Equation (59).

It is

$$g_3 = \frac{1}{4} b_1 (2g_0 - \eta g_0') \quad (60)$$

where  $b_1$  is an arbitrary constant to be found from the numerical procedure. The contribution to  $U$  from the pressure term is determined from the numerical integration of Equation (59) for  $n = 4$ . On substituting the results

$$g_4'(0) = 0.039, \quad g_4'(\infty) = -0.0527 \quad (61)$$

into Equation (57) we find

$$A(X) = 0.8920X^{1/3} + 0.8920b_1X^{-2/3} - 0.070X^{-1} + \dots \quad (62)$$

$$U(X,0) = 1.611X^{1/3} + 1.611b_1X^{-2/3} + 0.052X^{-1} + \dots \quad (63)$$

for  $X$  large and positive. Again utilizing the harmonic property of  $P(X)$  and  $A'(X)$ , the expansions

$$P(X) \sim \frac{0.8920}{3\sqrt{3} X^{2/3}} \left(1 + \frac{2b_1}{X}\right) - \frac{0.0816 \log X}{X^2} + \frac{d_1}{X^2} + \dots \quad (64)$$

for  $X$  large and positive and

$$P(X) \sim -\frac{1.7840}{3\sqrt{3}|X|^{2/3}} \left(1 + \frac{2b_1}{|X|}\right) - \frac{0.0816 \log X}{X^2} + \frac{d_1}{X^2} + \dots \quad (65)$$

for  $X$  large and negative are readily obtained.

The  $\log X$  terms in  $P(X)$  are required by the  $X^{-1}$  term in  $A(X)$  and similarly any integer power of  $X$  in either  $A(X)$  or  $P(X)$  will induce  $\log X$  terms in the other due to their harmonic property.

The constant multiplying the third term in each of Equations (62), (64) and (65) differs from the constant given in Stewartson's (1969) paper. The constant is determined by  $g_4'(\infty)$ , found here by employing a fourth-order Runge-Kutta numerical integration algorithm (Ralston and Wilf (1960)) to solve Equation (59) with  $n = 4$ . The signs on the first term of Equation (64) and the second term of Equation (65) were also found to be opposite to those given by Stewartson (1969).

The preceding equations are all that are necessary for the numerical solution except for the definition of  $\lambda_1$ , the factor multiplying the Blasius skin friction at  $X = 0$ . By trial Stewartson finds the following method of setting up the expansion of the solution about  $X = 0$  to be consistent. Assuming that on the plate where  $X = 0$  the velocity profile is differentiable, he writes

$$U(0-, Z) \equiv U_1(Z), U_1'(0) = \lambda_1 \neq 0. \quad (66)$$

Further assuming that in the wake where  $X = 0^+$

$$\frac{dP}{dX} \sim C_0 X^{-1/3} \quad (67)$$

and

$$U \sim \frac{1}{3} \left(\frac{X}{4}\right)^{1/3} G_0'(\eta) \text{ near } Z = 0 \quad (68)$$



he finds  $G_0$  satisfies

$$G_0'''' + 2 G_0 G_0'' - (G_0')^2 = 27 C_0^2 \lambda_1^{4/3} \quad (69)$$

for small  $\eta$ , with boundary conditions

$$G_0(0) = G_0''(0) = 0 \text{ and } G_0'(\infty) = 18 \lambda_1. \quad (70)$$

Also, to avoid a contradiction in the pressure expansion,

$$G_0' - 18 \lambda_1 \eta \rightarrow 0 \text{ as } \eta \rightarrow \infty.$$

The solution was found by Hakkinen and Rott (1965) and rechecked numerically here. Thus,

$$G_0'(0) = 3(2 \lambda_1)^{2/3} (0.8991) \quad (71)$$

and

$$C_0 = \lambda_1^{4/3} [0.4089]. \quad (72)$$

Stewartson then reaches the following tentative conclusions which the ensuing numerical analysis will demonstrate to be quite accurate.

1. The skin friction is finite as  $X \rightarrow 0^-$  and  $\lambda_1 > 1$ .

$$2. \quad U(X, 0) = 0.8991 \lambda_1^{2/3} X^{1/3} + O(X^{2/3}). \quad (73)$$

$$3. \quad P(X) = P_0 + P_1 X + O[X^2 \log(-X)] \quad (74)$$

when  $X < 0$  and

$$4. \quad P(X) = P_0 + 0.6133 \lambda_1^{4/3} X^{2/3} + O(X) \quad (75)$$

when  $X > 0$ ,

where  $P_0$  is a negative constant and  $P_1$  is also a constant.

For the convenience of the reader, the constants have been determined by  $h^2$  - extrapolation (Beckenbach (1961)) of the present numerical data to be  $\lambda_1 = 1.343$ ,  $P_0 = -0.388$  and  $P_1 = -0.278$ .

The match with the central region where  $x^*$  and  $y^*$  are  $O(\epsilon^6 L)$  will not be undertaken here since yet another region where  $x^*$  and  $y^*$  are  $O(\epsilon^4 L)$  intervenes and the elucidation of its properties will have to await further study. Its properties are not required for the determination of the largest perturbations which occur in the present  $O(\epsilon^3 L)$  region. Throughout this analysis it has been tacitly assumed that  $\epsilon \ll 1$  or  $R \gg 1$ , however the data comparisons will show that the present theory is accurate for  $R \rightarrow 1$ . This unexpected result also somewhat negates the requirement for higher-order terms.

## CHAPTER III

### THE NUMERICAL PROCEDURE

The computer program used in this study evolved from a boundary-layer program developed by Burggraf (1969). The essential elements of the final program will be described here. The details and the evolution of the program occupy towering columns of printer paper and over three years of analysis. All computations have been carried out on a CDC 6600 digital computer.

The main program consists of three main iteration loops as shown on Figure 1. Within this program, two subroutines are required. One subroutine, indicated by the upper large rectangle of Figure 1, iteratively computes the boundary-layer velocity profiles of the lower deck using an implicit Crank-Nicholson type-difference analogue. The other subroutine, indicated by the lower large rectangle of Figure 1, computes the Hilbert transformation of the pressure which is the slope of the displacement function,  $A(X)$ . As shown, the innermost of the three loops adjusts the pressure gradient at a given streamwise station until the boundary-layer subroutine produces a velocity profile with the desired  $A(X)$ . The middle loop provides the correct boundary conditions and advances the computation through its streamwise course and the outer loop compares displacement functions,  $A(X)$ , resulting from successive streamwise traverses through the entire lower deck

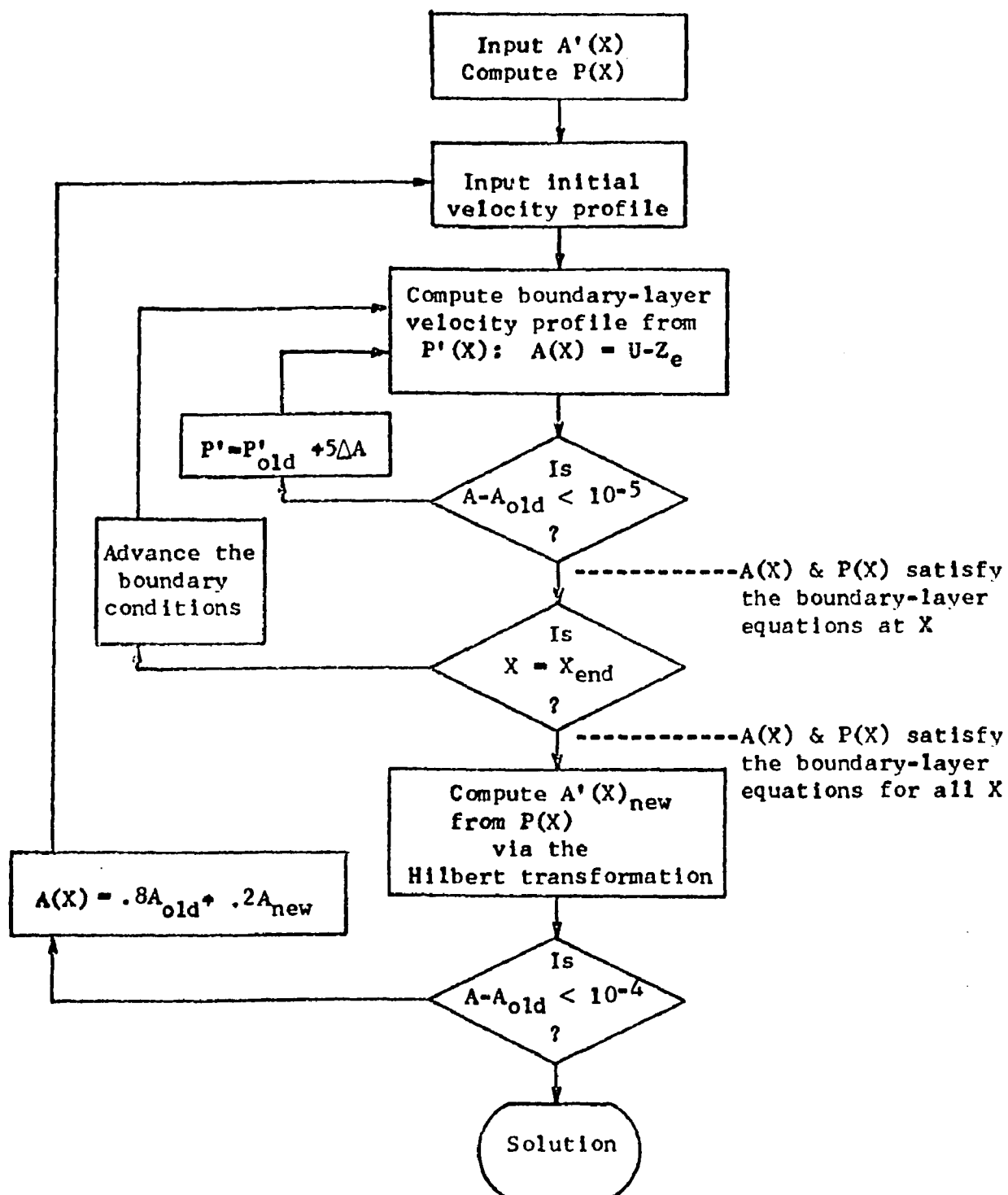


Fig. 1.--A Flow Chart of the Main Program

until the solution is obtained. Discussion of the subroutines will be deferred until their relationship to the main program is delineated.

All computations have been performed in the X,Z - coordinate system of Equation (40). The streamwise interval must be symmetric about the trailing edge  $X = 0$  and divided into an even number of equal increments of length  $\Delta X$ . Intervals extending from -3 to +3, -6 to +6, -9 to +9, and -12 to 12 with  $\Delta X = 0.1, 0.05, 0.025,$  and  $0.0125$  have been employed to insure the accuracy of the computations. The Z or normal coordinate direction is also divided into an even number of equal increments of length H. The thickness of the layer is limited by the computational time required and  $Z_e = 6, 8,$  and  $9$  have been used with increments  $H = 0.1$  and  $0.05$ . A finer grid or a thicker layer would require prohibitively long central processor time. The shortest run (20 minutes, 21,000 central memory locations) which produces reliable, accurate results was found to be the case where  $-6 \leq X \leq 6,$   $0 \leq Z \leq 6$  with  $\Delta X = 0.05$  and  $H = 0.1$ . All subsequent numerical investigations were performed to ascertain the effects of various changes on the above case.

#### Input Data

The boundary-layer equations are parabolic and require that the initial velocity profile and the boundary conditions along the streamwise edges are prescribed. The downstream velocity profile cannot be prescribed and serves as a check on the computations.

The initial velocity profile is required to initiate the boundary-layer computations during each cycle of the outer loop and ultimately affects the final solution. The initial velocity profile

for  $X$  large and negative has been obtained for the various  $H$  step sizes by numerically integrating Equation (54) using Hamming's modified predictor-corrector method (Ralston and Wilf (1960)) and substituting the results into Equation (52). The velocity profile, magnified by the subtraction of the linear portion, is presented in Figure 2. It should be noted that as  $Z \rightarrow 9$  the profile becomes vertical indicating that the boundary condition given by Equation (42) is not being enforced prematurely. The initial velocity profile has been checked by comparison with the velocity profile resulting from the computations initiated further upstream (see Appendix A).

The final set of input data required is an estimate for the displacement function,  $A(X)$ , or the pressure,  $P(X)$ . Either can be calculated from the other by the skew-reciprocal Hilbert transformation, Equation (43). Both are required to start the three main loops as shown on Figure 1. Presumably, any reasonable guess would suffice; however, the closer the guess is to the final solution, the shorter is the running time required. Realizing this, a function of the form

$$A'(X) = \frac{C_1}{C_2^2 + X^2} + C_3 X^{2/3} \exp(C_4 X) \quad X \leq 0$$

and

$$A'(X) = \frac{C_5}{C_6^2 + X^2} + \frac{C_7 X^{2/3}}{C_8^4 X^{4/3}} + \frac{C_9}{C_{10}^2 + X^{5/3}} \quad X > 0$$

(76)

was developed by modifying Messiter's first guess for the form of the slope of the displacement thickness to agree with the asymptotic

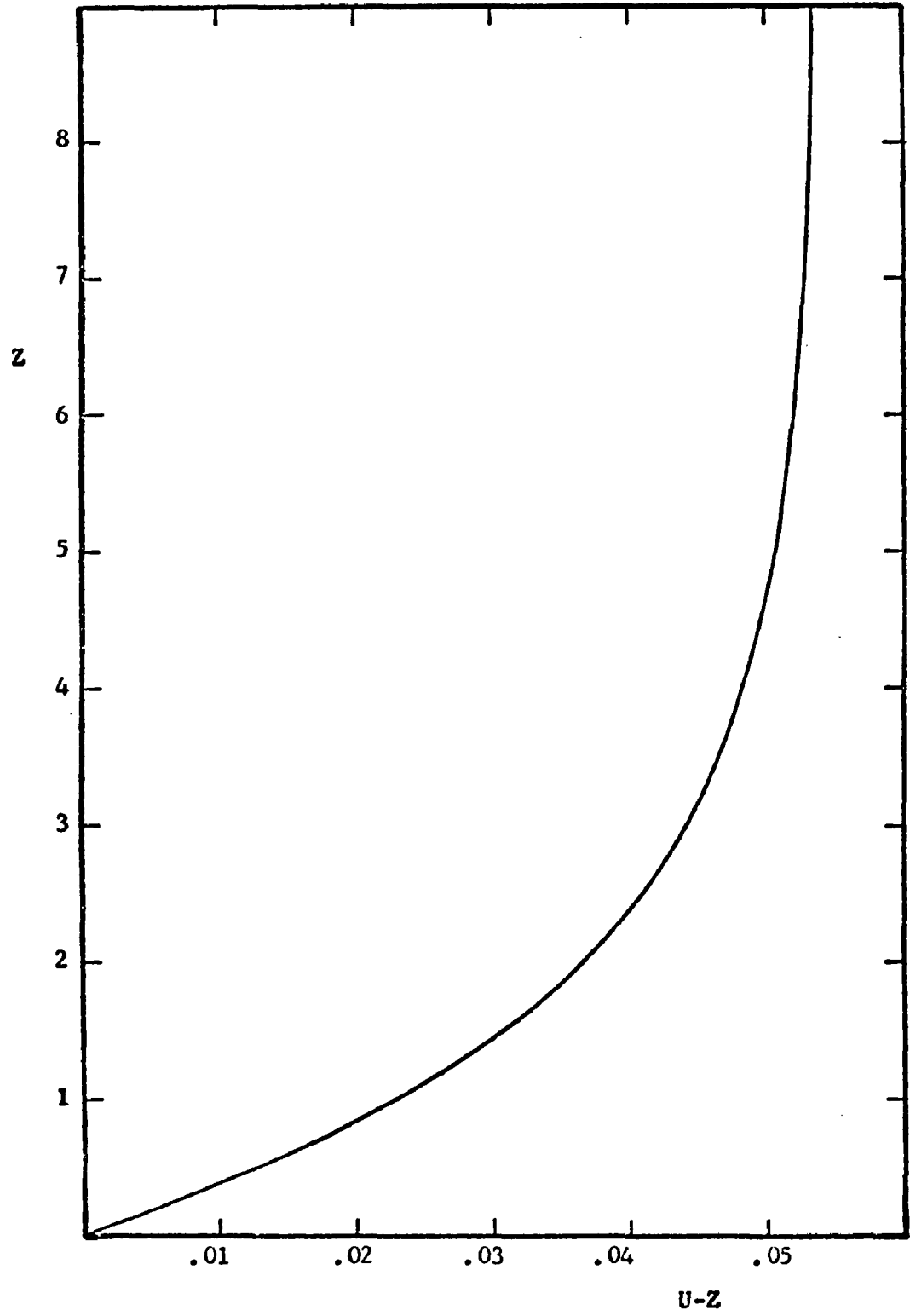


Fig. 2.--Initial Velocity Profile at X = -6

behavior predicted by Equations (56) and (62). Messiter's values for the  $C_i$  were:  $C_1 = .327$ ,  $C_2 = 1.142$ ,  $C_3 = -.594$ ,  $C_4 = 3.00$ ,  $C_5 = .624$ ,  $C_6 = 1.580$ ,  $C_7 = .297$  and  $C_8 = 1.00$ , where here  $C_1 = .3265$ ,  $C_2 = 1.011$ ,  $C_3 = -.4511$ ,  $C_4 = 1.500$ ,  $C_5 = .6054$ ,  $C_6 = 1.7921$ ,  $C_7 = .2974$ ,  $C_8 = 1.100$ ,  $C_9 = .1308$ , and  $C_{10} = 1.000$ . Messiter (1970) did not include the term containing  $C_9$  and  $C_{10}$ , thus effectively his  $C_9 = 0$ .

An estimate for the pressure gradient is also required as initial data as shown on Figure 1. It is readily obtained from the numerical differentiation of the pressure resulting from the Hilbert transformation of Equation (76). Figure 1 also shows that one cycle through the middle loop generates the pressure required to satisfy the boundary-layer equations for the  $A(X)$  given by the numerical integration of Equation (76). Thus, at the end of one cycle of the program, one pressure curve satisfies the Hilbert transformation and the other satisfies the boundary-layer equations. The  $C_i$  given above for Equation (76) were determined by a comparison of the two pressure curves. Many divergent attempts were required to develop the final convergent numerical procedure. They were not entirely useless since each afforded the opportunity to compare the pressure curves and adjust the  $C_i$  using data from prior unsuccessful runs to determine the trends in the pressure curves with respect to the  $C_i$ . Figure 3 compares the two pressure curves, the one that satisfies the Hilbert transformation and the other that satisfies the boundary-layer equations. The comparison shows that the pressure curves are in fair



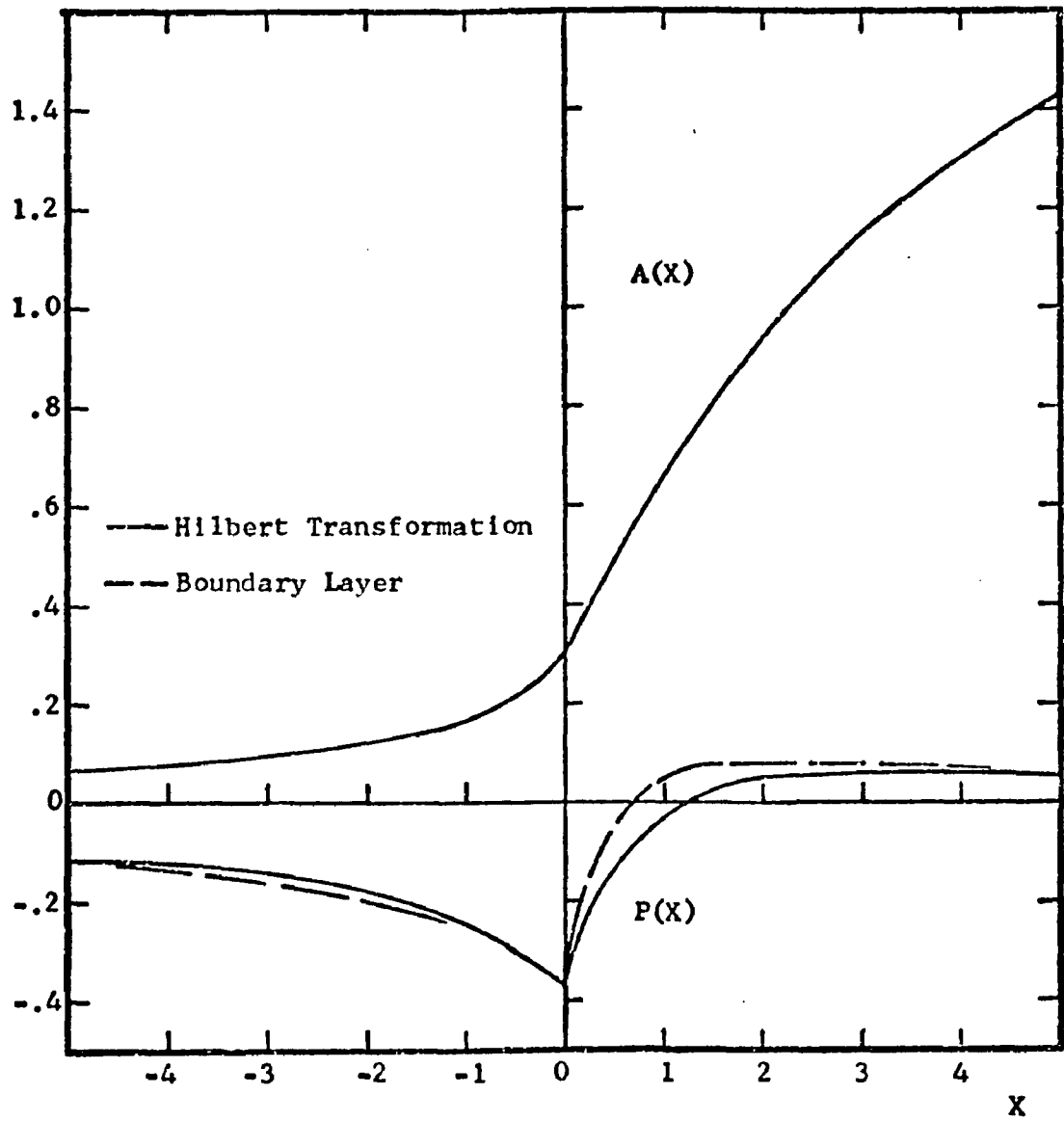


Fig. 3.--Initial Estimate for the Displacement Thickness

agreement which indicates that Equation (76) provides a good starting approximation for the final iteration procedure.

The final iteration procedure has been shown to converge to the same solution using either Messiter's form or the revised form of  $A'(X)$  as input data. A 22 per cent increase in computational time is required using Messiter's form of  $A'(X)$  due to the additional iterations required for convergence, however.

### The Main Program

The main program, shown in Figure 1, is comprised of three nested loops which utilize the preceding input data to produce the solution. The middle loop performs the necessary bookkeeping tasks of selecting corresponding values for the streamwise station  $X$ , the pressure gradient  $P(X)$ , the displacement thickness  $A(X)$ , and the previous velocity profile for the inner loop from the input data arrays.

The problem addressed by the inner loop of the main program is to solve the boundary-layer equations of the lower deck for that pressure gradient  $P'(X)$  which will produce the requested edge velocity,  $U_e$ , and thereby  $A(X) = U_e - Z_e$  with  $Z_e$  fixed. The method of solution is to compute the velocity profile using the iterative boundary-layer subroutine with the input  $P'(X)$ , determine the difference between the computed  $A(X)$  and the requested  $A(X)$ , then use this difference to correct  $P'(X)$  until the desired  $A(X)$  is achieved to within  $10^{-5}$ , the inner loop error tolerance. Symbolically,  $P'(X)_{\text{new}} = P'(X)_{\text{old}} + \Delta A(X)/(dA/dP')$  where  $dA/dP' = dU_e/dP'$  for fixed  $Z_e$ . The problem therefore is reduced to the determination of  $dU_e/dP'$ . The solution was obtained originally by differentiating the boundary-layer equation

with respect to  $P'(X)$  to obtain a partial differential equation for  $\partial U/\partial P'$ . This equation was then numerically integrated across the boundary layer in order to obtain  $dU_e/dP'$ . This subroutine and the similar boundary-layer subroutine each had to be employed during each cycle through the inner loop. After several runs and considerable data analysis it was determined that the optimum  $dU_e/dP'$  is nearly 0.2 for all  $X$ . The inner loop will converge more slowly if other values of  $dU_e/dP'$  are used. This discovery permitted the removal from the inner loop of the entire time-consuming subroutine and its attendant bookkeeping and reduced the run time to a manageable figure. After several iterations, depending upon the streamwise station, the program exits from the inner loop with the  $P'(X)$  required to produce the requested  $A(X)$  to within .00001, and proceeds stepwise downstream via the middle loop. At the completion of the middle loop, the  $P'(X)$  required to produce the requested  $A(X)$  has been determined for all  $X$ . To determine  $P(X)$  the pressure at the initial station must be found. The first-order term is known; from Equation (64), however, the second and fourth terms contain the unknown constants  $b_1$  and  $d_1$ . The slope of the displacement function  $A(X)$  may be changed by shifting the entire pressure curve by a constant value since the Hilbert integral of a constant is another constant for the finite limits necessitated by computer storage. Upstream  $A(X)$  is known to  $O(X^2)$  from Equation (56) and therefore  $A'(X)$  is known through  $O(X^2)$ . Thus, the pressure curve can be computed using an initial pressure shifted such that  $A'(X)$  is correct through  $O(X^2)$  at the initial point. Alternatively, a value of  $b_1$  could be obtained from the values of  $A(X)$  or  $U(X,0)$  from

the previous iteration using Equation (62) or Equation (63) and then used to determine the initial pressure. Both methods were tried; the former was selected since the overall convergence was considerably improved without significantly affecting the final results. Enforcing the correct asymptotic behavior of  $A'(X)$  effectively damps the oscillations which occur during the iteration cycles. A study of the effects of the pressure shift has been relegated to Appendix B. Thus, the pressure that satisfies the boundary-layer equations is generated in the middle loop.

The outer loop now computes the  $A'(X)$  corresponding to the new  $P(X)$  from the Hilbert transformation subroutine and, since the initial value of  $A(X)$  is known to  $O(X^2)$  from Equation (56), a new  $A(X)$  can be obtained by the trapezoidal rule. Comparing the new  $A(X)$  with the  $A(X)$  from the previous iteration determines if the program has converged. If not,  $A(X)$  is replaced according to the formula

$$A(X) = KA(X)_{\text{old}} + (1-K)A(X)_{\text{new}} \quad (77)$$

and the outer loop re-initiates the streamwise traverse of the lower deck until the differences between succeeding  $A(X)$  iterates is less than  $10^{-4}$ .

It has been found by trial and error that  $K = 0.8$  will produce a convergent iteration scheme. The outer loop will also converge with  $K = 0.9$  or  $K = 0.7$  but  $K = .8$  is the best of these three values. The outer loop will not converge if  $K = 0.5$  or  $K = 0$ .

### The Hilbert Transformation

The range of the Hilbert integral extends from negative infinity to positive infinity. The integrand is singular at the point under consideration. The functions  $A'(X)$  and  $P(X)$  are slowly approaching zero at both ends of the range and  $P(X)$  must contain a zero within the range. Additionally, it is highly desirable that the method use data at the same streamwise locations as the input data and the boundary-layer subroutine and return the pressure or displacement thickness results at the same streamwise locations. This feature eliminates the requirement for time-consuming data fitting and interpolation to adjust the output from the subroutines to be compatible with the main program. All these requirements present a formidable numerical problem.

Fortunately, the asymptotic expansions for large  $|X|$  are known for  $A(X)$ , given by Equations (56) and (62), and  $P(X)$ , given by Equations (64) and (65). The first two terms of these expansions have been integrated in closed form using the substitution  $t^3 = \pm X_1/X$  and the method of partial fractions (Equation (80), see below). Integrals of this form may also be found in Petit Bois (1961). The limits extend from minus infinity to the point where the numerical integration begins or from the point where the numerical integration terminates to positive infinity, whichever is applicable. This effectively splits the range into three parts and reduces the doubly-infinite range Hilbert transformation to a finite range Cauchy integral plus closed form expressions which account for the infinite portions of the range where the respective expansions are applicable.

The origin  $X = 0$  must also be treated separately to insure that the expressions do not contain functions or function arguments that tend to an undefined limit. The remaining finite-range Cauchy integral has been treated analytically by subtracting the singularity from the integrand (Davis and Rabinowitz (1967)).

We now consider the computation of

$$A'(X) = -\frac{1}{\pi} \int_{-\infty}^{\infty} \frac{P(X_1)dX_1}{X-X_1}, \quad (78)$$

the skew-reciprocal inverse of Equation (43) (Titchmarsh (1937)) to illustrate the method. Considering only the first terms of Equations (64) and (65) (the second terms may be reduced to the same form plus an elementary form by partial fractions), Equation (78) becomes

$$A'(X) = \frac{2K}{3} \int_{-\infty}^a \frac{dX_1}{(-X_1)^{2/3}(X-X_1)} + \frac{1}{\pi} \int_a^e \frac{P(X_1)dX_1}{X-X_1} - \frac{K}{3} \int_e^{\infty} \frac{dX_1}{(X_1)^{2/3}(X-X_1)} \quad (79)$$

where  $K = -0.892/\pi^{3/2}$  and the limits  $a$  and  $e$  are arbitrary, but large. The center portion of the integral is evaluated for each outer iteration using the following numerical integration procedure. It is evident that by considering various endpoints for the center integral, the accuracy of the approximations for the outer portions of the range may be assessed. For  $X = 0$  the integrand is  $X_1^{-5/3} dX_1$  which is readily

integrated. More generally, the substitutions  $t^3 = X_1/X$  and  $t^3 = X_1/(-X)$  when  $X < 0$  and  $t^3 = -X_1/X$  and  $t^3 = X_1/X$  when  $X > 0$  will reduce the integrands of the first and last integrals of Equation (79) to the form  $dt/1 \pm t^3$ . The antiderivative has the form

$$\frac{1}{6} \log \frac{(t \pm 1)^2}{t^2 \pm t + 1} \pm \frac{1}{3} \operatorname{arctg} \frac{t^{3^{1/2}}}{2 \pm t} \quad (80)$$

which remains finite at the infinite limits.

The integrals of the asymptotic expansions of  $A'(X)$  are evaluated in a similar manner and the range is segmented in an identical manner to insure compatibility with the main program.

The center portion of the integral is performed by subtracting the singularity, whether  $A'(X)$  or  $P(X)$  is in the integrand. The two subroutines differ in the analytic expressions which account for the infinite portions of the range.

The singularity in the integral is removed by subtraction, thus

$$\int_a^e \frac{P(X_1)dX_1}{X_1-X} = \int_a^e \frac{P(X_1)-P(X)dX_1}{X_1-X} + P(X) \int_a^e \frac{dX_1}{X_1-X} \quad (81)$$

Splitting the range about the point  $X$ ,

$$\int_a^e \frac{P(X_1)dX_1}{X_1-X} = \int_a^{X-} + \int_{X+}^{X+} + \int_{X+}^e \frac{P(X_1)-P(X)}{X_1-X} dX_1 + P(X) \log \left| \frac{e-X}{a-X} \right| \quad (82)$$

The first and third integrals are nonsingular and the trapezoidal rule has been employed for their evaluation. Assuming the integrand may be expanded in a Taylor series about X the center integral,

$$\int_{X-\Delta X}^{X+\Delta X} \frac{P(X_1)-P(X)}{X_1-X} dX_1 = 2 \Delta X P'(X) + O(\Delta X^3) \quad (83)$$

which may be evaluated using any standard differencing method for  $P'(X)$ . In order to assess the accuracy of this numerical method a second method for treating Cauchy integrals (Collatz (1961)) was used along with three of Van Dyke's (1959) airfoil integrals. The results of the evaluation, contained in Appendix A, demonstrate that subtracting the singularity is the more accurate of these methods for treating Cauchy integrals.

When X is at either of the endpoints of the finite numerical range, a or e, the above numerical procedures do not apply. The method of computing the integral at the endpoints consists of allowing the limits of the integrals of the asymptotic expansions to overrun the singularity at the endpoint by  $\Delta X$  and performing the remaining non-singular numerical portion using the trapezoidal rule. Thus, the endpoint singularity is contained within the range of the integral of the asymptotic contribution. The procedure of merely ignoring the singularity within the range of a Cauchy integral has been justified by Mangler (1951).

The skew-reciprocal property of the Hilbert transformation permits the simultaneous error analysis of both the  $P(X)$  and  $A'(X)$  subroutines. One subroutine computes  $A'(X)$  from  $P(X)$  by assembling



the appropriate expressions for the integrals of the asymptotic expansions of  $P(X)$  and the above numerical methods. Particular attention is required to insure that each method is employed only within its range of validity, i.e.,  $X = a$ ,  $X < 0$ ,  $X = 0$ ,  $X > 0$  or  $X = e$ . The other subroutine computes the pressure,  $P(X)$ , from  $A'(X)$  by the same procedure utilizing the appropriate expressions resulting from the integrals of the asymptotic expansions of  $A'(X)$ . Subsequent error analysis and programming checks were facilitated by the skew-reciprocal nature of the subprograms which were combined in a short flip-flop program. This error analysis, using Messiter's (1970) form of  $A'(X)$ , is contained in Appendix A. The error analysis of the present converged numerical results is reported in the following discussion of the results.

#### The Boundary-Layer Subroutine

This is the most standard of the subroutines in the entire program, yet the most crucial since it is required several times during each cycle of the innermost loop. This subroutine solves the boundary-layer equations of the lower deck, given by Equation (41) as

$$\frac{\partial U}{\partial X} + \frac{\partial V}{\partial Z} = 0, \quad U \frac{\partial U}{\partial X} + v \frac{\partial U}{\partial Z} = - \frac{dP}{dX} + \frac{\partial^2 U}{\partial Z^2},$$

by an iterative procedure and thus constitutes another loop within the inner loop (See Fig. 1) of the main program. The boundary conditions are given by Equation (42) as

$$U = 0, V = 0 \text{ on } Z = 0, X < 0,$$

$$V = 0, \partial U / \partial Z = 0 \text{ on } Z = 0, X > 0, \quad (84)$$

and  $\partial U / \partial Z \rightarrow 1$  as  $Z \rightarrow \infty$ .

The pressure gradient and the velocity profile at the previous stream-wise station,  $X - \Delta X$ , are required as input data to compute the velocity profile  $U(Z)$  at  $X$ .

The introduction of the stream function and the application of the Crank-Nicholson differencing scheme to the boundary-layer momentum equation results in a matrix equation of the form

$$\sum_j C_{ij} U_j = R_i \quad (85)$$

The  $C_{ij}$  matrix is tridiagonal with elements that contain the initially unknown  $U_j$  as shown in Appendix C. This matrix equation was solved by employing modified Gaussian elimination with back substitution (Richtmyer and Morton (1967)) and the continuity equation to update the stream function during each cycle. Convergence was achieved in 10-20 cycles when the successive velocity profiles were within the specified error tolerance,  $10^{-6}$ . A more efficient boundary-layer subroutine using Newton iteration could have considerably reduced the computing time required, since this iteration is within the inner loop of the main program.

The boundary conditions are enforced by prescribing values for specific elements of the matrix or vectors. For example, with the representation of  $C_{ij}$  by its elements

$$B_j U_{j+1} + U_j + A_j U_{j-1} = R_j, \quad (86)$$

the boundary condition  $\partial U/\partial Z = 1$  requires that  $A_j = -1$  and  $R_j = -H$  at the outer edge. The boundary condition on the wake centerline,  $\partial U/\partial Z = 0$ , was enforced by requiring that  $B_1 = -1$  and either  $R_1 = 0$  or

$$R_1 = -\frac{H^2}{2} \left[ U_1 \frac{\Delta U_1}{\Delta X} + P'(X) \right] \quad (87)$$

The formulas for the  $A_j$ ,  $B_j$ , and  $R_j$  are contained in Appendix C.

The effects of the higher-order form of the boundary condition given by Equation (87) and the accuracy of the subroutine in general were assessed by the momentum-integral method. Integrating Equation (41) across the layer,

$$\partial (U_{Z_e}^2 \theta) / \partial X - A'(X) F(Z_e) - Z_e P'(X) + 1 - \partial U / \partial Z \Big|_{Z=0} = 0 \quad (88)$$

where  $U_{Z_e}^2 \theta = - \int_0^{Z_e} U(U - U_{Z_e}) dZ$ ,  $Z_e$  is the value of  $Z$  at the outer edge,

and  $F$  satisfies the continuity equation. Equation (88) is satisfied by the velocity profiles resulting from the boundary-layer subroutine to better than one per cent over the majority of the streamwise extent of the layer. The maximum momentum imbalance may reach nine per cent of the value of the first term of Equation (88) at the point immediately aft of the trailing edge; however, it diminishes to less than one per cent four points downstream. The nine per cent error in Equation (88) amounts to an error in the fourth significant figure of the velocity which is consistent with the numerical procedure. These

errors are slightly increased for the boundary condition  $R_1 = 0$ , consequently Equation (87) was used for the wake boundary condition during the final data runs.

Additionally, many known solutions of the boundary-layer equations were employed to ascertain the accuracy of the boundary-layer subroutine. Rosenhead (1961) has tabulated the Blasius velocity profile to six significant figures and the velocity profile for the boundary-layer flow along a cylinder near the forward stagnation point to seven figures. These solutions afforded an excellent opportunity to check the numerical method. In particular, it was found that agreement to five significant figures could be obtained with a velocity profile error tolerance of  $10^{-6}$ . Diminishing the error tolerance to  $10^{-9}$  did not significantly improve the results for the same mesh. It did, however, increase the number of iterations required for convergence from 13 to 21. All succeeding results were obtained with a  $10^{-6}$  error tolerance on the velocity profile for this reason.

Further, agreement to the number of significant figures reported with the data of Rosenhead (1961) for several Falkner-Skan flows and convergent channel flow was obtained. For the adverse gradient Howarth flow,  $U = U_\infty (1 - X^*/L)$ , the point of vanishing skin friction was computed to occur at  $X^*/L = 0.12$ , in agreement with the data reported by Rosenhead (1961) of Howarth ( $X^*/L = 0.12$ ) and Leigh ( $X^*/L = 0.1198$ ). The mesh size was  $\Delta Z = .025$ ,  $\Delta X = 0.005$  and the outer edge of the boundary layer was at  $Z_e = 4$ .

A test flow of special relevance was the computation of Goldstein's wake function,  $f_0$ , from Equation (11). The present

results differ from Goldstein's (1930) by less than the 0.5 per cent at  $\eta = 0$  and less than 0.05 per cent at  $\eta = 1.4$ . Goldstein's results are probably the more accurate since he employed a smaller step-size and higher-order of accuracy integration method.

Concluding this section treating the numerical procedure, we reiterate how the limits on the entire program arise. The overall computations are limited by the central processor time required. Central memory storage requirements are not a limiting factor. The bulk of the computing time is required by the inner loop because it contains the iterative boundary-layer subroutine. The error tolerance of the boundary-layer subroutine is  $10^{-6}$  to achieve the most accuracy with the minimum number of iterations. Typically, about 10 iterations per velocity profile are required by this subroutine. The error tolerance of the inner loop that incorporates the boundary-layer subroutine is  $10^{-5}$  and it requires about five iterations to converge using  $dU_e/dP' = 0.2$ . The inner loop is required to converge at each streamwise station and either 240 or 480 stations have been employed in the main loop. The error tolerance of the outer loop is  $10^{-4}$  and it requires about 20 streamwise traverses to converge when started with the initial  $A'(X)$  given by Equation (76) and  $K=0.8$  in Equation (77).

The relationship between the error tolerances:  $10^{-6}$  on the boundary-layer subroutine,  $10^{-5}$  on the inner loop and  $10^{-4}$  on the outer loop, must be approximately satisfied for convergence of the outer loop to the specified tolerance. If the inner loop-error tolerance is relaxed, the error in the computations will approach a small value which is greater than the outer loop error tolerance.

## CHAPTER IV

### THE RESULTS

The final computations have been performed with the numerical endpoints at  $X = \pm 6$  or  $\pm 12$  and the outer edge of the lower deck located at  $Z_e = 9$ . The step sizes  $H = 0.05$  or  $0.1$  with  $\Delta X = 0.05$  or  $0.025$  were employed in the various combinations permitted by the computational time required. Certainly several additional combinations are desirable; however, the central processor time required and cost make these runs impractical at present. For example, diminishing  $H$  to  $0.025$  and  $\Delta X$  to  $0.0125$  simultaneously would require over one-half hour of CDC 6600 central processor time for each cycle through the main loops. The ensuing tabular results have been obtained by performing  $h^2$ -extrapolation (Beckenbach (1961)) on the relevant data.

The skin friction which increases smoothly from the Blasius value upstream to the value  $\lambda_1$  at the trailing edge of the triple-deck region is shown in Figure 4. The plotted values of  $\partial U / \partial Z \Big|_{Z=0}$  are the ratio of the actual skin friction to the Blasius skin friction from Equation (46) and the coordinate transformations of Equations (40) and (2). Thus  $\partial U / \partial Z \Big|_{Z=0} = 1$  denotes the Blasius value of the skin friction.

The numerical skin friction joins smoothly to the asymptotic behavior predicted by Equation (56) when the velocity profile resulting

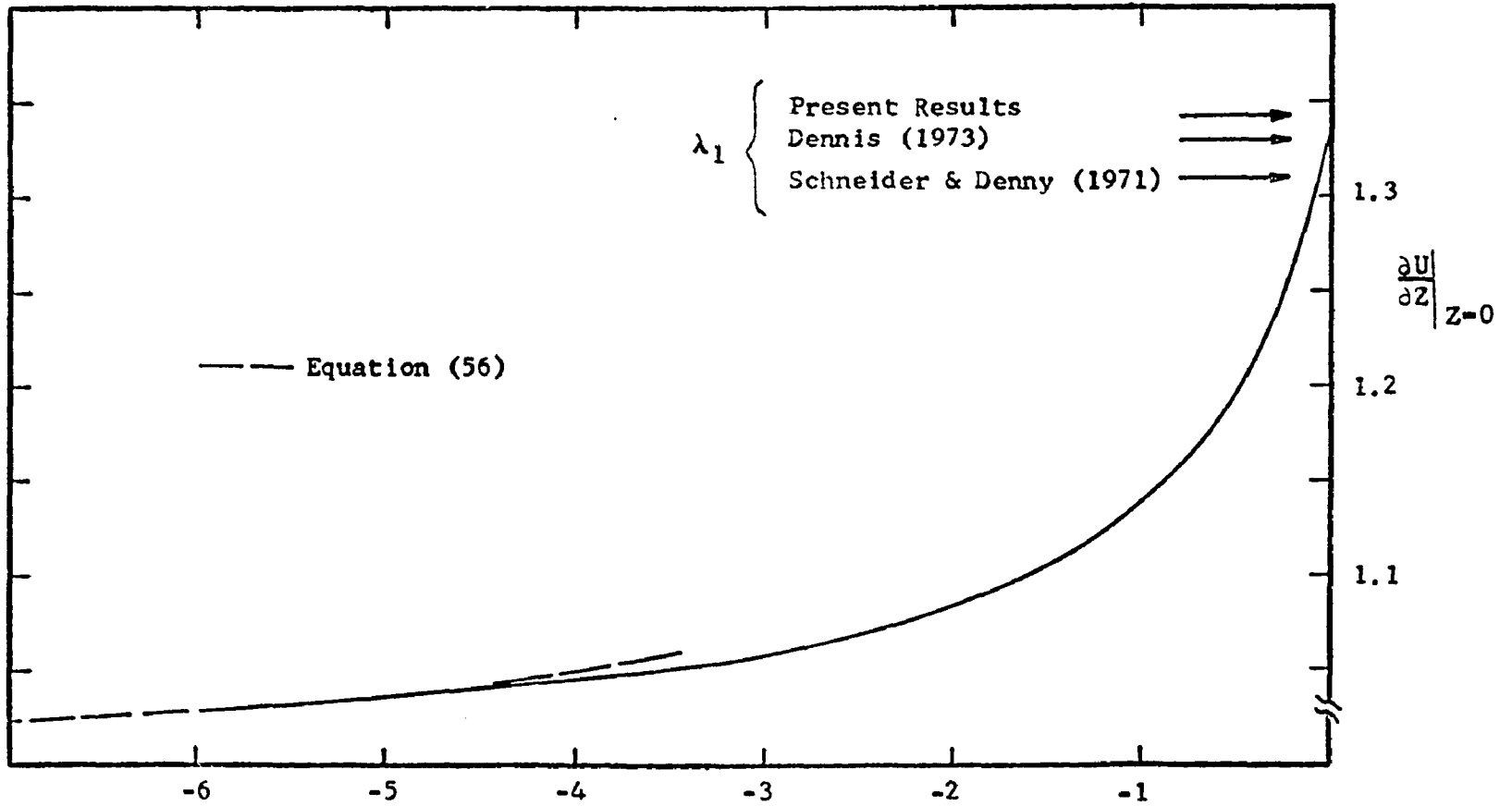


Fig. 4.--Skin Friction near the Trailing Edge

from the numerical integration of Equation (54) is employed to initiate the boundary-layer computations in the lower deck at  $X = -6$ . A confirmation that the computations have been initiated an adequate distance upstream from the trailing edge is provided by the skin friction results from the computations initiated at  $X = -12$ . The results from the longer interval are in agreement with the plotted results to four decimal places.

The ratio of the actual skin friction at the triple-deck trailing edge  $X = 0$  to the Blasius value is  $\lambda_1$  from Equation (66). Performing  $h^2$ -extrapolation on the data yields the result  $\lambda_1 = 1.343$ . It may be noted that the skin friction approaches its trailing-edge value smoothly from the left

$$\partial U / \partial Z \Big|_{Z=0} = 1.343 + 0.550 X, \quad X < 0.$$

For comparison, Figure 10 of Schneider and Denny (1971) shows two constant values for the skin friction in the immediate trailing-edge region, one labeled second order boundary layer, the other isobaric plate. The ratio of their second-order boundary-layer skin friction to the isobaric plate-skin friction is approximately  $2.75/2.10 = 1.31$  for their single Reynolds number of  $10^5$ . At the lower Reynolds numbers of 40, 100, and 200, Dennis (1973) has found that  $\lambda_1 = 1.33$  by fitting the skin-friction data from his numerical solutions to the Navier-Stokes equations with the  $R^{-3/8}$  scaling of the triple deck.

The multiplicative constant in the second term of the drag equation is the result of the integration of the increased skin friction in the trailing edge region shown in Figure 4. The drag on



one side of the finite flat plate is given by Equation (47) as

$$C_d = 1.328 R^{-1/2} + 2.694 R^{-7/8} + \dots \quad (89)$$

with the constant in the second term evaluated from the numerical integration of the skin friction along the plate and the contribution from the integral of the asymptotic expansion, Equation (56), valid from the numerical endpoint to minus infinity. Messiter (1970) obtained the approximate values of 1.58 from his assumed  $A(X)$  and 1.21 from his computed  $A(X)$  for this constant. His values are lower than the present result because of the smaller favorable pressure gradient acting over most of the plate in his computations.

The drag coefficients predicted using Equation (89) are compared with the data of Dennis (1973), Dennis and Chang (1969) and Dennis and Dunwoody (1966) in Table 1. The present results are about eight per cent high at  $R = 1$  ( $\epsilon = 1$ ), two per cent high at  $R = 15$  ( $\epsilon = 0.713$ ), 3.6 per cent low at  $R = 1,000$  ( $\epsilon = 0.422$ ) and nearly exact at  $R = 10,000$  ( $\epsilon = 0.316$ ) as compared with the numerical solutions of the Navier-Stokes equations. The accuracy of the two-term formula for the drag was unexpected at the lower Reynolds numbers, since the neglected third term is  $O(R^{-1})$  and the term retained is  $O(R^{-7/8})$ . It was not entirely without precedent, however. Lagerstrom and Cole (1955) found that at  $R = 2$  the skin friction predicted by boundary-layer theory plus the first correction agreed to within one per cent with the exact solution for the example of a cylinder expanding at a parabolic rate. However, the neglected third term in their expansion differs from the second term by the inverse square

root of the Reynolds number. This example prompted their comment, also reported by Van Dyke (1964), that ". . . the first correction to boundary-layer theory would predict the skin-friction (in separation-less flow) down to much lower Reynolds numbers than generally imagined, say  $R_e = 10$  or even 5." The data in Table 1 and the following data are even more surprising, since the exponents in their expansion are much further separated than the exponents of the present expansion.

TABLE 1  
DRAG COMPARISON WITH NUMERICAL DATA  
FLAT PLATE DRAG

R	$C_d$ (Equation (89))	$C_d^1$	$C_d^2$	$C_d^3$
1	4.022	3.79	3.64	3.708
2	2.408		2.20	
4	1.465		1.36	
10	0.779	0.773	0.748	0.7535
15	0.595		0.581	
20	0.493	0.504	0.483	0.4862
40	0.317	0.323	0.316	0.3144
100	0.181	0.187	0.188	0.1826
200	0.120	0.123		0.1220
500	0.0711		0.0731	
1000	0.0484		0.0502	
2000	0.0332		0.0341	
5000	0.0203		0.0206	
10000	0.0141		0.0141	

<sup>1</sup>Dennis and Chang (1969)

<sup>2</sup>Dennis and Dunwoody (1966)

<sup>3</sup>Dennis (1973)

Janour (1951), under the guidance of L. Prandtl, conducted experiments in the oil tunnel for viscous flow at the Wilhelm Institute at Göttingen in 1935 to determine the lower limit of validity

of the Blasius drag formula. The lower limit was found to be approximately  $R = 2 \times 10^4$  by extrapolation of the experimental data taken at 47 Reynolds numbers from 12 to 2335. Table 2 presents the experimental data tabulated by Janour (1951) and the drag coefficient predicted using Equation (89). The mean value of the error is 1.51 per cent, the root mean square error is 3.48 per cent and the maximum error is 7.52 per cent. For comparison, the mean value of the experimental error is given by Janour as  $\pm 3$  per cent. At  $R = 2 \times 10^4$ , the second term of Equation (89) contributes an additional 4.9 per cent to the Blasius drag, well within the limits of Janour's extrapolation. For  $R = 5 \times 10^5$ , a commonly accepted upper limit for laminar flows, the second term contributes an additional 1.5 per cent to the Blasius drag.

The tabulated results are also shown on Figure 5 where the experimental scatter is evident. The Blasius drag equation, the first term of Equation (89), considerably underpredicts the drag for the lower range of Reynolds numbers, whereas including the second term corrects the drag prediction to within 0.5 per cent of the experimental error.

The very close agreement between the present results and the previous data may be somewhat disconcerting when the next higher-order term of Equation (89) is considered. Imai (1957) has shown that this term, due to the overall displacement effect of the boundary layer on the semi-infinite plate is of  $O(R^{-1})$  and a term of this order also arises from the trailing-edge region from Equation (47). Unfortunately, the numerical and experimental data reported in Tables 1 and 2 scatter

TABLE 2  
DRAG COMPARISON WITH EXPERIMENTAL DATA

R	$C_d$ (Experimental)	$C_d$ (Equation (89))	% Error
11.93	0.668	0.6923	3.64
15.83	0.534	0.5741	7.52
15.83	0.564	0.5741	1.80
20.00	0.500	0.4928	-1.43
23.88	0.440	0.4394	-.12
28.02	0.369	0.3967	7.51
31.67	0.348	0.3669	5.46
29.7	0.375	0.3822	1.94
34.9	0.364	0.3451	-5.18
36.62	0.321	0.3348	4.31
40.08	0.300	0.3163	5.46
43.33	0.323	0.3013	-6.71
47.6	0.291	0.2842	-2.33
50.7	0.268	0.2733	1.98
53.4	0.268	0.2646	-1.24
60.3	0.243	0.2455	1.07
75.6	0.218	0.2139	-1.87
92.9	0.191	0.1888	-1.11
102.5	0.177	0.1780	.60
115.5	0.168	0.1658	-1.31
138.4	0.153	0.1489	-2.66
165.6	0.134	0.1340	.01
227.3	0.111	0.1114	.40
247.2	0.108	0.1061	-1.70
219.1	0.1073	0.1138	6.09
234.5	0.1068	0.1094	2.48
318.1	0.0912	0.0918	.73
340.	0.0872	0.0884	1.42
403.	0.0806	0.0803	-.37
432.	0.0764	0.0772	1.05
483.	0.0702	0.0725	3.28
516.	0.0678	0.0698	3.04
640.	0.0620	0.0619	-.11
993.	0.0460	0.0485	5.59
1050.	0.0458	0.0471	2.85
1134.	0.0438	0.0451	3.10
724.	0.0547	0.0578	5.72
785.	0.0528	0.0552	4.72
808.	0.0520	0.0544	4.65
1143.	0.0450	0.0449	-.08
1336.	0.0417	0.0412	-.98
1542.	0.0391	0.0382	-2.32
1680.	0.0345	0.0364	5.67
1921.	0.0326	0.0339	4.01
2133.	0.0313	0.0320	2.39
2262.	0.0305	0.0310	1.80
2335.	0.0304	0.0305	.41

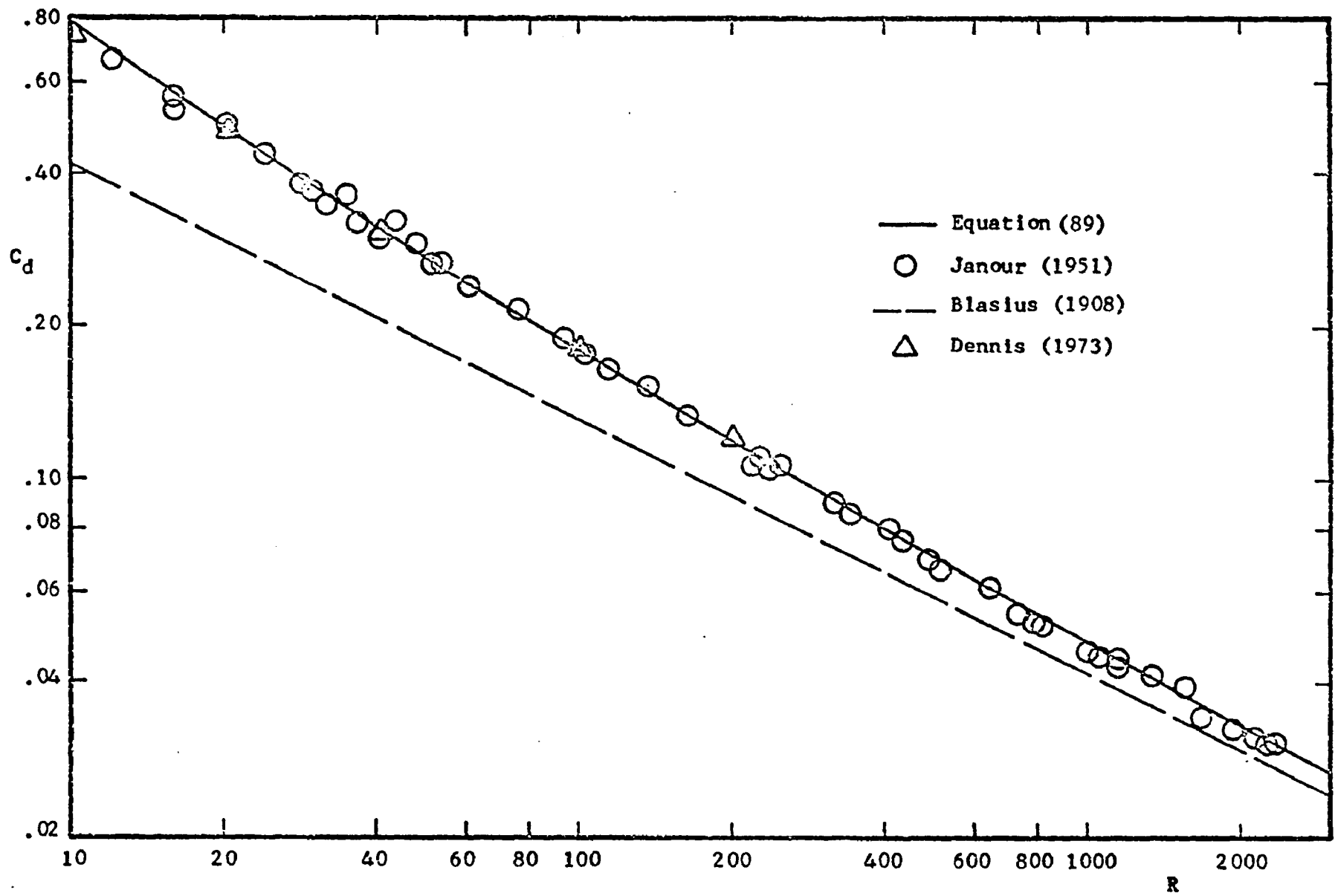


Fig. 5.--Drag versus Reynolds Number - A Comparison of Theory and Experiment

about the present results and trends with  $R^{-1}$  cannot be discerned. A plausible explanation appears to be that the term of  $O(R^{-1})$  and other higher fractional-order terms resulting from the trailing-edge region tend to cancel the  $O(R^{-1})$  term of Imai (1957).

The increase in skin friction is caused by the favorable pressure gradient induced on the plate by the wake. The pressure distribution on the plate and downstream in the wake is shown on Figures 6 and 7. The pressure  $P(X)$  of Figure 6 is related to the physical pressure  $p^*$  by

$$P(X) = \lambda^{1/2} \epsilon^2 (p^* - p_\infty) / \rho U_\infty^2 \quad (90)$$

and the streamwise coordinate  $X$  is related to the physical coordinate  $x^*$  by

$$X = \lambda^{5/4} \epsilon^3 x^*/L \quad (91)$$

as in Chapter II. Messiter (1970) also employed the above scaling and his approximate results are shown on Figure 6 for comparison. Upstream near  $X = -3$  Messiter's results are in agreement with the present results. In the range  $-3 < X < .75$  Messiter's pressure gradient is apparently less favorable than the present results, thus accounting for the smaller multiplicative constant he obtained for the second term of the drag equation. The minimum value of the pressure is reached at  $X = 0$  in both analyses and Messiter (1970) found  $P_0 \approx -0.36$  while here  $P_0 = -0.388$ . Downstream in the wake Messiter's pressure apparently reaches a maximum of  $P(X) \approx 0.06$  at

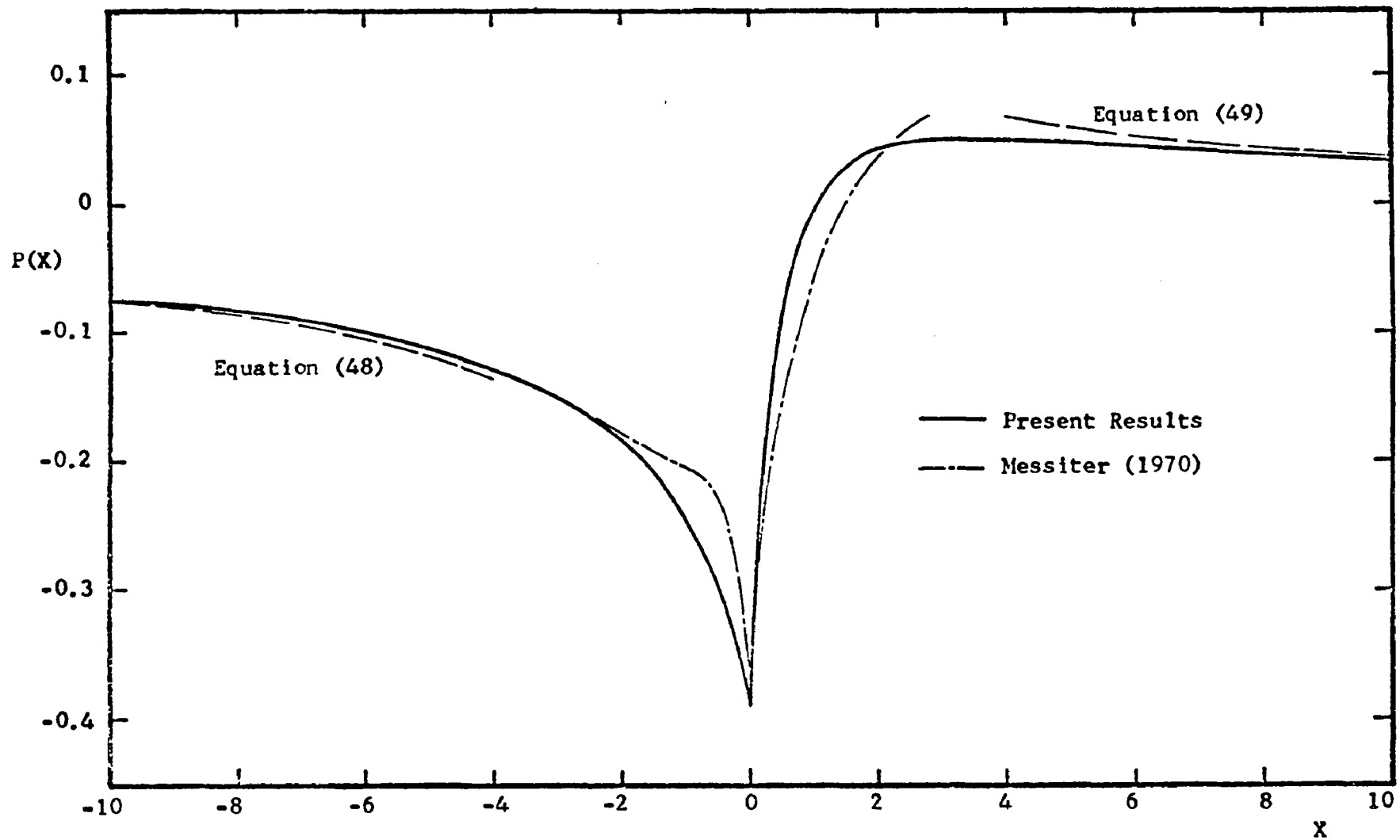


Fig. 6.--Induced Pressure Distribution

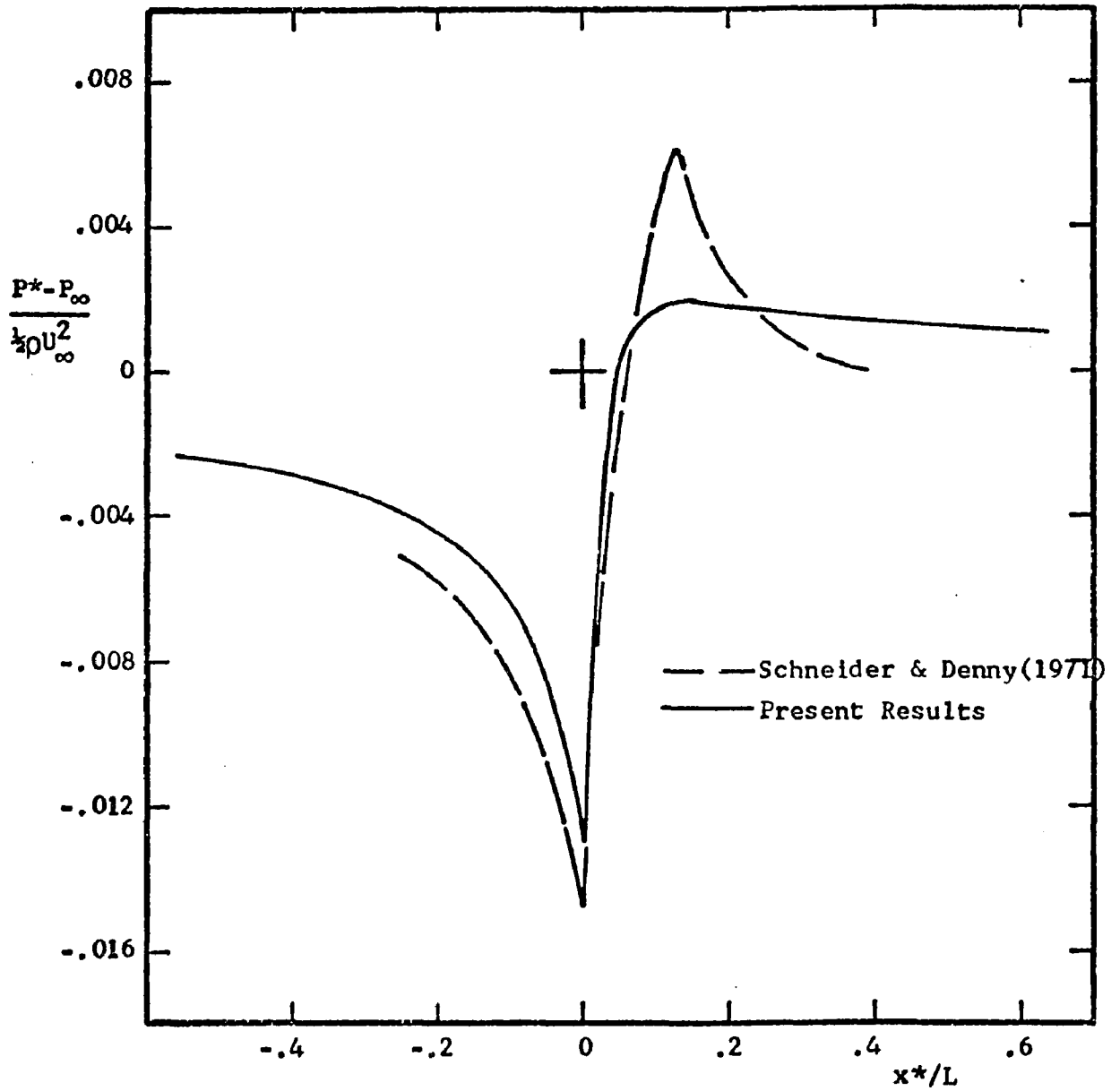


Fig. 7.-- A Comparison of the Induced Pressure Distribution with the Results of Schneider & Denny at  $R = 10^5$



$X \approx 2.75$ . The pressure computed here reaches a maximum of  $P(X) = 0.049$  at  $X = 3.05$  and diminishes to the asymptotic behavior predicted by Equation (64) with  $b_1 = -0.275$ . The constant  $b_1$  also occurs in the expansions of the pressure upstream and the centerline velocity and displacement function downstream as indicated in Equations (65), (63), and (62), respectively. The constant  $b_1$  was determined by fitting the numerical data from these three independent sources to serve as a check on the accuracy of the results. The discussion of  $b_1$  will be deferred until the relevant results are presented.

Schneider and Denny (1971), who did not employ the Reynolds number scaling of Stewartson (1969) and Messiter (1970), obtained results for the specific Reynolds number  $R = 10^5$ . Their pressure results are shown in Figure 7. Along the plate and in the immediate wake their pressure gradient and the present results appear in agreement although their pressure level is lower. The similar pressure gradients on the plate produce similar increases in the skin friction as evidenced by the close agreement of  $\lambda_1$  and their second-order boundary-layer results. In the wake the pressure results of Schneider and Denny (1971) reach a relatively high peak before rapidly diminishing to the freestream value while the present results smoothly approach the asymptotic freestream value.

The pressure distribution is generated by the displacement function of the lower deck, shown with Messiter's approximate solutions on Figure 8. Messiter (1970) assumed the form for  $A'(X)$  given by Equation (76) with  $C_0 = 0$ , performed the Hilbert integral analytically, then employed an integral sublayer method to arrive at a

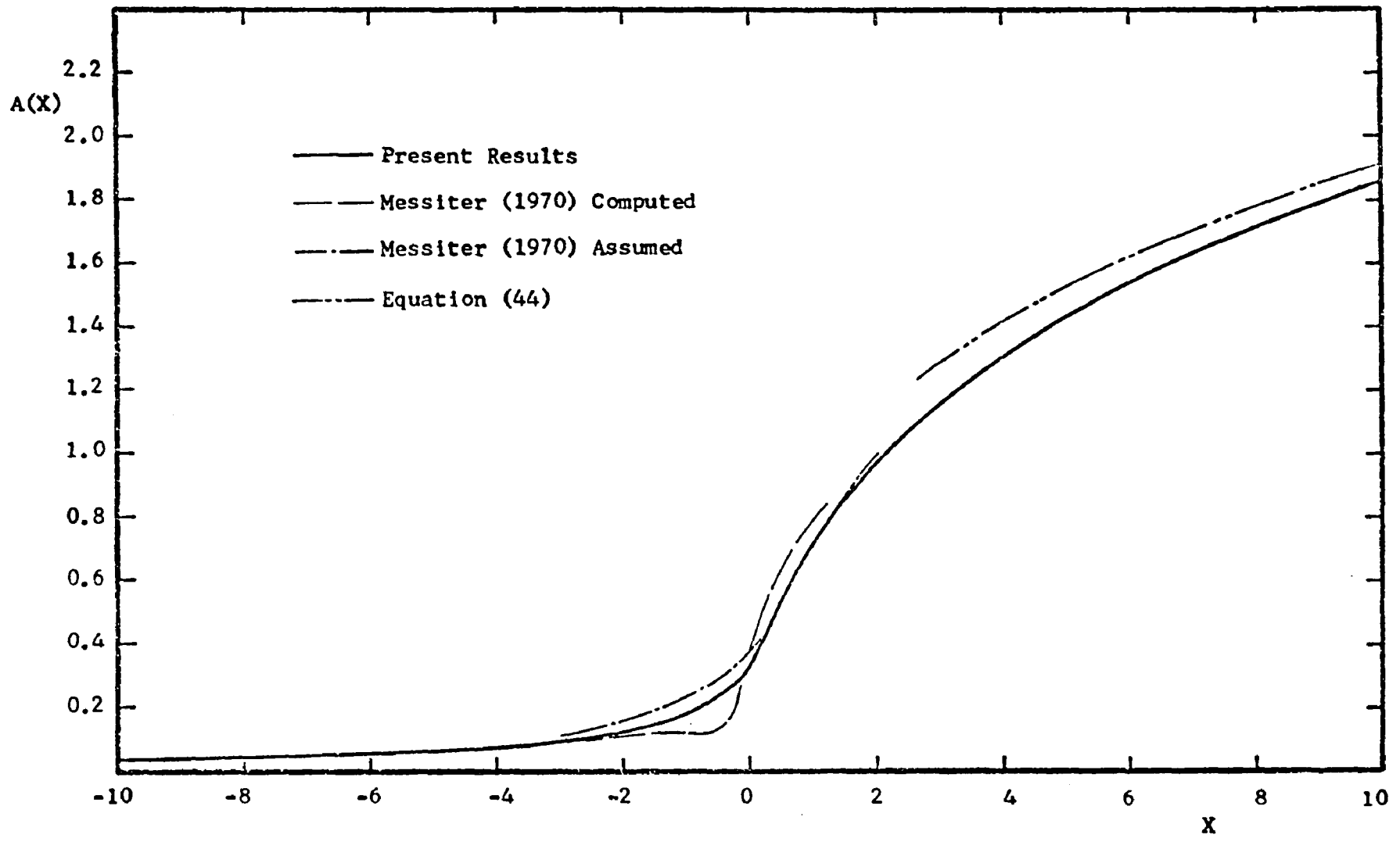


Fig. 8.--Lower Deck Displacement Function,  $A(X)$

computed  $A(X)$  which was compared with the assumed  $A(X)$  to ascertain the adjustments required in the  $C_i$ . The method is similar to the procedure employed here to improve the input data. Messiter was able to obtain a computed  $A(X)$  that is in qualitative agreement with the assumed  $A(X)$ . Both functions are displayed on Figure 8 along with the present results which lie between Messiter's results on the plate and approximately follow his assumed  $A(X)$  in the wake. Asymptotically the present results satisfy the expansion of Equation (62) for  $X \rightarrow \infty$  if  $b_1 = -0.275$ .

From Equations (18) and (24),  $A(X)$  multiplies the first-order perturbation to the streamwise velocity in the main deck

$$u = U_0(y) + \epsilon \lambda^{-3/4} A(\lambda^{-5/4} X) dU_0/dy + \dots \quad (92)$$

Considering Equation (92) as a Taylor series in  $U_0$ , it is evident that  $A(X)$  represents a shift in  $y$  or displacement of the streamlines throughout the main deck.

In the upper deck, the pressure is related to the slope of the displacement function  $A'(X)$ , shown on Figure 9 by linear airfoil theory, i.e., the Hilbert integral, Equation (43). Physically,  $A'(X)$  is the negative of the velocity normal to the plate at the lower edge of the upper deck and is of  $O(\epsilon^2)$  from Equations (27) and (28). As shown on Figure 9, the vertical velocity is not discontinuous at the trailing edge as in the joining of the Blasius (1908) and Goldstein (1930) solutions. The triple-deck analysis has smoothed out the discontinuity in the normal velocity, which was its purpose. The maximum normal velocity occurs immediately aft of the trailing edge and strong gradients exist in this region.

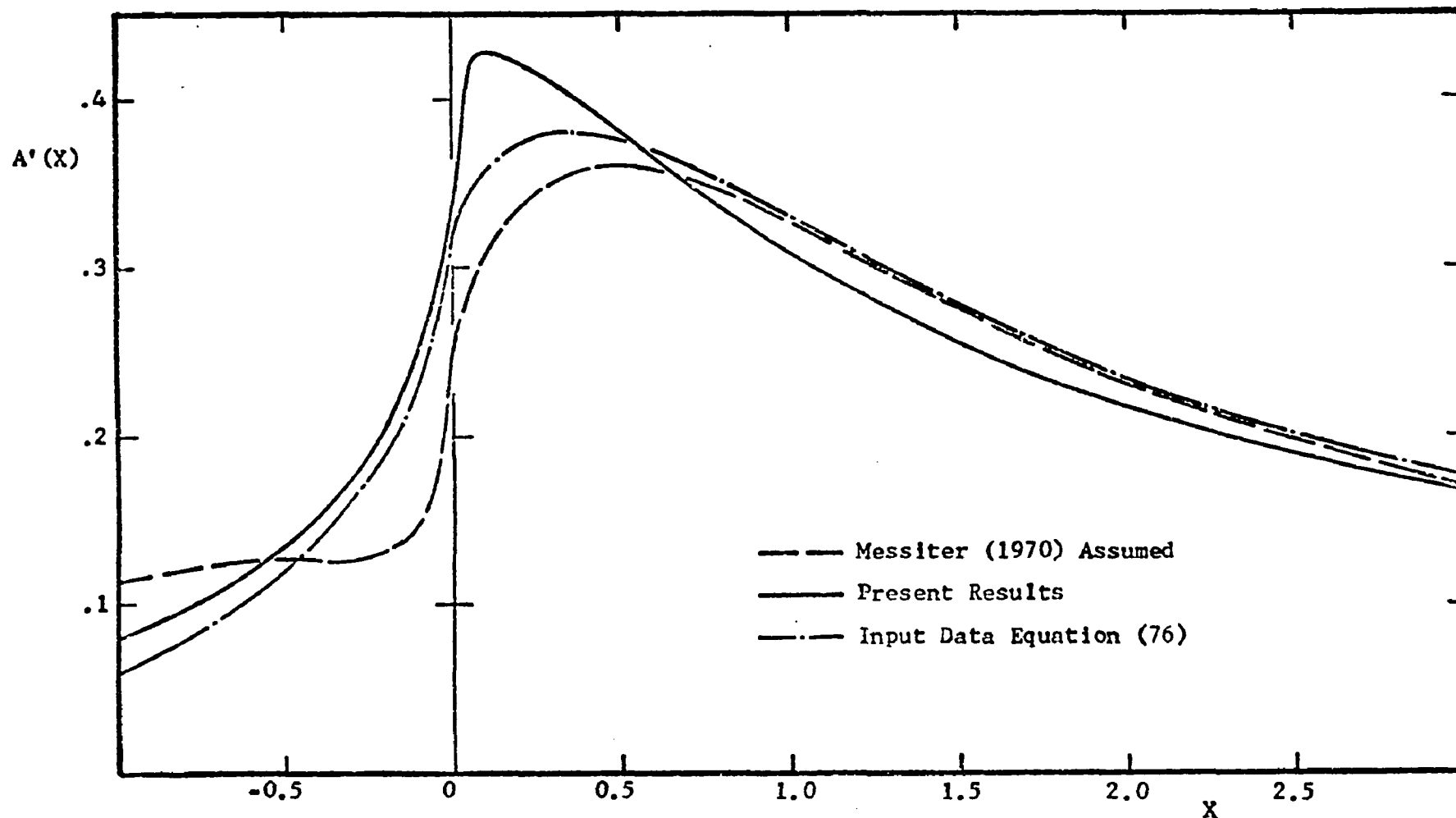


Fig. 9.--Slope of the Displacement Function,  $A'(X)$

The assumed  $A'(X)$  of Messiter (1970) and the revised  $A'(X)$  for the present input data do not approximate the solution well near the maximum. The revised  $A'(X)$  is closer to the solution upstream of the trailing edge, thus accounting for the increased computational time required to achieve convergence when Messiter's form of  $A'(X)$  was employed as initial data. The improvement in  $A'(X)$  is primarily due to the change in the constant  $C_4$  of Equation (76) which was diminished from Messiter's value of 3.0 to 1.5.

At this point it is relevant to reconsider the skew-reciprocal Hilbert integral subroutines and perform an error check. The subroutine that computes  $A'(X)$  from  $P(X)$  is required by the numerical procedure to produce the results just discussed. The subroutine that computes  $P(X)$  from  $A'(X)$  is not required in the main loops and therefore may be employed as a check on the skew-reciprocal nature of the preceding pressure and displacement thickness results. The  $A'(X)$  of Figure 9 was input to this subroutine and the resulting  $P(X)$  was compared with the  $P(X)$  of Figure 6. The error, based on the pressure at the trailing edge, is about one per cent over most of the numerical range as shown on Figure 10. For the short range calculations  $-6 \leq X \leq 6$ , the error reaches a maximum of 4.5 per cent at the downstream extreme of the range,  $X = 6$ . Thus, the preceding  $P(X)$  and  $A'(X)$  are properly skew-reciprocal within the error shown on Figure 10. The extended curves of Figure 10 pertain to the computations originating at  $X = -12$ . The error is diminished to about 0.5 per cent using the extended interval and again reaches a maximum of five per cent at the downstream extreme,  $X = +12$ . The decreasing error with increasing

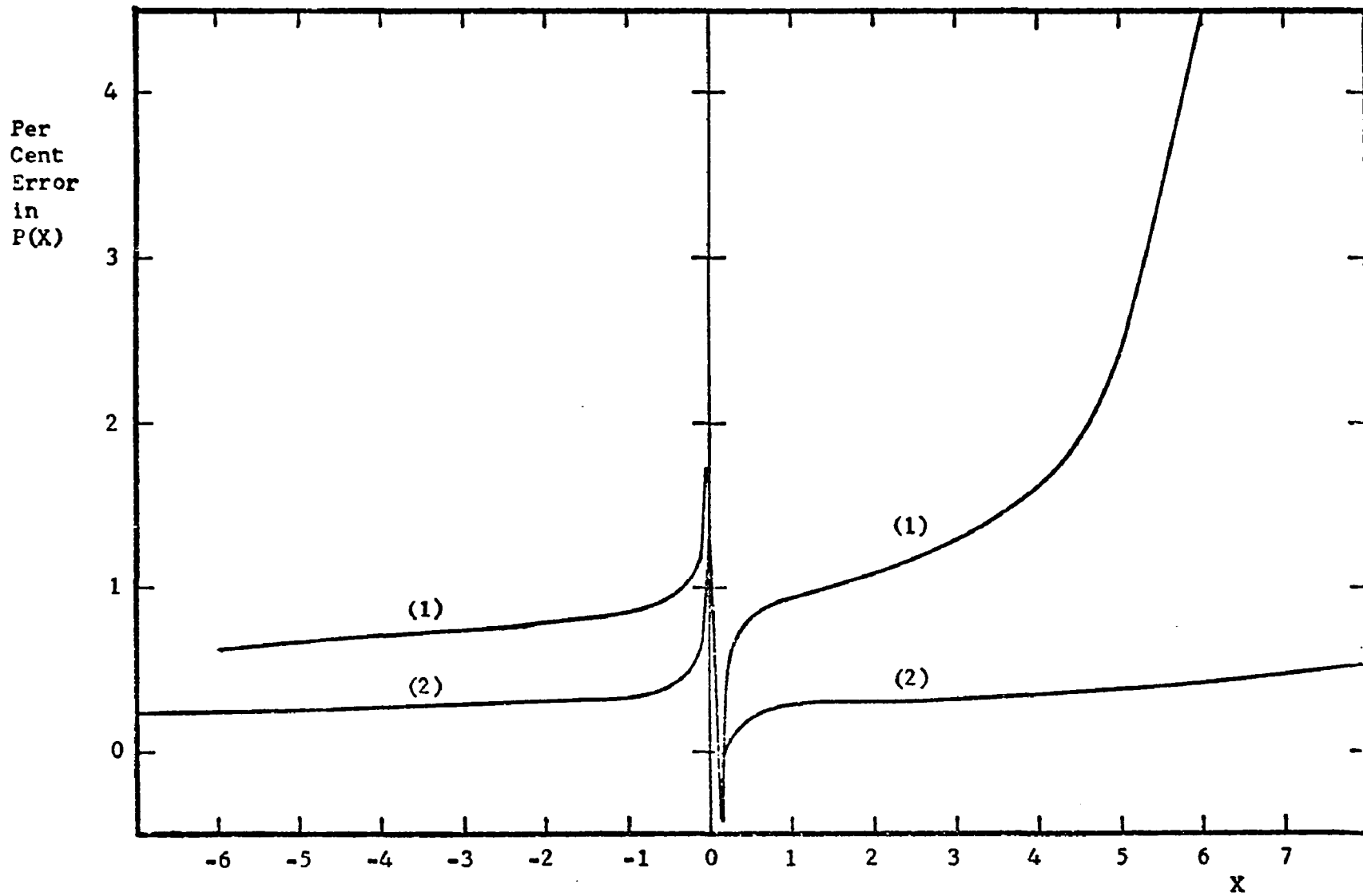


Fig. 10.--Pressure-Displacement Function Error Analysis;  
 (1)  $-6 \leq X \leq 6$ ; (2)  $-12 \leq X \leq 12$ .

interval length is in agreement with the Hilbert transformation error analysis, Appendix A. The skin friction data resulting from the two computations agrees to about  $10^{-4}$  indicating that errors of the magnitude shown on Figure 10 in the pressure and displacement thickness have little effect on the solution.

Another quantity of interest, which is also required for the computation of the constant  $b_1$  is the wake centerline velocity shown on Figure 11. Physical coordinates at  $R = 10^5$  have been employed to permit comparison with the data of Schneider and Denny (1971). The present results agree with the results of Schneider and Denny over the downstream range  $0.001 < x^*/L < 0.05$ . Far downstream the present results correctly approach the one-term Goldstein (1930) results. The results of Schneider and Denny (1971) apparently lie between the one-term Goldstein and the full Goldstein results at  $x^*/L = 1$  corresponding to their second-order boundary-layer calculations which employ the true edge velocity as the boundary condition, rather than matching to the main deck as in Stewartson's theory.

The desirability of using a smaller streamwise step size is evident when the small  $x^*/L$  range is viewed. Computational time limitations on the present numerical procedure prohibit the use of a  $\Delta X$  small enough to determine precisely how the present results approach the Navier-Stokes region computed by Schneider and Denny. Both sets of data approach the small  $x^*/L$  behavior of the centerline velocity predicted by Equation (73) but the results of Schneider and Denny deviate for  $x^*/L < 3 \times 10^{-4}$ .

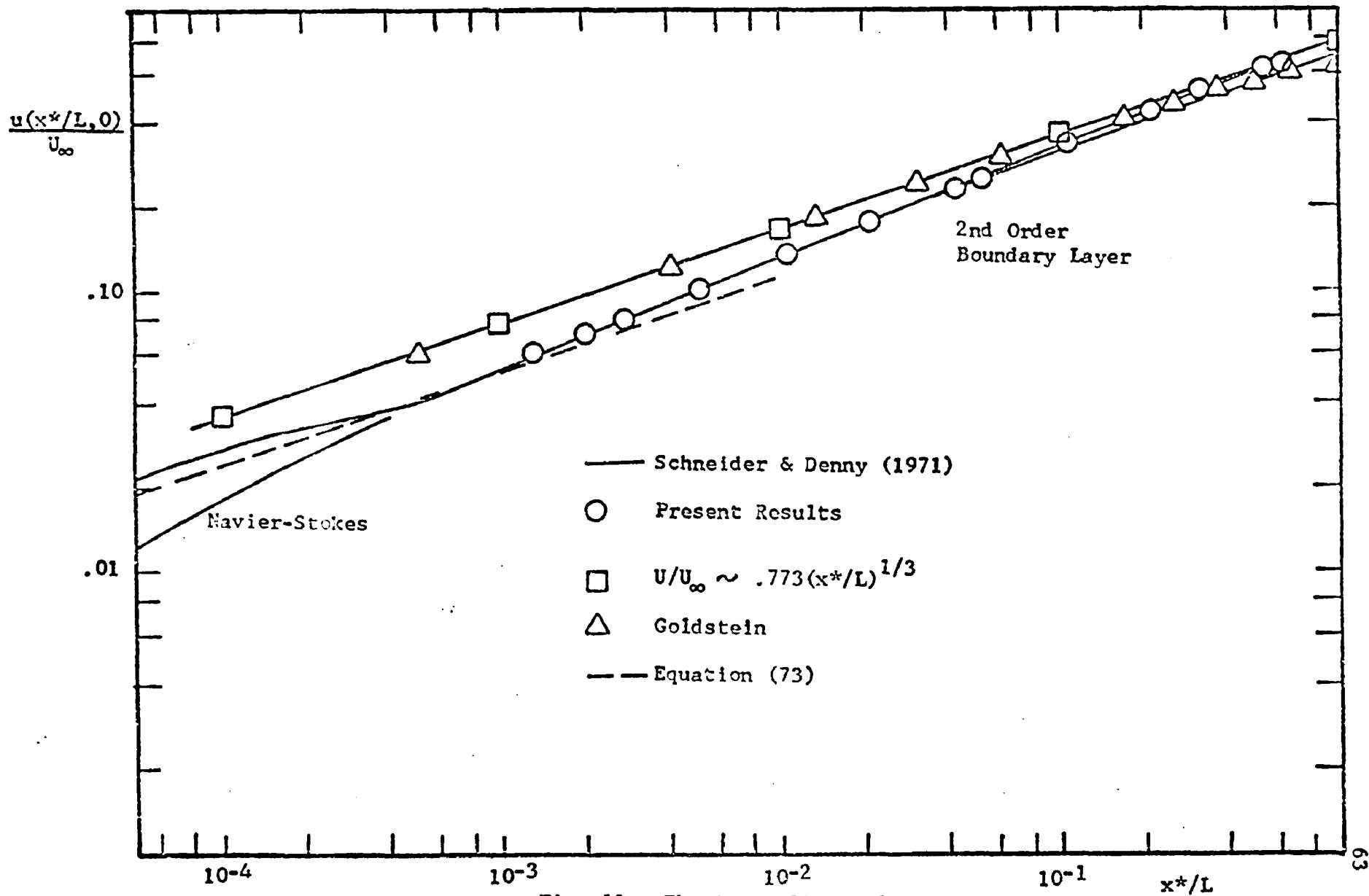


Fig. 11.--The Centerline Velocity



Expanding the previous streamwise scales and returning to the triple-deck coordinates to permit visualization of the region near  $X = 0$  (Figures 12 and 13) we see that the present results approach the behavior predicted by Equation (73) as the step size is halved. The sensitivity of the results to the step size on this scale is not surprising since Plotkin and Flugge-Lotz (1968) encountered the same phenomena in their computations to obtain an improved first approximation to the solution in the trailing edge region at high Reynolds numbers. It should also be noted that the second-order terms of the expansions Equations (73) and (75) are very nearly equal to the first-order terms and could easily account for the small disagreement evident in Figures 12 and 13.

The pressure results, Figure 13, exhibit the same trends as the centerline velocity as  $X \rightarrow 0$ . Upstream the pressure results are less sensitive to step size than downstream because the boundary layer has not been directly notified that the skin friction has vanished. Alternatively, the pressure is more singular as  $X \rightarrow 0$  from the wake side than as  $X \rightarrow 0$  from the plate side of the trailing edge. The pressure at the trailing edge  $P_0$  has been evaluated from the limit as  $X \rightarrow 0$  from the left for this reason.

We have now discussed the numerical data for the three functions  $A(X)$ ,  $P(X)$  and  $U(X,0)$ , together with the predicted asymptotic behavior near  $X = 0$ . The asymptotic expansions for large  $X$  of these three functions each contain the arbitrary constant  $b_1$  which must be determined from the numerical procedure. The satisfaction of the asymptotic boundary conditions is of major importance in assessing the

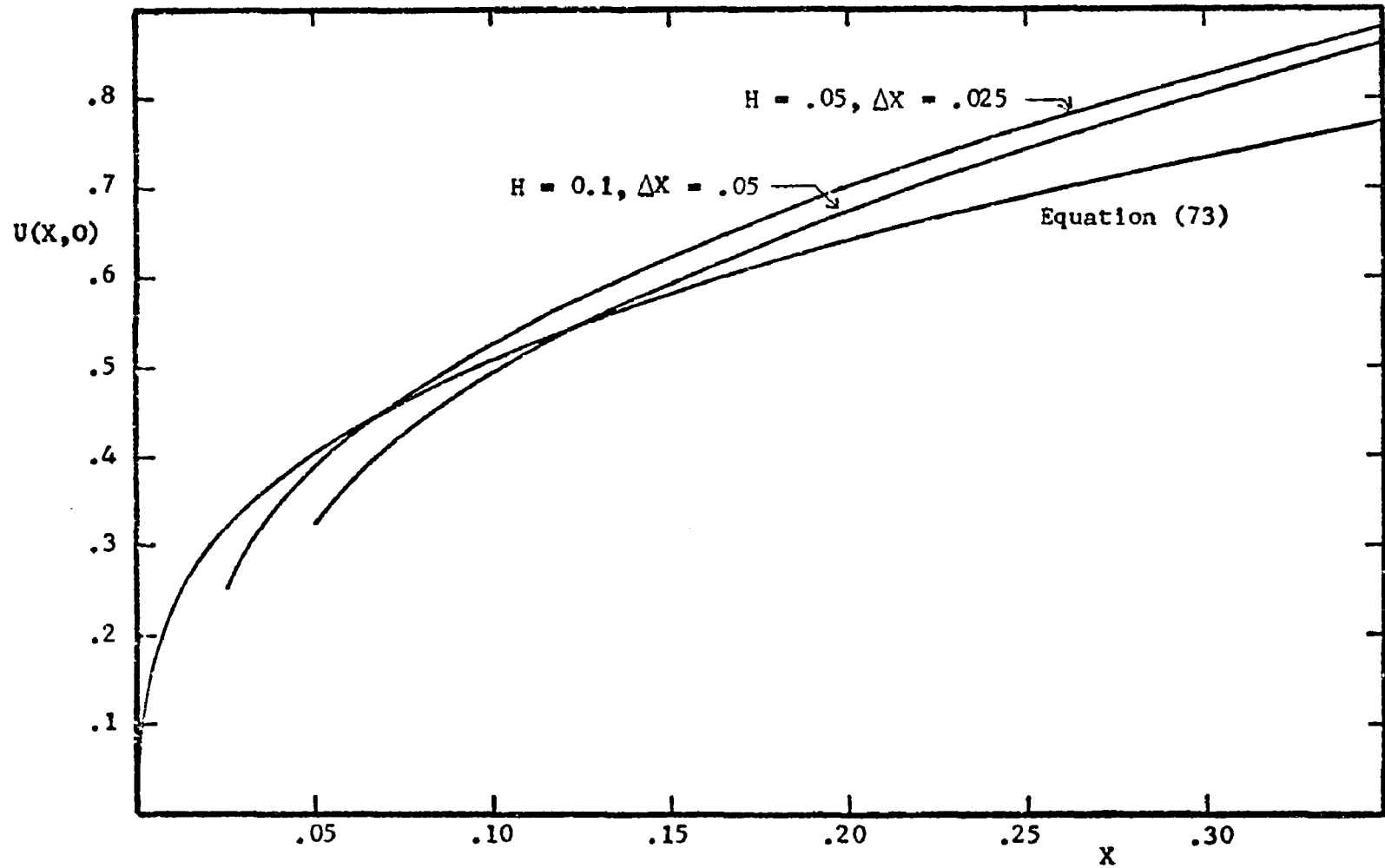


Fig. 12.--The Centerline Velocity near  $X = 0$

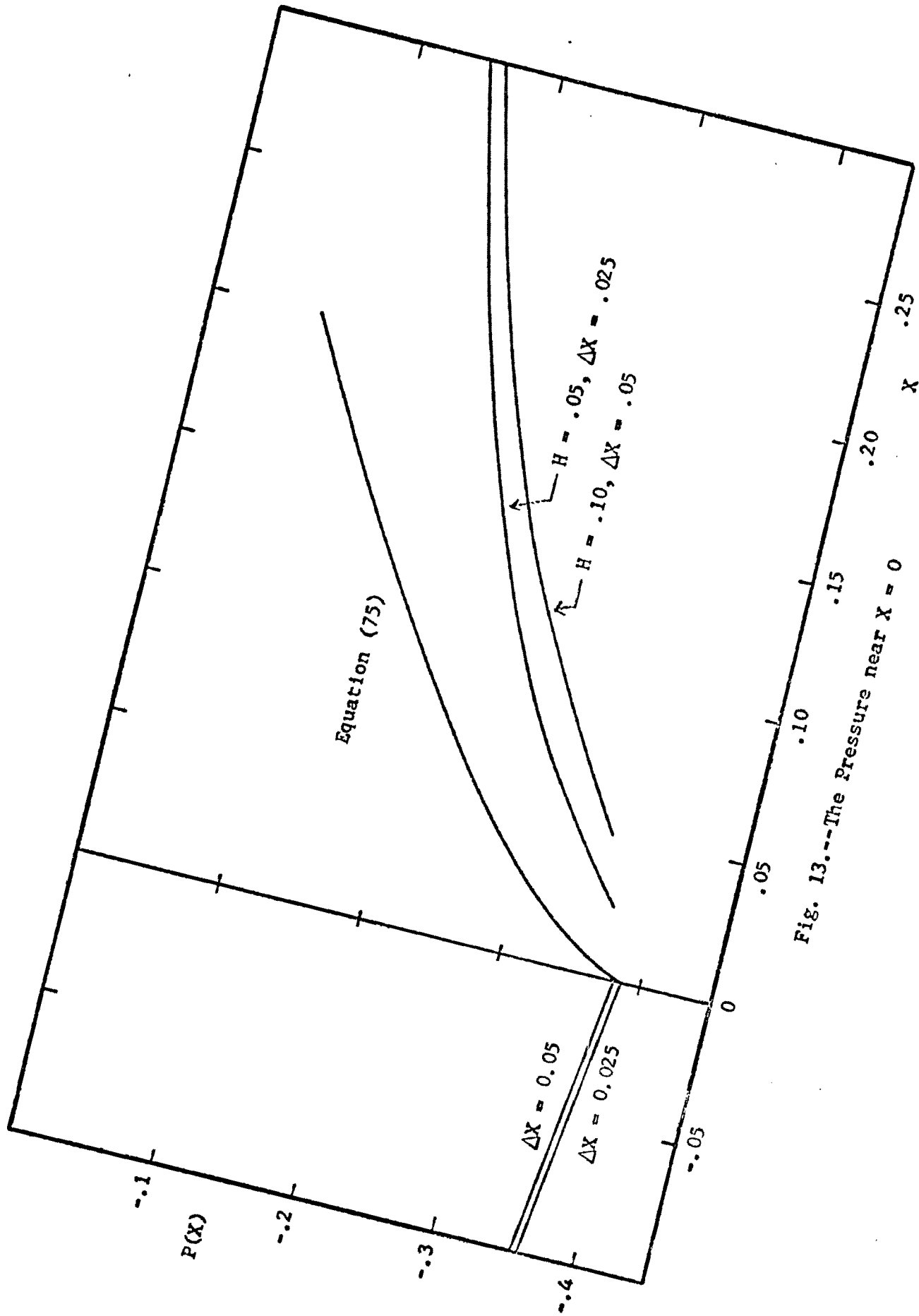


Fig. 13.--The Pressure near  $x = 0$

accuracy of the numerical procedure. The present results all approach the predicted asymptotic behavior for  $|X| \rightarrow \infty$ ; however, the second-order terms serve as a more stringent test of the accuracy of the numerical procedure. Here the asymptotic expansions were numerically fitted to the previous numerical data to simultaneously determine the second-order constant  $b_1$  and provide a measure of the numerical matching of the data and the expansions.

With the obvious change in notation, each of the expansions Equations (62), (63), (64), and (65) were rearranged to determine the constant  $b_1$  appearing in the second-order term, i.e.,

$$b_p = [3^{1/2} |X|^{2/3} (P^+ - P^-)/(0.892) - 1] |X| / 2 \quad (93)$$

$$b_A = [A(X) + 0.070X^{-1} - 0.892X^{1/3}] X^{2/3}/0.892 \quad (94)$$

$$b_U = [U(X,0) - 0.052X^{-1} - 1.611X^{1/3}] X^{2/3}/1.611 . \quad (95)$$

The difference of Equations (64) and (65) was formed to eliminate the higher-order constant  $d_1$  from the pressure expansions. By substitution of the values of  $P(X)$ ,  $A(X)$  and  $U(X,0)$  obtained from the numerical procedure the values of  $b_1$  required to fit each function to second-order to the predicted asymptotic behavior are found. Ideally, the three  $b_1$  curves should approach and remain at one constant value as  $X \rightarrow \infty$ . The fact that the  $b_1$  curves of Figures 14, 15 and 16 do not is, admittedly, a shortcoming of the numerical procedure. The curves shown pertain to the preceding data. The numerical study which led to the selection of the preceding values for the parameters of the

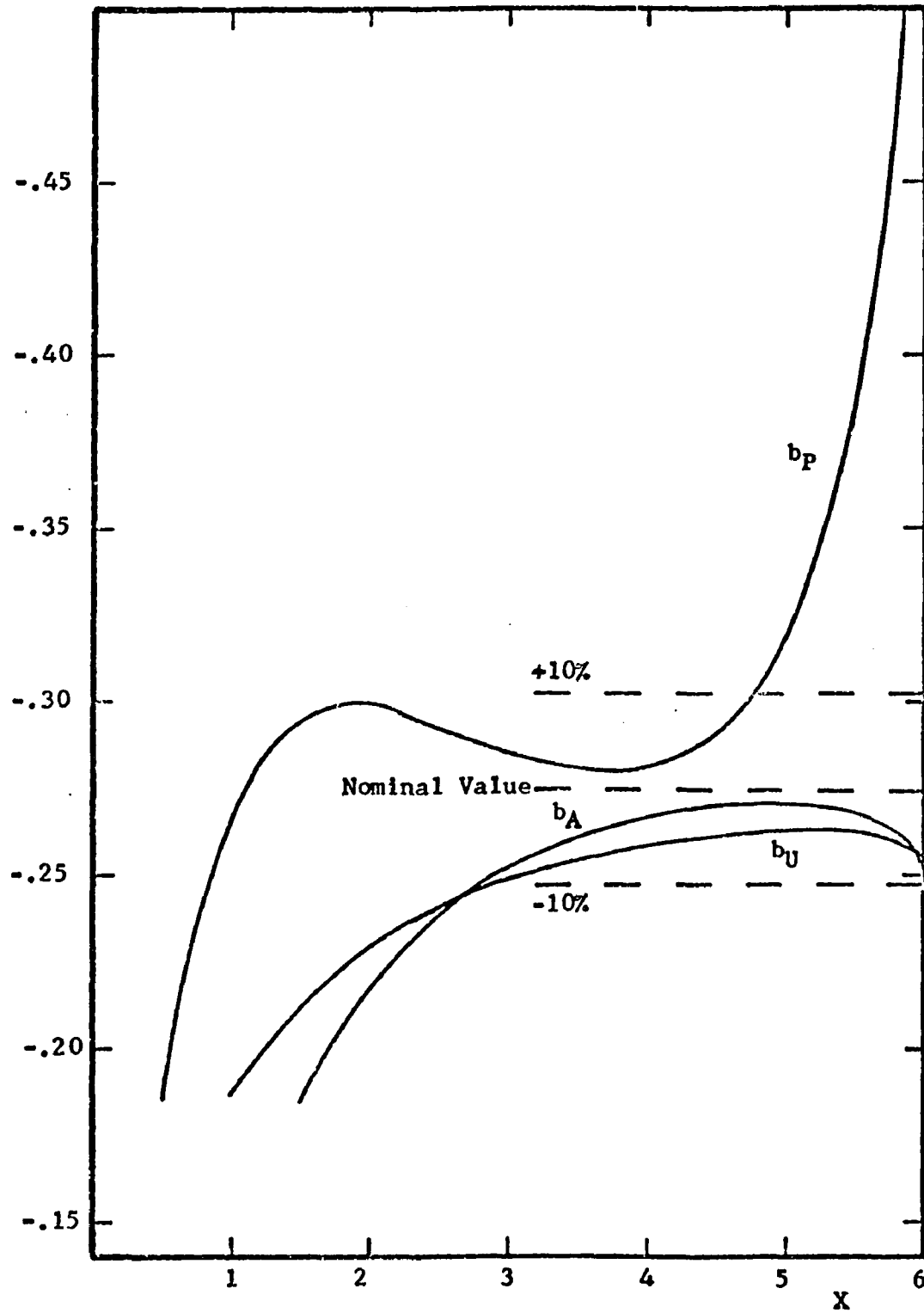


Fig. 14.--The Asymptotic Behavior:  $b_1$  for  $X \rightarrow 6$ ,  $\Delta X = .05$

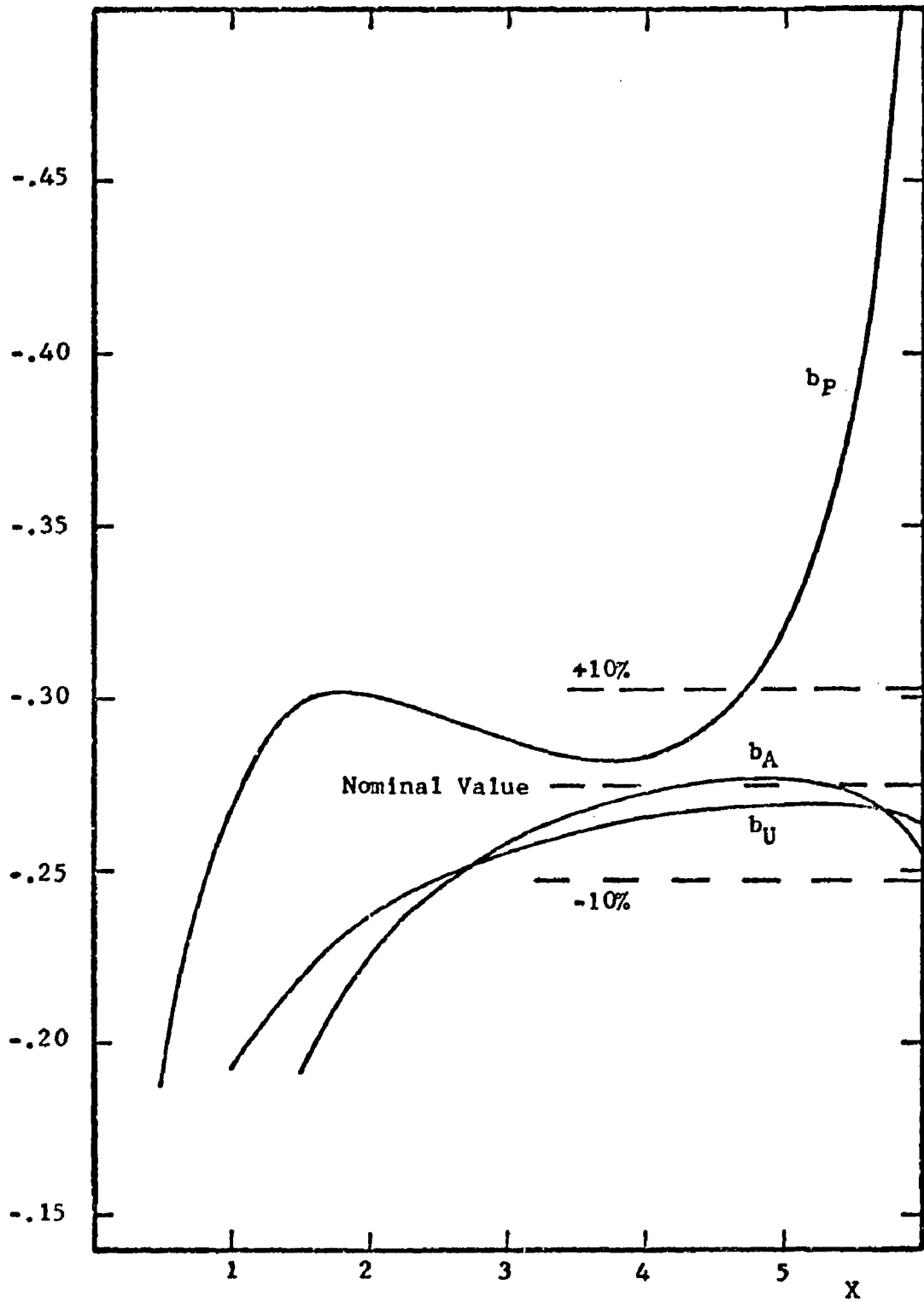


Fig. 15.--The Asymptotic Behavior:  $b_1$  for  $X \rightarrow 6$ ,  $\Delta X = .025$

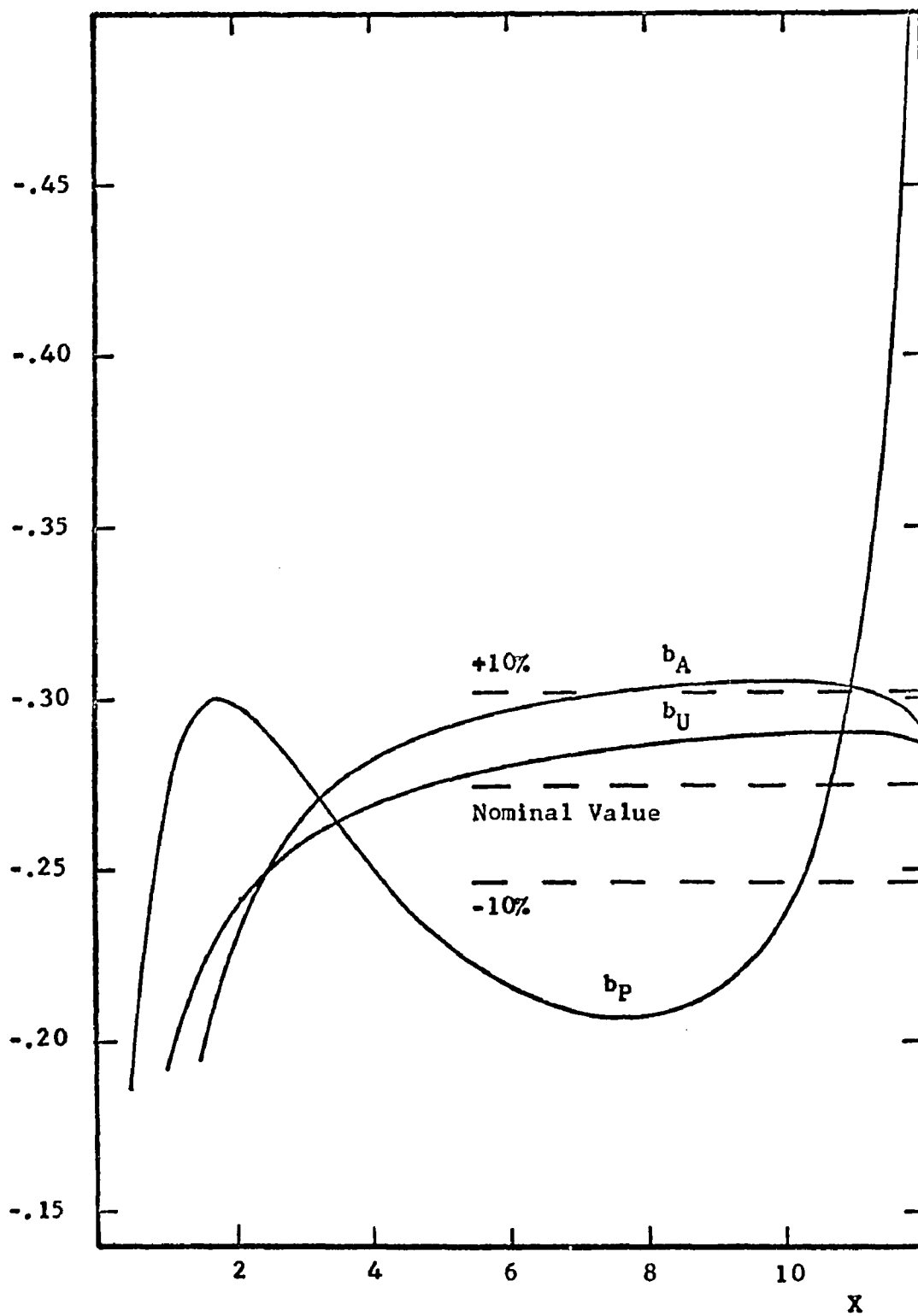


Fig. 16.--The Asymptotic Behavior:  $b_1$  for  $X \rightarrow 12$ ,  $\Delta X = .05$

interval is contained in Appendix B. Figure 14 pertains to the data obtained with  $0 \leq Z \leq 9$ ,  $H = 0.1$  and  $-6 \leq X \leq 6$ ,  $\Delta X = 0.05$ . Figure 15 pertains to the same interval with  $H = 0.05$  and  $\Delta X = 0.025$  while Figure 16 pertains to the extended interval  $-12 \leq X \leq 12$  with  $\Delta X = 0.05$  and  $H = 0.1$ , as employed for Figure 14.

A nominal asymptotic value of  $-0.275$  has been selected for  $b_1$  from the three sets of data. To set the frame of reference, the  $\pm 10$  per cent error bounds on  $b_1$  amount to a one per cent error in  $P(X)$  and a 0.5 per cent error in  $A(X)$  and  $U(X,0)$  at  $X = 6$  from Equations (62), (63), (64), and (65). In fact, an error of 100 per cent in  $b_1$  only amounts to a nine per cent error in  $P(X)$  at  $X = 6$ .

It should be noted that the respective  $b_A$ ,  $b_U$  and  $b_P$  curves are in agreement between three different sets of data within the range  $X < 2$ . This is definite indication that the small changes in the large  $X$  behavior of  $A(X)$ ,  $P(X)$  and  $U(X,0)$  encountered here do not appreciably effect the solution nearer the trailing edge.

The  $b_A$  and  $b_U$  curves are within the 10 per cent error band of the nominal  $b_1$  as  $X$  becomes large in all three cases indicating that  $A(X)$  and  $U(X,0)$  agree with the predicted asymptotic behavior to within 0.5 per cent.

The pressure results are indeed the least accurate. The  $b_P$  curve may even appear divergent as  $X \rightarrow 6$  on this scale. The curve is not divergent since the  $b_P$  of Figure 16 is smooth in the range  $+6 < X < 10$ , the steep increase in  $b_P$  occurring at  $X = 12$ . This steep increase in  $b_P$ , which approaches nine per cent error in  $P(X)$ , is attributed to several numerical problems. The computation of  $b_P$



becomes less accurate as  $|X| \rightarrow \infty$  because  $P(X)$  is approaching zero at both ends of the range and the difference must be employed to compute  $b_p$  from Equation (93). The  $b_A$  and  $b_U$  computations do not encounter the small differences incurred in the computation of  $b_p$ . For example, at  $X = 6$ ,  $A(X) \approx 1.6$ ,  $U(X,0) \approx 3$  while  $P(X) \approx 0.05$ . The second numerical problem is the Hilbert integral which is dependent on the functions  $A'(X)$  and  $P(X)$  over the entire interval. As  $|X| \rightarrow \infty$  both  $A'(X)$  and  $P(X) \rightarrow 0$  and the integral is the sum of hundreds of larger values which must cancel. This is the classical nemesis of numerical analysts. The slope and magnitude of the error is in agreement with the results of inverting the solution using the Hilbert transformation, Figure 10. The error does not significantly affect the results because the error is a small percentage of a very small function value removed a sufficient distance from the trailing edge region.

The constant  $b_1$  corresponds to an origin shift in  $X$  which is evident from the binomial expansion

$$\begin{aligned} X^{1/3} &\rightarrow (X + \Delta X)^{1/3} = X^{1/3} (1 + \Delta X/3X + \dots) \\ &= X^{1/3} + X^{-2/3} \Delta X/3 + \dots \end{aligned}$$

so  $\Delta X = 3b_1$ . The origin shift is evident when the present velocity profiles are compared with the first-order Goldstein wake velocity profiles given by Equation (45) for large  $X$  as shown on Figure 17. The present velocity profiles are uniformly translated upstream since

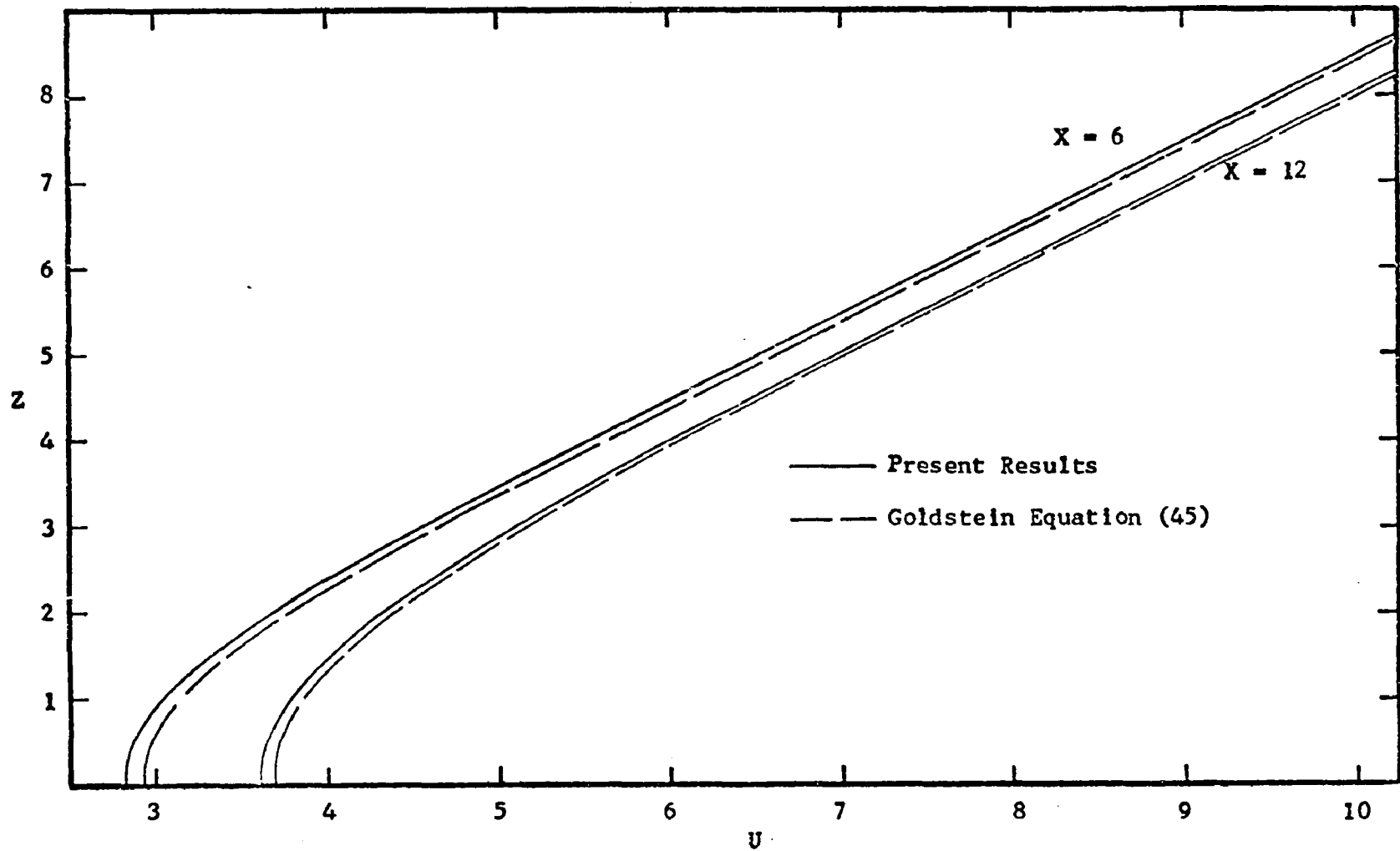


Fig. 17.-- A Comparison of the Lower Deck and the Goldstein Wake Velocity Profiles

$b_1$  is negative. As  $X$  increases the magnitude of the shift properly diminishes. The origin shift is also evident when the pressure and displacement function are compared with the one-term asymptotic expansions as shown on Figures 6 and 8.

The condition that the velocity profile of the lower deck must ultimately merge with the Goldstein wake velocity profile is attained by the numerical procedure. This condition cannot be enforced because of the parabolic nature of the boundary-layer equations and serves as another check on the results. From Equation (62)  $b_1$  is the shift in  $A(X)$  or the velocity at the outer edge of the profile and from Equation (63)  $b_1$  is the shift in  $U(X,0)$ , the velocity at the lower edge or wake centerline.

The perturbations to the linear velocity profile of the lower deck caused by the preceding pressure gradients are shown on Figures 18, 19 and 20. The velocity perturbations show that the outer edge was taken sufficiently large since  $A(X)$  attains its constant value well inside the outer edge at all streamwise locations. Upstream on the plate the perturbations are small and permit the expanded velocity scale of Figure 18 where a slight departure of the velocity profile from the vertical direction is evident at  $Z = 6$ . The velocity variation at  $Z = 6$  is greater than  $10^{-4}$ , the error tolerance on  $A(X)$ , and necessitated moving the numerical outer edge of the lower deck from  $Z = 6$  to  $Z = 9$  to determine the second-order constant,  $b_1$ .

The significance of the proper placement of the outer edge of the layer is that the outer boundary condition is enforced on the profile by the numerical method. The effects of enforcing the

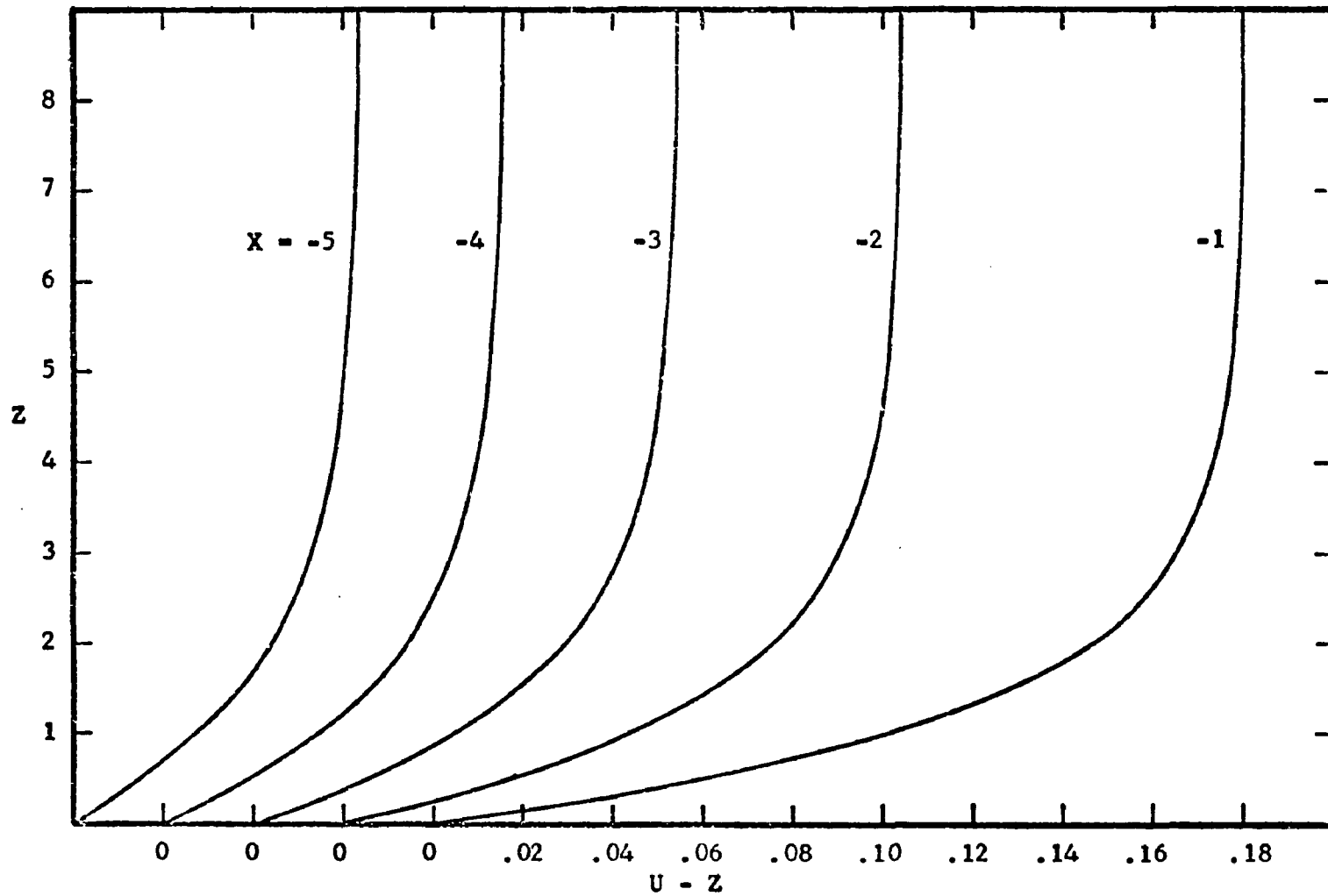


Fig. 18.--Velocity Perturbations on the Plate

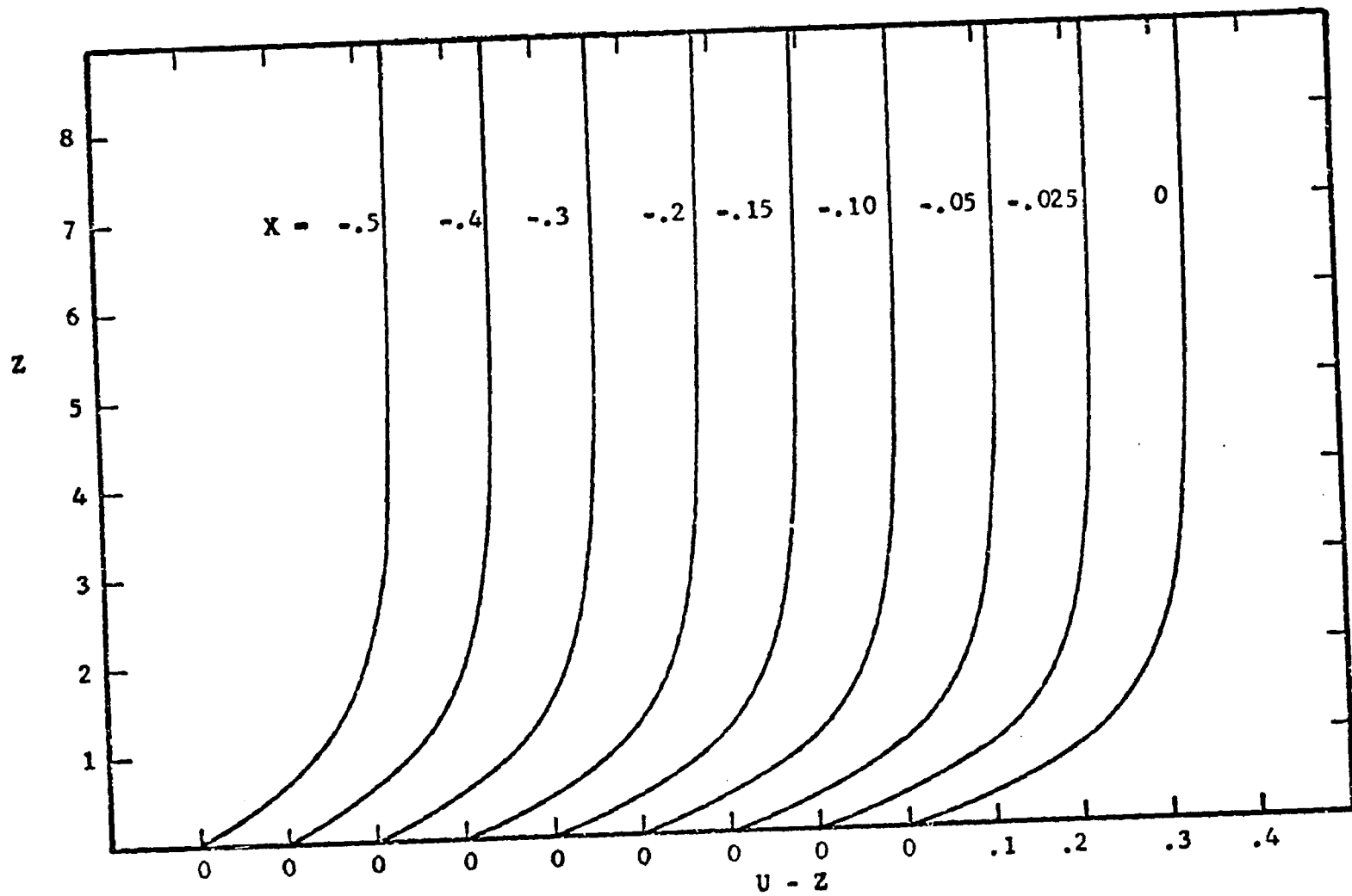


Fig. 19.--Velocity Perturbations at the Trailing Edge

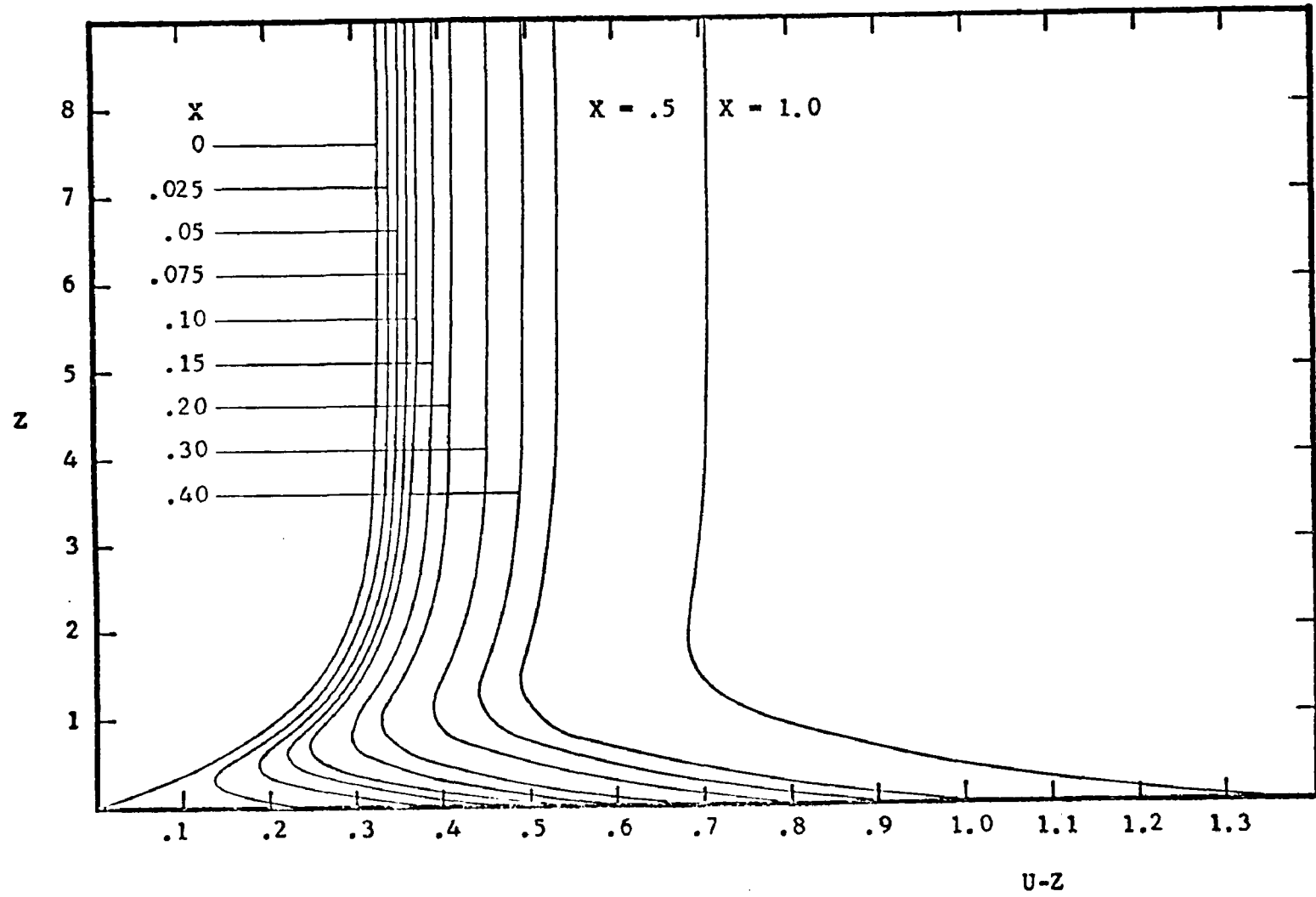


Fig. 20.--Velocity Perturbations in the Inner Wake

boundary condition propagate for some distance down the profile and into the layer. The propagation of the boundary condition into the layer requires that the numerical outer edge of the layer be placed away from the region of interest. It is shown in Appendix B that the skin friction and  $\lambda_1$  are not significantly affected by changing the depth of the layer from  $Z_e = 6$  to  $Z_e = 9$ , insuring that the outer edge boundary condition has not been enforced prematurely.

Figures 18 and 19 demonstrate that the velocity increases smoothly to the trailing edge under the influence of the favorable pressure gradient induced on the plate by the wake. Note that the velocity perturbation,  $U - Z$ , is plotted on Figures 18, 19 and 20. At the trailing edge,  $X = 0$ , the velocity profile is smooth and differentiable as assumed in the triple-deck analysis. Downstream of the trailing edge the effects of the vanished skin friction and rapidly increasing centerline velocity propagate smoothly outward into the wake velocity profiles as shown on Figure 20. The slope of the perturbation velocity profiles at  $Z = 0$  must be  $-1$  to satisfy the boundary condition along the wake centerline. Ultimately, the velocity profiles downstream, Figure 21, merge with the Goldstein wake velocity profiles to satisfy the conditions downstream, as shown on Figure 17.

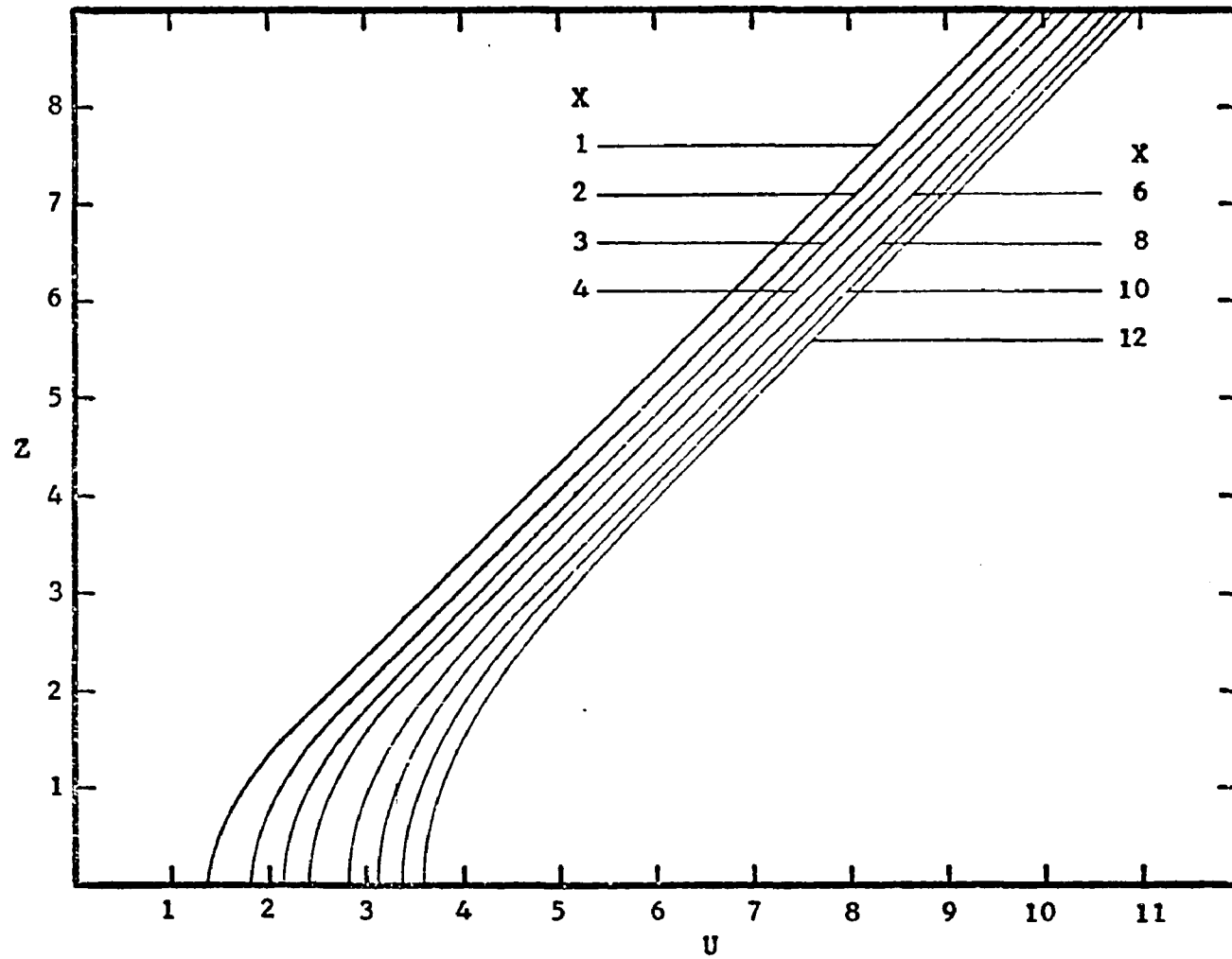


Fig 21.--Velocity Profiles in the Inner Wake



## CHAPTER V

### CONCLUSIONS

The present numerical analysis has provided additional validation for the triple-deck flow structure at the trailing edge of a flat plate and determined the constants required to complete the asymptotic expansions of Stewartson (1969). The results are self-consistent for the various grid sizes and numerical ranges employed for the computation. The present results have been demonstrated consistent with the previous numerical analyses of others and with the experimental data of Janour (1951) for the entire laminar range of Reynolds numbers.

A summary of the present numerical results is presented in Figure 22. As qualitatively predicted by Stewartson (1969) and Messiter (1970), the pressure gradient is favorable to the trailing edge, steeply adverse immediately aft of the trailing edge, and again favorable downstream of the pressure overshoot. The skin friction continuously increases from the Blasius value to  $\lambda\lambda_1$ , its value at the trailing edge. The displacement function  $A(X)$  also continuously increases from its upstream value on the plate through the trailing edge region and downstream to the Goldstein wake.

The numerical results are also tabulated in Table 3. The third decimal place is believed to be accurate.

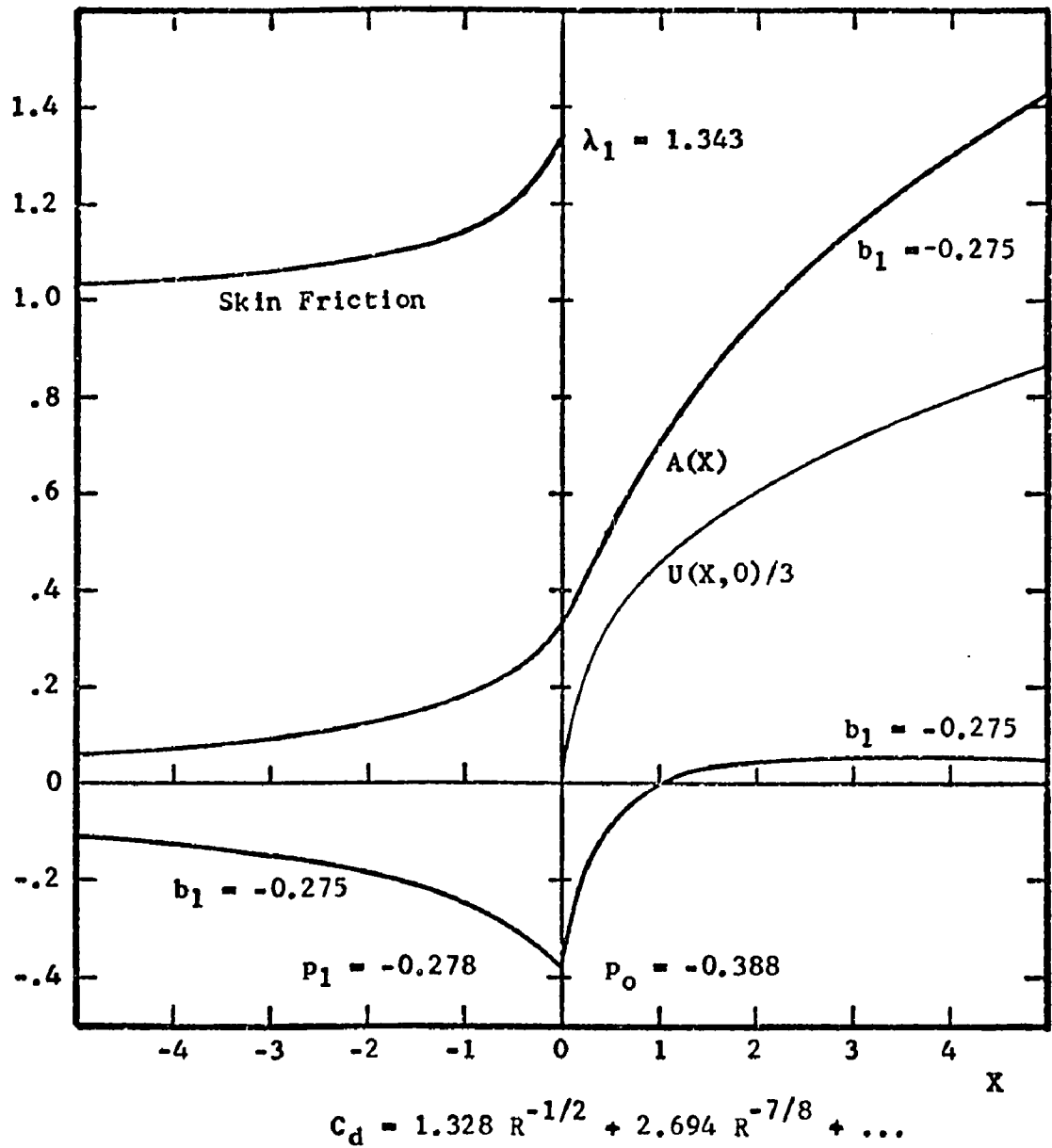


Fig. 22.--A Summary of the Numerical Results

TABLE 3  
THE NUMERICAL RESULTS

X	P(X)	A(X)	$\partial U/\partial Z _{Z=0}$	U(X, 0)
-5.0	-.113	.064	1.035	
-4.5	-.120	.069	1.039	
-4.0	-.129	.076	1.044	
-3.5	-.140	.084	1.050	
-3.0	-.152	.094	1.058	
-2.5	-.167	.107	1.069	
-2.0	-.186	.125	1.084	
-1.5	-.211	.148	1.106	
-1.0	-.245	.181	1.139	
-0.5	-.296	.233	1.198	
0.0	-.388	.335	1.343	0.
0.5	-.082	.539	0.	1.024
1.0	-.004	.710		1.367
1.5	.028	.850		1.620
2.0	.042	.967		1.825
2.5	.047	1.068		1.999
3.0	.049	1.156		2.150
3.5	.048	1.234		2.285
4.0	.047	1.305		2.407
4.5	.044	1.369		2.518
5.0	.041	1.429		2.622

The theoretical extensions of the triple-deck analysis of Chapter II which are necessary to include the effects of a compressible subsonic freestream, a supersonic freestream, a body of non-zero thickness, and angle of attack are reported in Stewartson (1974). The present numerical results may be generalized to account for the subsonic freestream. The numerical solution for the supersonic freestream case has been performed by P. G. Daniels and is reported in Stewartson (1974).

The numerical problem associated with a body of non-zero thickness, discussed by Riley and Stewartson (1969), entails the accurate determination of the separation point and has not been solved.

The effects of non-zero angle of attack or the fundamental problem of the triple deck for a lifting flat plate has been posed by Brown and Stewartson (1970). The numerical problem is similar to the present problem but complicated by the asymmetry of the flow. The numerical solution has not been obtained since the angle of attack generates different pressures and displacement functions on the top and bottom surfaces of the plate which present another formidable problem. It should be noted that the present numerical procedure is constrained by the time required to perform the computations. This constraint is primarily due to the boundary-layer subprogram. It is recommended that subsequent numerical procedures employ considerably faster boundary-layer computation methods to solve the above problem.

The unique numerical method developed here is the method of solving the boundary-layer equations iteratively for the pressure gradient. This numerical method is stable and does not require smoothing of the data to achieve convergence between the inviscid flow and the boundary layer.

## APPENDIX A

### ERROR ANALYSES OF THE NUMERICAL PROCEDURE

Two error analyses relevant to the numerical procedure are presented in this Appendix. The first checks the initial velocity profile of Figure 2. The second was used to develop the Hilbert transformation subroutines.

#### The Upstream Velocity Profile

The upstream velocity profile may be obtained by several methods. Originally, the boundary-layer equations were integrated along the plate from an arbitrary  $-X$  location where a linear velocity profile was assumed to exist with the pressure gradient given by Equation (48) until the asymptotic value of the displacement thickness given by Equation (56) was obtained. This method was later found to have produced a velocity profile, labeled 1 on Figure 23, with a 2.5 per cent larger skin friction than predicted by Equation (56). The second method corrects this difficulty by numerically integrating Equation (54) using Hamming's modified predictor-corrector method (Ralston and Wilf (1960)) and substituting the results into Equation (52) to obtain the correct asymptotic velocity profile for  $X$  large and negative. The numerical solution of Equation (54) is presented in Table 4. The initial velocity profiles for  $X = -6$  obtained from these

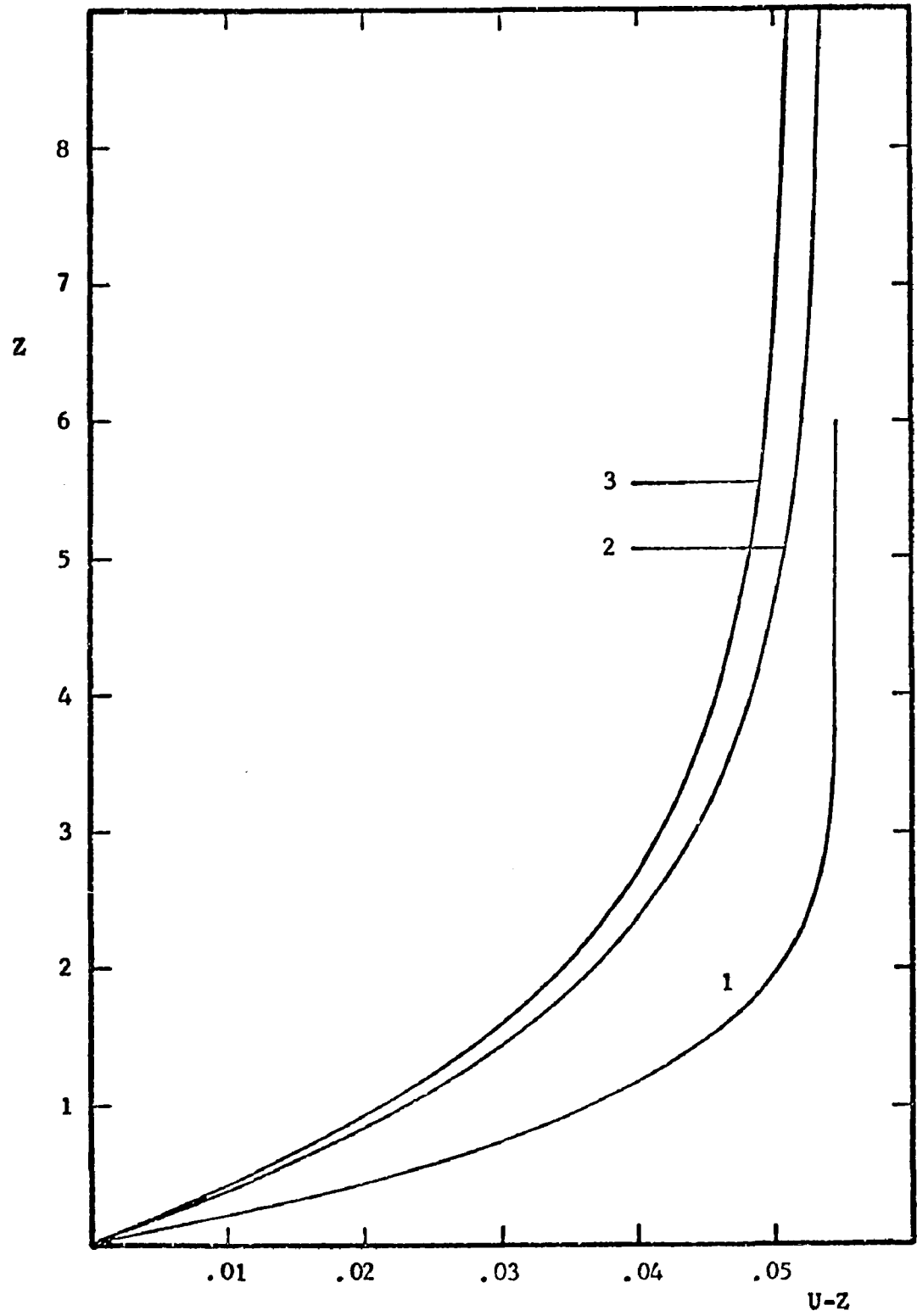


Fig. 23.--A Comparison of Initial Velocity Profiles

two methods are shown on Figure 23. The third profile serves as a final check. It is a result from the final program started at  $X = -12$  with an initial velocity profile from Equation (54) and converged to the solution.

TABLE 4

THE NUMERICAL SOLUTION OF  
 $F_1'''' - 18\eta^2 F_1'' - 36 (\eta F_1' - F_1) = -1.8330$

$\eta = \frac{Z}{3(2X)^{1/3}}$	$F_1$	$F_1' = \frac{(U-Z)X}{1.7840}$	$F_1''$
0	0	0	.6580
.05	.0008	.0306	.5673
.10	.0030	.0568	.4813
.15	.0064	.0789	.4031
.20	.0108	.0973	.3341
.25	.0161	.1125	.2749
.30	.0220	.1249	.2249
.35	.0285	.1351	.1834
.40	.0355	.1434	.1492
.45	.0428	.1501	.1213
.50	.0505	.1556	.0988
.55	.0584	.1601	.0805
.60	.0665	.1637	.0659
.65	.0747	.1667	.0540
.70	.0831	.1691	.0445
.75	.0916	.1712	.0368
.80	.1002	.1728	.0305
.85	.1089	.1742	.0255
.90	.1177	.1754	.0214
.95	.1265	.1764	.0180
1.00	.1353	.1772	.0152
1.05	.1442	.1779	.0129
1.10	.1531	.1785	.0110
1.15	.1620	.1790	.0095
1.20	.1710	.1795	.0082
1.25	.1800	.1799	.0071
1.30	.1890	.1802	.0061
1.35	.1980	.1805	.0054
1.40	.2070	.1807	.0047
1.45	.2161	.1809	.0041
1.50	.2251	.1811	.0036

The velocity profile resulting from the integration of the boundary-layer equations originating from a linear velocity profile, curve 1 of Figure 23, is shallow, indicating that the layer was not given sufficient distance to develop or the  $Z \rightarrow \infty$  boundary condition was enforced prematurely at  $Z_e = 6$ . The asymptotic velocity profile resulting from the integration of Equation (54), curve 2 of Figure 23, is in agreement with the solution from the computations initiated at  $X = -12$ , curve 3 of Figure 23, the skin friction differing by less than 0.3 per cent and the velocities across the layer differing by a lesser amount. The differences have been greatly magnified by the subtraction of the linear portion of the velocity profile to permit visualization. It should also be noted that as  $Z \rightarrow 9$  the profile becomes vertical indicating that the boundary condition given by Equation (84) is not being enforced prematurely.

A clear indication that the initial velocity profile has been located a sufficient distance upstream is given by the skin friction results shown on Figure 24. When the velocity profile labeled 1 of Figure 23 is used to begin the computations, the skin friction curve begins at the larger, incorrect value but recovers to join the correct skin friction curve further downstream. The increased skin friction from  $X = -6$  to  $X = -3$  due to the shallow initial velocity profile results in a three per cent higher multiplicative drag constant, thus necessitating the use of the corrected velocity profile labeled 2.

Another confirmation that the depth of the layer is sufficient to correctly determine the skin friction is provided by the value of  $\lambda_1$ . Performing  $h^2$ -extrapolation (Beckenbach (1961)) on the data



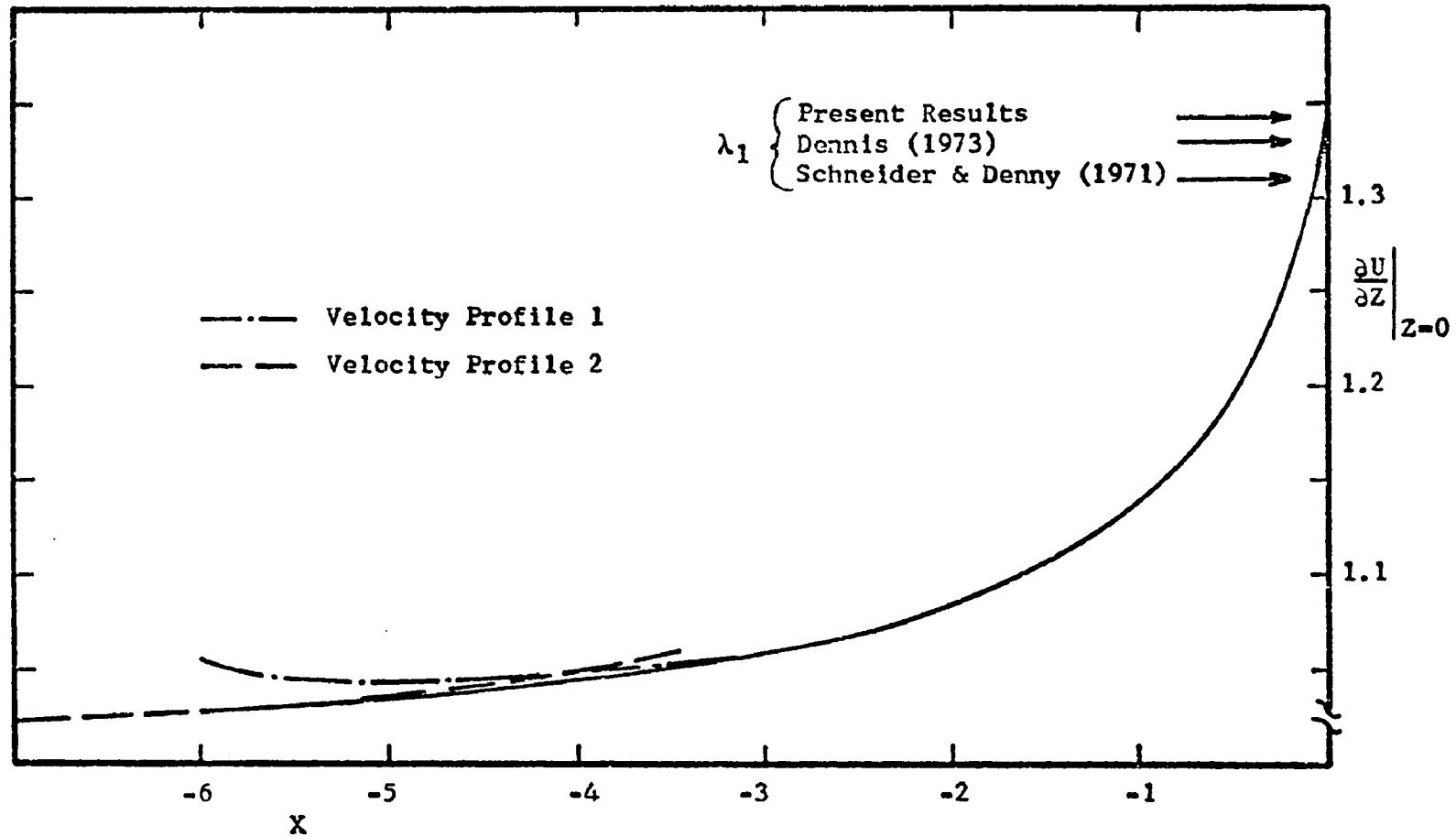


Fig. 24.--A Comparison of the Skin Friction resulting from the Initial Velocity Profiles

resulting from either of the initial velocity profiles yields the same result,  $\lambda_1 = 1.343$ .

### The Hilbert Integral

The numerical method used to compute the central portion of the Hilbert integral, subtracting the singularity, has been checked by comparison with a second method and by comparison with the solutions to Van Dyke's (1959) airfoil integrals. The two Hilbert transformation subroutines were checked by employing the skew-reciprocal property of the transformation.

The second method for the numerical evaluation of Cauchy integrals is reported in Collatz (1966) and attributed to Weber. The method consists of splitting the range of integration about the singularity and translating the singularity to the origin in each of the resulting integrals. Thus, employing this method, the center integral of Equation (79) is

$$\int_a^e \frac{P(X_1) dX_1}{X-X_1} = \int_0^{X-a} \frac{P(X-s) ds}{s} - \int_0^{e-X} \frac{P(X+s) ds}{s} \quad (96)$$

where  $s = X-X_1$  in the first integral and  $s = X_1-X$  in the second integral on the right hand side. When the integrands are combined, three cases that depend upon the position of the singularity within the original interval result and

$$\int_a^e \frac{P(X_1) dX_1}{X-X_1} = - \int_0^{X-a} \frac{P(X+s)-P(X-s)}{s} ds - \int_{e-X}^{X-a} \frac{P(X+js)}{s} ds \quad (97)$$

Here  $j = +1$  if  $|X-a| < |e-X|$ ,  $j = 0$  if  $|X-a| = |e-X|$  and  $j = -1$  when  $|X-a| > |e-X|$ . In each of the three cases the singularity has been translated to the origin. The remaining portions of the integrals are nonsingular and may be integrated by the trapezoidal rule. The singularity is treated by assuming a Taylor series as it was for the subtraction of the singularity method.

An error analysis was performed utilizing three of Van Dyke's (1959) airfoil integrals. The solutions are given in closed form and the two methods were compared with each other and the solution. For the three cases considered smaller errors were incurred using the subtraction of the singularity technique than with Weber's method. It was therefore eliminated from further consideration. Figure 25 presents the error incurred during the computation of the Cauchy integral of the function  $X_1^3$  since it was determined that cubics fit wide ranges of Messiter's (1970) data very closely. The error approaches three per cent as the singularity approaches the endpoint for  $\Delta X = 0.1$ . For the smaller step sizes,  $\Delta X = 0.05$  and  $0.01$ , the error is less than 0.7 per cent for all points. The error for  $\Delta X = 0.05$  is small and this step size was selected to perform many of the ensuing computations. The smaller step size was reserved for final checks on the entire program.

The skew-reciprocal property of the Hilbert transformation permits the simultaneous error analysis of both the  $P(X)$  and  $A'(X)$  subroutines. One subroutine computes  $A'(X)$  from  $P(X)$  by assembling the appropriate expressions for the integrals of the asymptotic expansions of  $P(X)$  and the above numerical methods. Particular attention

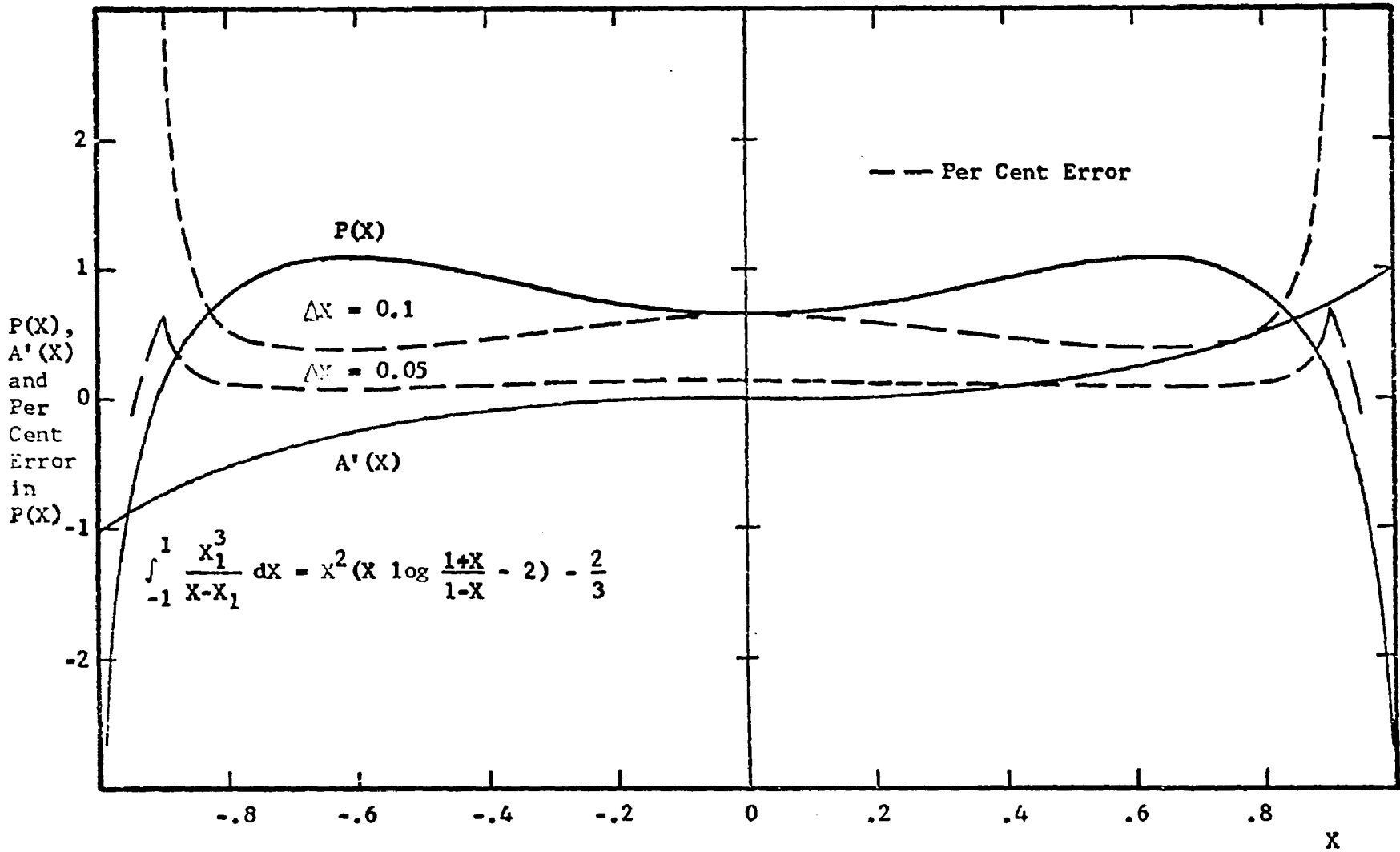


Fig.25.--Cauchy Integral Error Analysis

is required to insure that each method is employed only within its range of validity, i.e.,  $X = a$ ,  $X < 0$ ,  $X = 0$ ,  $X > 0$  or  $X = e$ . The other subroutine computes the pressure,  $P(X)$ , from  $A'(X)$  by the same procedure utilizing the appropriate expressions resulting from the integrals of the asymptotic expansions of  $A'(X)$ . Subsequent error analysis and programming checks were facilitated by the skew-reciprocal nature of the subprograms which were combined in a short flip-flop program. The input is an assumed  $A'(X)$ ; the output is the error accumulated in computing the pressure from  $A'(X)$  and then computing  $A'(X)$  plus the two-way error from the pressure. Messiter's (1970) form for  $A'(X)$ , Equation (76) with  $C_9 = 0$ , was used to check the subroutines since the converged form was not yet available. The relevant error is the error in computing  $A(X)$  since it is  $A(X)$  that drives the inner loop to produce  $P'(X)$ . This feature of the inner loop eliminates the requirement for further numerical differentiations and simultaneously requires a numerical integration.

Figure 26 presents the error incurred in performing the transformation and inversion of  $A'(X)$  and the subsequent trapezoidal rule integrations employed here and in the main program to obtain  $A(X)$ . The error based on the local value of the function reaches a maximum of about seven per cent when the limits of the numerical integration are located at  $X = \pm 3$ . Extending the limits to  $\pm 6$  diminished the maximum error to about five per cent thus demonstrating the necessity for extending the limits on the main program to  $X = \pm 6$  or larger. It is noted that the error does not decrease with  $\Delta X$  and remains relatively constant with  $\Delta X$  decreasing. This must be attributed to

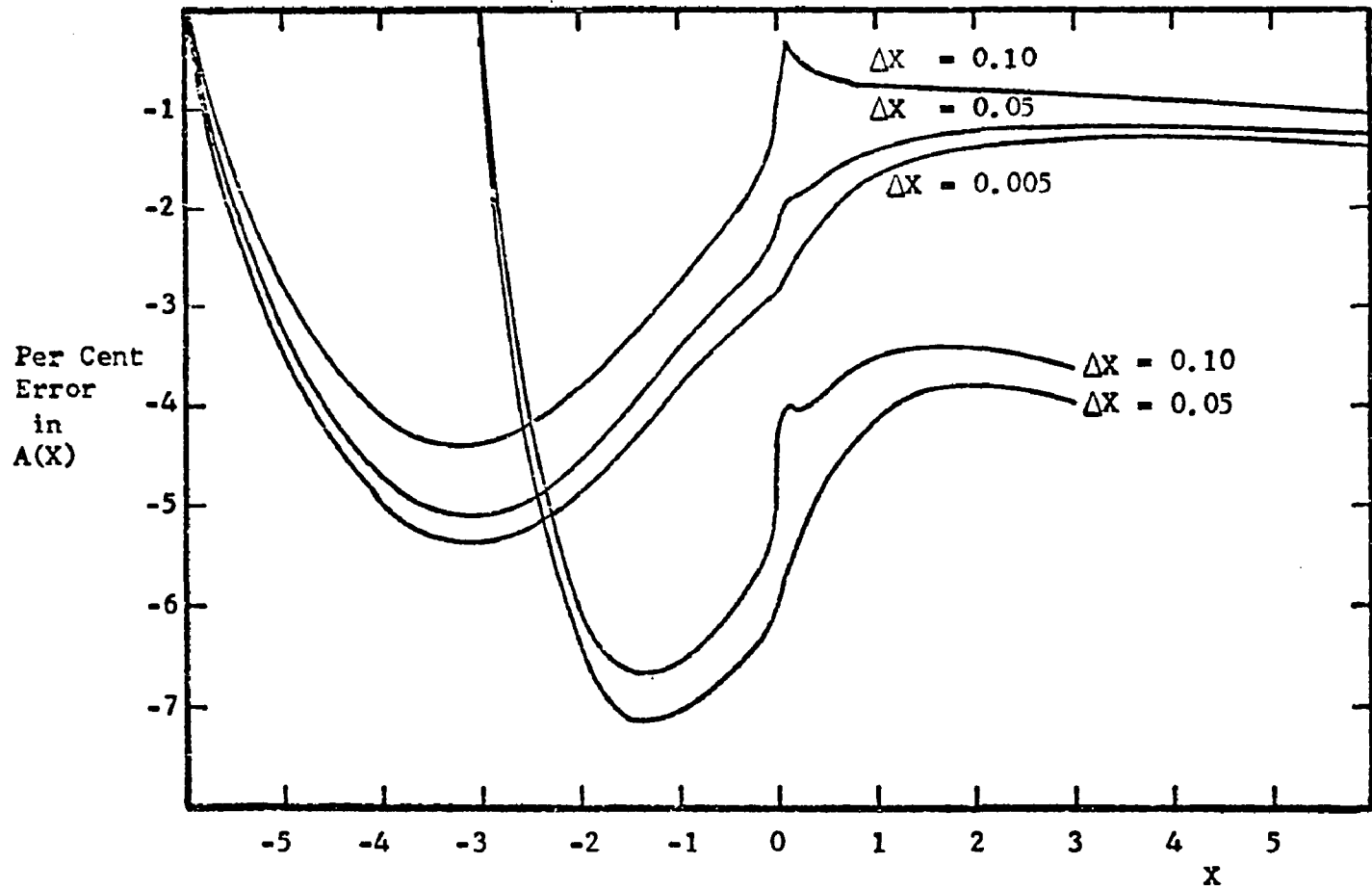


Fig.26.--Hilbert Transformation Error Analysis

the addition of the integrals of the asymptotic forms since Figure 25 demonstrates that the numerical scheme employed in the central section produces errors that diminish with  $\Delta X$ .

The error curves of Figure 26 represent an extreme upper bound for the main program because the outer loop only requires the single transformation of  $P(X)$  into  $A'(X)$  and the results are smoother functions of  $X$  than were those employed here. Error checks of this type were also performed using the results and are reported in the discussion of the results, Chapter IV.

## APPENDIX B

### THE ASYMPTOTIC BEHAVIOR OF THE NUMERICAL RESULTS

The purpose of this Appendix is to present the numerical study which led to the selection of the boundary conditions and parameters of the numerical interval employed during the computation of the final data. The computations reported in this Appendix were performed on the interval  $-6 \leq X \leq 6$  with  $\Delta X = 0.05$  and  $H = 0.1$ . The location of the outer edge was a variable. In order to decrease the computational time required and the cost, all ensuing computations were initiated with the solution, i.e., the  $A'(X)$  and  $P'(X)$  from a previous computation. The effects on the solution wrought by the various changes in the numerical procedure were measured by the relative agreement of the  $b_1$  curves. The constant  $b_1$  measures how precisely the numerical solution approaches the asymptotic predictions for the pressure, displacement thickness and centerline velocity. The coefficient  $b_1$  of the second-order term of asymptotic expansions Equations (62), (63), (64), and (65) is computed using Equations (93), (94) and (95). Seven different cases are reported, Figures 27 through 33, for comparison with the final results on Figure 14.

The  $b_A$ ,  $b_P$ , and  $b_U$  values for the first case are presented on Figure 27. The shallow initial profile of Figure 23 initiated the computations and the outer edge of the layer was located at  $Z_e = 6$ .



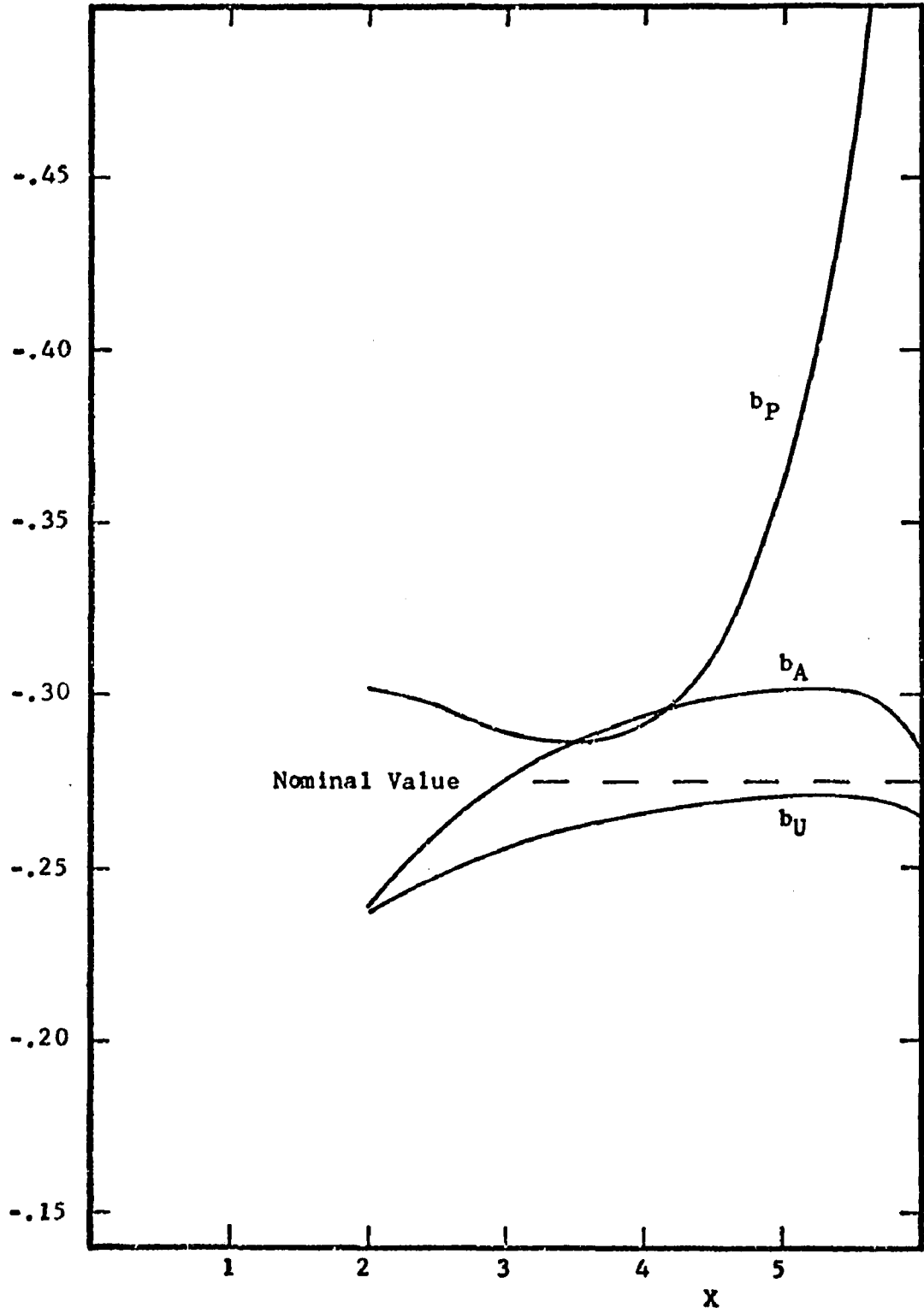


Fig. 27.--Asymptotic Behavior:  $Z_e = 6$ , Shallow Velocity Profile

The  $b_U$  values resulting from the asymptotic expansion of  $U(X,0)$  appear to be approaching the nominal value. The  $b_p$  values resulting from the asymptotic expansion of  $P(X)$  approach the nominal value then rapidly increase due to numerical error. The  $b_A$  values resulting from the asymptotic expansion of  $A(X)$  reach a maximum value about 10 per cent above the nominal value of  $b_1$ .

The first change in the main program subsequent to achieving the convergent numerical procedure was generated by the skin friction of Figure 24 which is noticeably larger than the predicted asymptotic value when the shallow initial velocity profile is employed to start the computations. Improved computations of Case 2 were initiated using the velocity profile shown in Figure 23 with  $Z_e = 6$ . The centerline velocity and pressure results were slightly improved and the displacement thickness results,  $b_A$ , were significantly improved, as shown on Figure 28. The effect of the incorrect outer portion of the initial profile had propagated throughout the entire streamwise course of the lower deck while the lower portions of the velocity profiles were affected a much shorter distance.

To insure that the outer edge-boundary condition was not being enforced prematurely, the outer edge of the layer was removed to  $Z_e = 8$ . The results of Case 3 indicate that  $Z_e = 6$  is too shallow, for both the pressure and displacement thickness results came into closer agreement with the centerline velocity results which remained relatively unchanged, as shown on Figure 29.

However, the rapid increase in the pressure results toward the downstream end of the numerical interval remained. The pressure

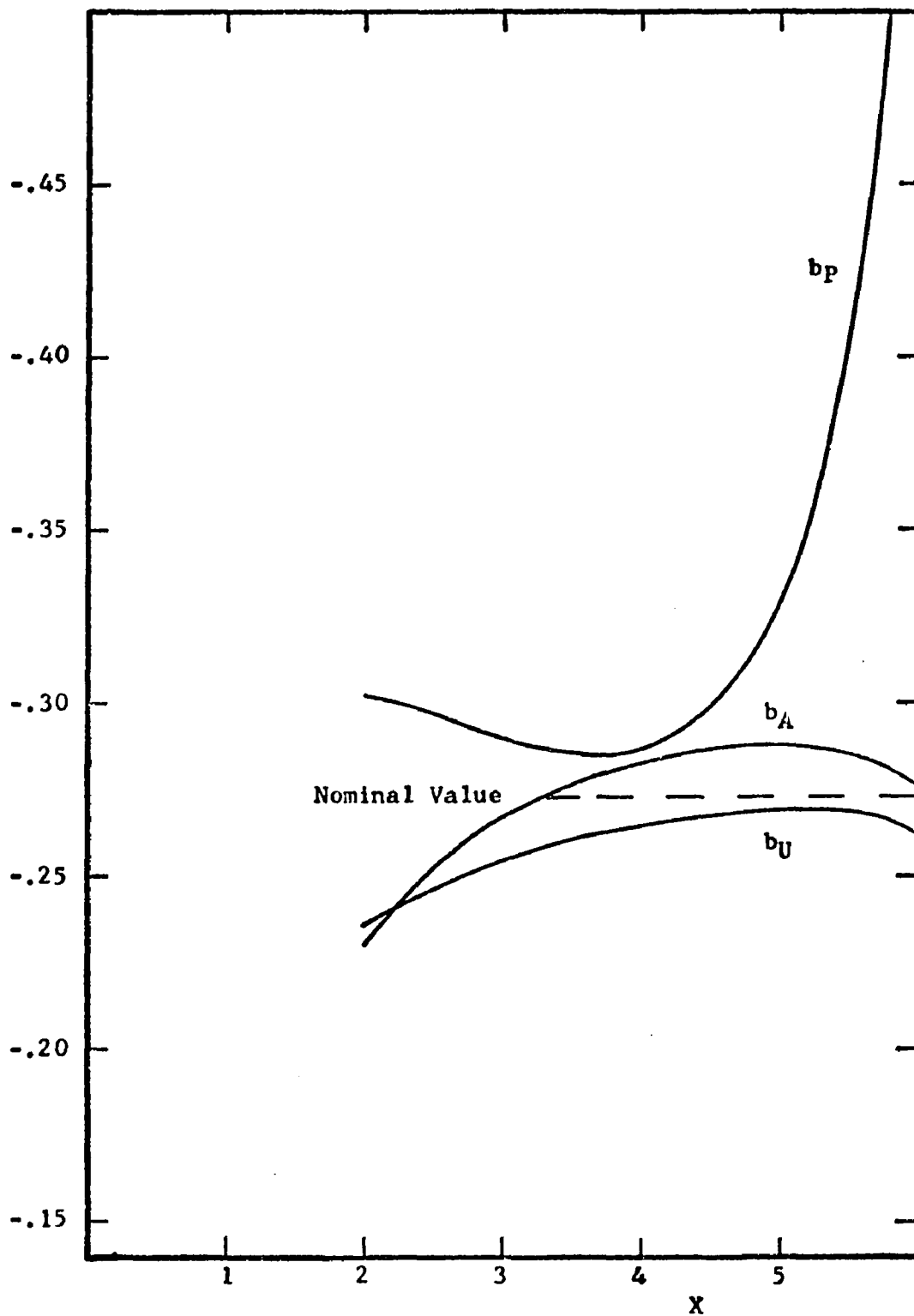


Fig. 28.--Asymptotic Behavior:  $Z_e = 6$ , Revised Velocity Profile

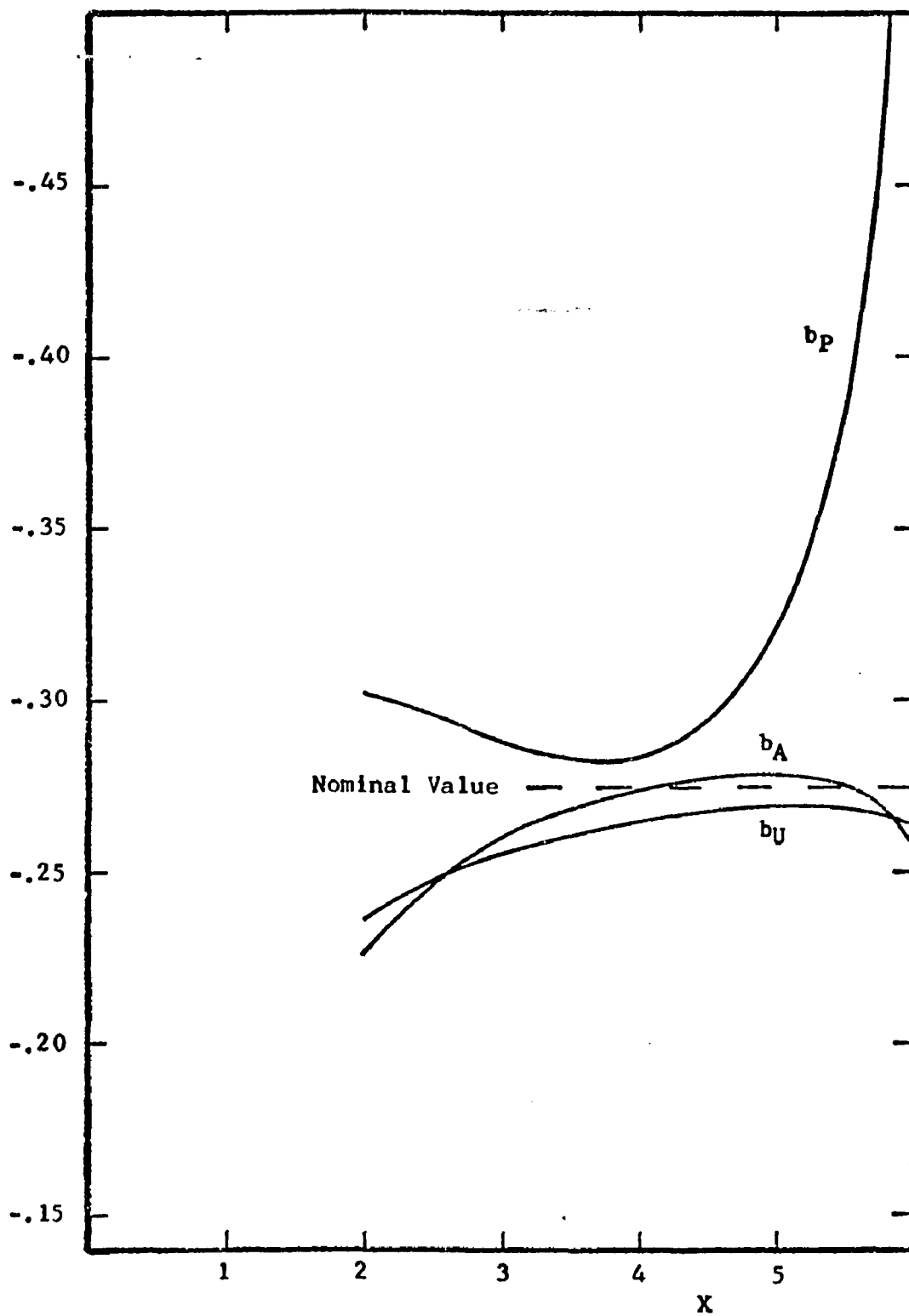


Fig. 29.--Asymptotic Behavior:  $Z_e = 8$ , Revised Velocity Profile

shift at the upstream end of the interval to obtain the correct value of  $A'(X)$  could have been the cause. The shift of the entire pressure curve by a constant  $\Delta P$  produces a logarithmic term in  $A'(X)$  through the Cauchy integral, Equation (78). Thus, if

$$\Delta A'(X) = -\frac{1}{\pi} \int_a^e \frac{\Delta P}{X-X_1} dX_1$$

then

$$\Delta A'(X) = -\frac{\Delta P}{\pi} \log \left| \frac{X-a}{X-e} \right|$$

over the finite numerical range of integration. The numerical procedure shifts the entire  $P(X)$  curve resulting from the inner loop until  $A'(X)$  agrees with the predicted asymptotic behavior Equation (56). This shift could induce the rapid increase in the  $b_p$  curves of the previous Figures 27, 28, and 29 through the above logarithmic term.

The results of Case 4 demonstrate that the above hypothesis is false. The pressure shift was deleted and a value of  $b_1$  was computed by averaging the values of  $b_A$  and  $b_U$  from the previous cycle of the iteration procedure. The pressure expansion for  $X \rightarrow -\infty$  Equation (65) with the cyclically updated value of  $b_1$  was used to obtain the initial value of the pressure,  $P(a)$ . The numerical procedure converged more slowly to the same results as Case 3 as a comparison of Figures 29 and 30 will show. The effect of shifting the pressure curve to obtain the asymptotic value of  $A'(X)$  is to damp the oscillations which occur during the cycles of the iteration procedure and thus increase the rate of convergence.

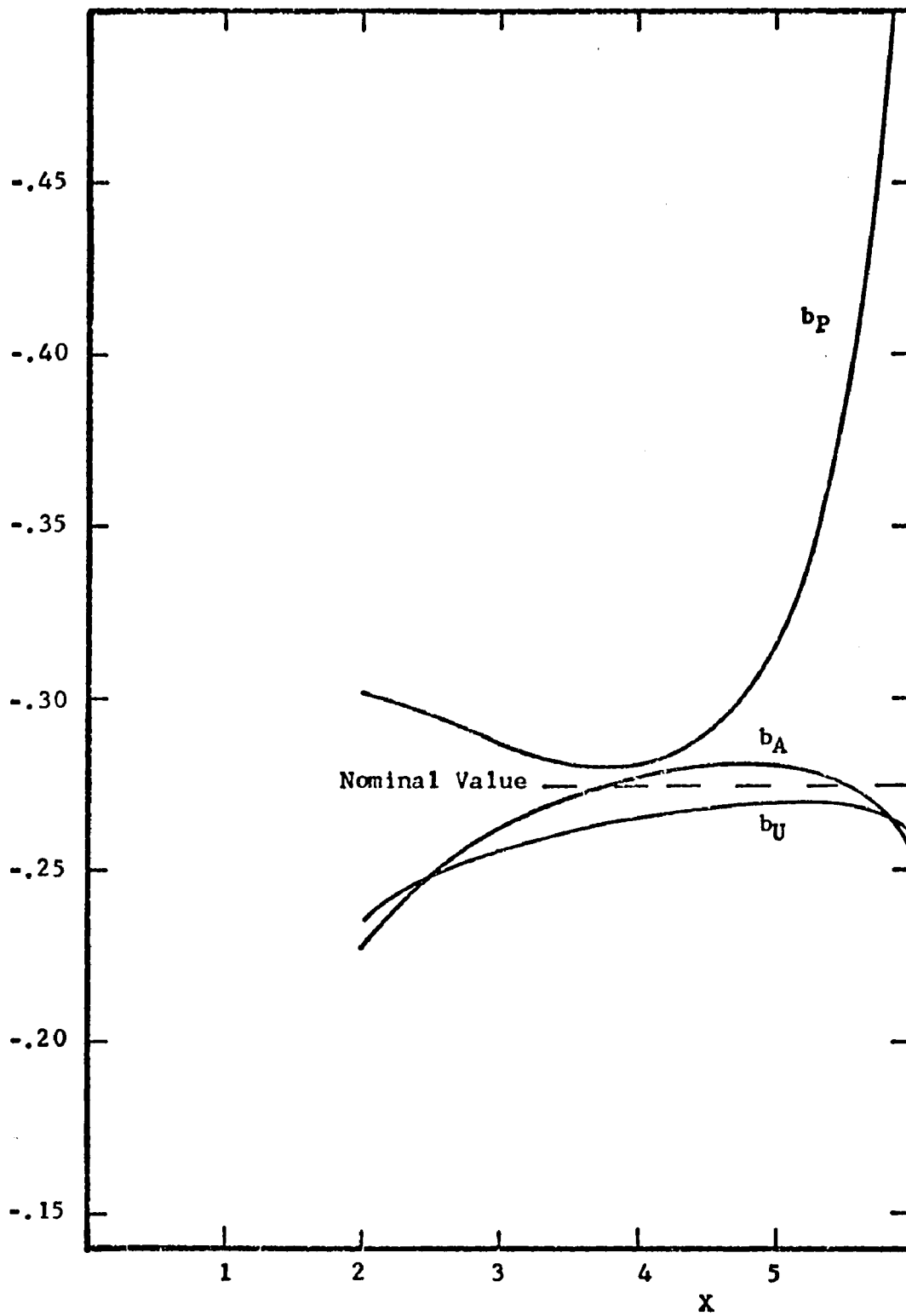


Fig. 30.--Asymptotic Behavior:  $Z_e = 8$ , The Pressure Shift

The computations to this point have not included the second-order terms of the asymptotic expansions of  $P(X)$  and  $A(X)$ , which depend upon  $b_1$ , in the integrals of the asymptotic contributions to the Hilbert transformation, Equation (79). Case 4 demonstrated that the iteration procedure will converge without the pressure shift and employed a method to update the value of  $b_1$  during each iteration cycle. Case 5 illustrates the effects of including all the second-order terms in the asymptotic contributions to the Hilbert transformation utilizing the  $b_1$  obtained by the method of Case 4. The outer edge of the layer was removed to  $Z_e = 9$  and  $A(X)$  was computed at  $Z = 8$  to further insure that the effects of the outer edge boundary condition were minimal. The inclusion of the second-order terms in the Hilbert transformation effectively reversed the previous results about the nominal value as shown on Figure 31. The pressure results of Case 5 rapidly decrease from the nominal value of  $b_1$ .

Case 6, Figure 32, is the useful result of a programming error. The sign of  $b_1$  was inadvertently reversed before being input to the Hilbert transformation subroutine. Thus, the second-order terms of the asymptotic contributions are subtracted from the resulting integral. The results again indicate a rapid increase in  $b_p$  and a greater variation from the nominal value of  $b_1$  than the previous similar results.

Taken together, Cases 5 and 6 demonstrate that the numerical error in the Hilbert transformation is in the same sense as the second-order terms and that the inclusion of these terms is not an adjuvant procedure.

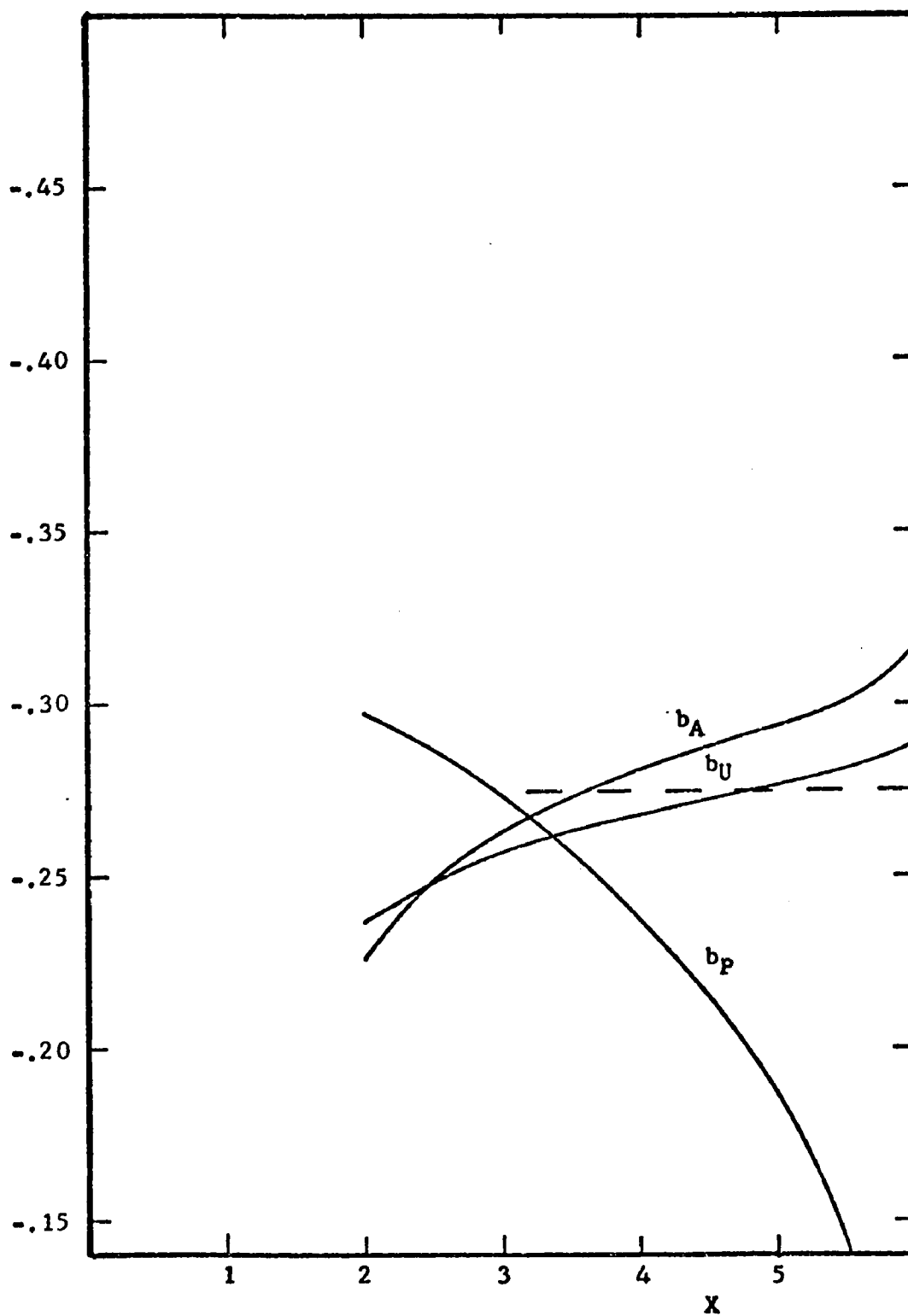


Fig. 31.--Asymptotic Behavior:  $Z_e = 9$ , Second-Order Terms



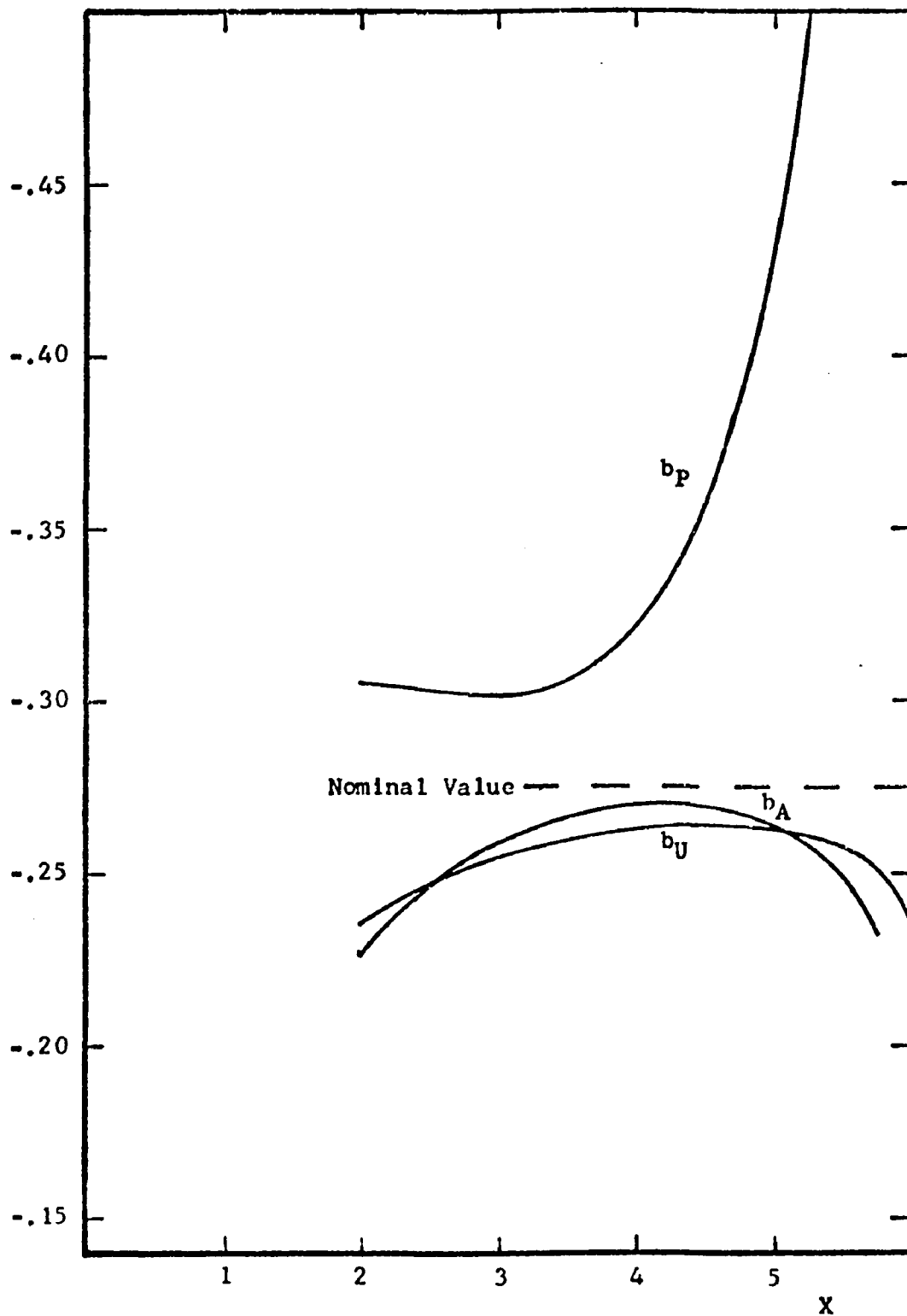


Fig. 32.--Asymptotic Behavior:  $Z_e = 9$ , Second-Order Terms

The final case was computed to ascertain the effects of removing the higher-order wake-centerline boundary condition, Equation (87), and employing in its stead  $R_1 = 0$ . The previous study by the momentum-integral method, Equation (88), had indicated that the centerline velocity would be slightly reduced and perhaps agreement with the pressure results of Case 5 could be attained. The results of the computation shown on Figure 33, are disastrous. The three sets of values of  $b_1$  diverge from each other as  $X$  increases.

An inspection of the preceding seven cases reveals that the values of  $b_1$  obtained from the centerline velocity and displacement thickness data remain near the nominal value of  $-0.275$ . The errors shown on the preceding Figures 27 through 32 are second-order and amount to less than one per cent mismatch between the asymptotic expansions and the numerical data near the end of the interval. The pressure data have a much greater range about the nominal value and mismatches of five to ten per cent occur in the small values of the pressure at  $X = 6$ .

The effects of the mismatches on the plate upstream may be measured by the changes in  $\lambda_1$  and the constant appearing in the drag equation. The variation in  $\lambda_1$  was less than 0.1 per cent for Cases 1 through 6 and 1.2 per cent for Case 7. The drag equation constant is somewhat more sensitive to the changes because it is the integral of the skin friction over the entire plate. Variations approaching 1.5 per cent were found except for Case 1 which was initiated with the incorrect value of the skin friction. The data clearly shows that small changes a sufficient distance downstream induce even smaller

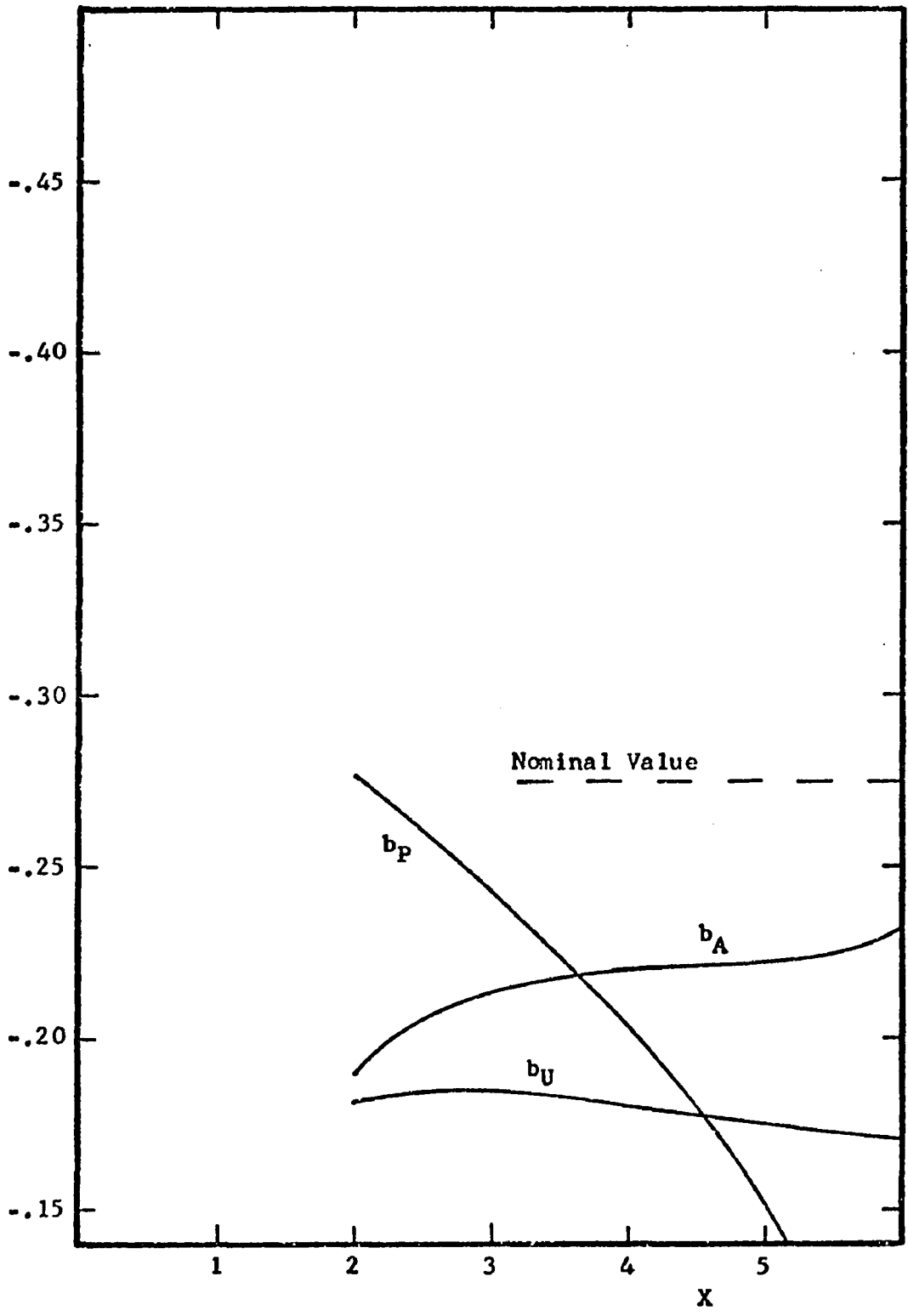


Fig. 33.--Asymptotic Behavior:  $Z_e = 9$ , Centerline Boundary Condition

changes in the flow upstream. This is also evident from the three  $b_1$  curves which respectively approach the same value as  $X$  decreases.

The study of the second-order terms in the expansions of  $P(X)$ ,  $A(X)$  and  $U(X,0)$  as  $X \rightarrow \infty$  undertaken in this Appendix indicates that:

1. The second-order terms should not be included in the Hilbert integral,
2. The pressure shift should be retained,
3. The higher-order wake centerline boundary condition is necessary,
4. The outer edge of the layer should be extended as far as computational time required permits,
5. The initial velocity profile must be accurate, and
6. The downstream boundary conditions should be approached as precisely as possible.

The numerical procedure used to compute the final data was designed to meet the above criteria.

## APPENDIX C

### THE BOUNDARY-LAYER DIFFERENCE EQUATIONS

The boundary-layer subprogram solves Equation (41)

$$\frac{\partial U}{\partial X} + \frac{\partial V}{\partial Z} = 0$$

$$U \frac{\partial U}{\partial X} + V \frac{\partial U}{\partial Z} = - \frac{dP}{dX} + \frac{\partial^2 U}{\partial Z^2}$$

for the velocity profile  $U(Z)$  by using a Crank-Nicholson type implicit finite difference procedure. Introduce the stream function  $F$  such that

$$\partial F / \partial X = -V, \quad \partial F / \partial Z = U$$

and rewrite Equation (41) so that

$$\frac{\partial^2 U}{\partial Z^2} + \beta = U \frac{\partial U}{\partial X} - \frac{\partial F}{\partial X} \frac{\partial U}{\partial Z} \quad (98)$$

where  $\beta = -dP/dX$ .

Define  $\hat{U}_j$  as the velocity at the previous streamwise station,  $X - \Delta X$ , and

$$\bar{U}_j = U_j - 0.5 \Delta U_j$$

where  $\Delta U_j = U_j - \hat{U}_j$

and similarly define the  $F_j$ . The subscript  $j$  denotes the  $Z$ -direction distance at  $Z = (j-1) H$ .

On substituting the preceding definitions into Equation (98) and using centered difference formulas we find that

$$\frac{\bar{U}_{j+1} - 2\bar{U}_j + \bar{U}_{j-1}}{H^2} + \beta = \bar{U}_j \frac{\Delta U_j}{\Delta X} - \frac{\bar{U}_{j+1} - \bar{U}_{j-1}}{2H} \frac{\Delta F_j}{\Delta X}$$

or alternatively

$$\frac{U_{j+1} - 2U_j + U_{j-1}}{H^2} - \frac{\Delta U_{j+1} - 2\Delta U_j + \Delta U_{j-1}}{2H^2} + \beta =$$

$$\frac{(U_j + \hat{U}_j)(U_j - \hat{U}_j)}{2\Delta X} - \left( \frac{U_{j+1} - U_{j-1}}{2H} - \frac{\Delta U_{j+1} - \Delta U_{j-1}}{4H} \right) \frac{F_j - \hat{F}_j}{\Delta X}.$$

The matrix elements of the boundary-layer subroutine are obtained by collecting the coefficients of  $U_{j+1}$ ,  $U_j$ , and  $U_{j-1}$  in the above equation. By defining

$$\sigma_1 = [2 + H^2 (U_j + \hat{U}_j)/2\Delta X]^{-1}$$

$$\sigma_2 = \sigma_1 H (F_j - \hat{F}_j)/2\Delta X$$

$$A_j = -\sigma_1 + \sigma_2$$

$$B_j = -\sigma_1 - \sigma_2$$

and

$$R_j = \sigma_1 [\beta H^2 + U_j - \hat{U}_j + H^2 \hat{U}_j (U_j + \hat{U}_j)/2\Delta X] \\ + 0.5 [A_j (U_{j-1} - \hat{U}_{j-1}) + B_j (U_{j+1} - \hat{U}_{j+1})]$$

we obtain the difference equation

$$B_j U_{j+1} + U_j + A_j U_{j-1} = R_j \quad .$$

This tridiagonal matrix equation is solved by using Gaussian elimination to eliminate the  $A_j$  diagonal and back substitution to determine the velocity profile (Richtmyer and Morton (1967)). If the difference between successive velocity profiles is less than the error tolerance, the iteration procedure has converged. If not, the velocity profile is integrated by the trapezoidal rule to obtain an updated stream function and the iteration procedure is repeated until the error tolerance is satisfied. Although not especially fast this procedure has been found to be stable and accurate for relatively large step size for a variety of boundary-layer problems.

The boundary conditions are enforced by prescribing values for specific elements of the matrix, the velocity and the  $R_j$ . The boundary condition on the wake centerline has been obtained by considering a Taylor series of the velocity

$$U_2 = U_1 + 0.5 H^2 \left( \frac{\partial^2 U}{\partial Z^2} \right)_1 + \dots$$

and the momentum equation

$$\left( \frac{\partial^2 U^2}{\partial Z^2} \right)_1 = -\beta + U_1 \frac{dU_1}{dX}$$

for  $Z = 0$ . In difference form,

$$U_2 - U_1 = 0.5 H^2 [\beta + (U_1 - \hat{U}_1)/\Delta X]$$

which requires that

$$B_1 = -1$$

and

$$R_1 = -0.5 H^2 [\beta + U_1 (U_1 - \hat{U}_1)/\Delta X] .$$

Upstream on the plate, the skin friction is calculated by the same method from the formula

$$\left. \frac{\partial U}{\partial Z} \right|_{Z=0} = \frac{U_2}{H} + 0.5H \beta$$

since  $U_1 = 0$ .

The boundary-layer subprogram has been used to compute the Goldstein inner wake with  $Z_e = 9$  and  $H = .10$ ,  $\Delta X = .05$  or  $H = .05$ ,  $\Delta X = .025$  for comparison with the results in Chapter IV. The pressure gradient for the Goldstein wake computation is zero and the main program consisted of a single loop which advanced the computation downstream. A linear velocity profile was used to start the computation at the trailing edge. The centerline velocity results for the two grid sizes are compared with the first term of Goldstein's expansion for the centerline velocity on Figure 34. The numerical results are shifted downstream from Goldstein's results because of the finite step size of the numerical computations. The shift in the centerline velocity decreases as the step size decreases. The computed velocities are less than 0.1 per cent smaller than Goldstein's results for  $X > 5$ . Increasing the centerline velocity reported in the results, Chapter IV, by this amount would decrease the value of  $b_U$  and bring the  $b_A$  and  $b_U$  curves of Figures 14, 15 and 16 into closer agreement.



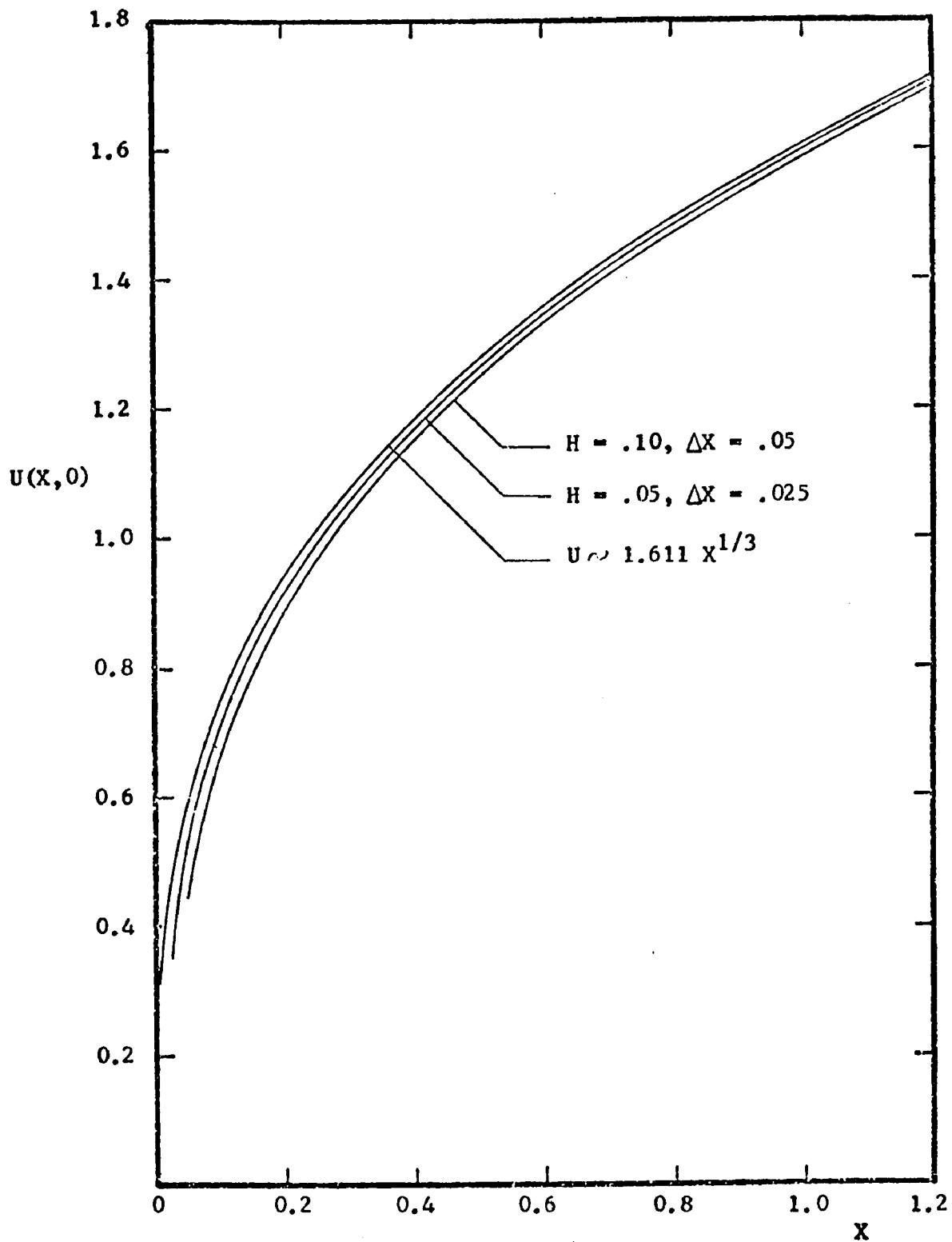


Fig. 34.--A Comparison of the Centerline Velocity for Goldstein's Inner Wake

## REFERENCES

- Beckenbach, E. F., (editor). 1961. Modern mathematics for the engineer. pp. 383-403. New York: McGraw-Hill.
- Blasius, H., 1908. Grenzschichten in Flussigkeiten mit kleiner Reibung. Z. Math.Phys., 56:1-37. English translation: NACA TM 1256.
- Brown, S. N., and Stewartson, K. 1970. Trailing-edge stall. J. Fluid Mech., 42:561-584.
- Burggraf, O. R. 1969. Computation of separated flow over backward-facing steps at high Reynolds number. In Proc. of the 1969 Symposium Viscous Interaction phenomena in supersonic and hypersonic flow. pp. 463-491. Dayton: Univ. of Dayton Press.
- Collatz, L. 1966. The numerical treatment of differential equations. pp. 508-509. New York: Springer-Verlag.
- Davis, P. J., and Rabinowitz, P. 1967. Numerical integration. pp. 72-80. Waltham, Mass.: Blaisdell.
- Dennis, S. C. R. 1973. private communication.
- Dennis, S. C. R., and Chang, Gau-Zu. 1969. Numerical integration of the Navier-Stokes equations for steady two-dimensional flow. Phys. Fluids Suppl. II:88-93.
- Dennis, S. C. R., and Dunwoody, J. 1966. The steady flow of a viscous fluid past a flat plate. J. Fluid Mech., 24:577-595.
- Denny, V. E. 1972. Reply by author to A. F. Messiter and K. Stewartson. AIAA J., 10:719-720.
- Goldberg, A., and Cheng, Sin-I. 1961. The anomaly in the application of Poincare-Lighthill-Kuo and parabolic coordinates to the trailing edge boundary layer. J. Math. and Mech., 10:529-535.
- Goldstein, S. 1930. Concerning some solutions of the boundary layer equations in hydrodynamics. Proc. Cambridge Phil. Soc., 26:1-30.
- Hakkinen, R. J., and Rott, N. 1965. Similar solutions for merging shear flows II. AIAA J., 3:1553-1554.

- Imai, I. 1957. Second approximation to the laminar boundary-layer flow over a flat plate. *J. Aeronaut. Sci.*, 24:155-156.
- Janour, Z. 1951. Resistance of a plate in parallel flow at low Reynolds numbers. NACA TM 1316.
- Kuo, Y. H. 1953. On the flow of an incompressible viscous fluid past a flat plate at moderate Reynolds numbers. *J. Math. and Phys.*, 32:83-101.
- Lagerstrom, P. A., and Cole, J. D. 1955. Examples illustrating expansion procedures for the Navier-Stokes equations. *J. Rat. Mech. Anal.*, 4:817-882.
- Mangler, K. W. 1951. Improper integrals in theoretical aerodynamics. RAE Rept. Aero. 2424.
- Messiter, A. F. 1970. Boundary-layer flow near the trailing edge of a flat plate. *SIAM J. Appl. Math.*, 18:241-257.
- Messiter, A. F., and Stewartson, K. 1972. Comment on "Evolution of the laminar wake behind a flat plate and its upstream influence." *AIAA J.*, 10:719-720.
- Petit Bois, C. 1961. *Tables of Indefinite Integrals.* pp. 8-9. New York: Dover.
- Plotkin, A., and Flugge-Lotz, I. 1968. A numerical solution for the laminar wake behind a finite flat plate. *J. Appl. Mech.*, 90:625-630.
- Ralston, A., and Wilf, H. S. 1960. *Mathematical methods for digital computers.* pp. 95-109. New York: Wiley.
- Richtmyer, R. D., and Morton, K. W. 1967. *Difference methods for initial-value problems.* p. 191. New York: Interscience.
- Riley, N., and Stewartson, K. 1969. Trailing edge flows. *J. Fluid Mech.*, 39:193-207.
- Rosenhead, L. 1961. *Laminar boundary layers.* pp. 222-281. London: Oxford.
- Schneider, L. I., and Denny, V. E. 1971. Evolution of the laminar wake behind a flat plate and its upstream influence. *AIAA J.*, 9:655-660.
- Stewartson, K. 1969. On the flow near the trailing edge of a flat plate II. *Mathematika*, 16:106-121.
- Stewartson, K. 1974. Multi-structured boundary layers on flat plates and related bodies. In preparation.

- Talke, F. E., and Berger, S. A. 1970. The flat plate trailing edge problem. *J. Fluid Mech.*, 40:161-189.
- Titchmarsh, E. C. 1937. Introduction to the theory of Fourier integrals. pp. 119-151. London: Oxford.
- Van Dyke, M. 1959. Second-order subsonic airfoil theory including edge effects. NACA Rept. 1274.
- Van Dyke, M. 1964. Perturbation methods in fluid mechanics. pp. 121-146. New York: Academic Press.